

Dissertation

submitted to the

Combined Faculty of Mathematics, Engineering and Natural Sciences

of

Heidelberg University, Germany

for the degree of

Doctor of Natural Sciences

Put forward by

Adrian Lukas Braemer

born in: Heidelberg, Germany

Oral examination: 14.11.2024

QUANTUM DYNAMICS OF DISORDERED MANY-BODY SPIN SYSTEMS

Effects of Spatial Disorder in a Dipolar, Frozen Gas and
Influence of Spatial Inhomogeneity in Periodically Driven Systems

Referees: Prof. Dr. Martin Gärttner
Prof. Dr. Tilman Enss

Do I want to dedicate this to someone?

ToDo:

- Do all of the things
- Remember to update the Title in **2 places**

ABSTRACT

In this thesis, we study the thermalization properties in both closed and periodically driven systems subject to spatial inhomogeneities. In Part 1, we take motivation from current state-of-the-art experimental platforms using cold atoms to implement long-range Heisenberg spin models of spatially disordered spins. We find numerically, that the disordered couplings induced by the randomly positioned spins can lead to a many-body localized regime. Using perturbative arguments based on the real-space renormalization group, we demonstrate that the emergent quasi-conserved quantities are due to pairs of strongly interacting spins decoupling from their environment. Predictions of the resulting effective model of pairs are subsequently compared to real experimental data for validation are found to be highly accurate. In the second part of this thesis, we pivot to an ordered spin system subject to a periodic driving field with spatial inhomogeneity. It is demonstrated that a deviation on only a single site of an otherwise uniform drive can already enhance the lifetime of the system's magnetization dramatically. We link this behavior again to the presence of approximate conservation laws that are stabilized by the spatial inhomogeneity.

ZUSAMMENFASSUNG

Deutsche Übersetzung des vorigen Abstrakts.

PUBLICATIONS

This thesis is based on the following manuscripts and publications:

- [A] A. **Braemer**, T. Franz, M. Weidemüller, and M. Gärttner, "Pair localization in dipolar systems with tunable positional disorder," *Physical Review B* **106**, 134212 (2022).
- [B] T. Franz*, S. Geier*, C. Hainaut, A. **Braemer**, N. Thaicharoen, M. Hornung, E. Braun, M. Gärttner, G. Zürn, and M. Weidemüller, *Observation of universal relaxation dynamics in disordered quantum spin systems*, Sept. 2023.
- [C] T. Franz, S. Geier, A. **Braemer**, C. Hainaut, A. Signoles, N. Thaicharoen, A. Tebben, A. Salzinger, M. Gärttner, G. Zürn, and M. Weidemüller, *Emergent pair localization in a many-body quantum spin system*, 2022.
- [D] A. **Braemer**, J. Vahedi, and M. Gärttner, *Cluster truncated Wigner approximation for bond-disordered Heisenberg spin models*, July 2024.
- [E] N. Euler*, A. **Braemer***, L. Benn, and M. Gärttner, "Metronome spin stabilizes time-crystalline dynamics," *Physical Review B* **109**, 224301 (2024).

*These authors contributed equally.

The author also contributed to the following publications:

- [F] S. Geier, A. **Braemer**, E. Braun, M. Müllenbach, T. Franz, M. Gärttner, G. Zürn, and M. Weidemüller, *Time-reversal in a dipolar quantum many-body spin system*, 2024.
- [G] M. Müllenbach*, S. Geier*, A. **Braemer**, T. Franz, G. Zürn, M. Weidemüller, and M. Gärttner, *Detecting operator spreading in Rydberg quantum simulators*, In preparation.

CONTENTS

1	Introduction	1
I	Pair localization in spatially disordered Heisenberg spin models	
2	Concepts: Thermalization and absence thereof	5
2.1	Thermalization	5
2.1.1	Prethermalization	5
2.2	Many-body Localization (MBL)	5
2.2.1	L-bit picture	5
2.2.2	Does MBL exist?	6
2.2.3	Long-range	6
2.2.4	Localization in long-range, bond-disordered systems	
		7
3	Cold Rydberg gases as experimental platform	9
4	Pair localization transition	11
5	Efficient time evolution of pair localized systems	23
6	Evidence of pair localization in dynamics of Rydberg spins	41
6.1	Anisotropy-independent relaxation dynamics	41
6.2	Emergent pair localization	55
6.2.1	Simple physical picture	69
7	Outlook	73
7.1	OTOCs	73
7.2	Disorder-averaged, effective time evolution	73
7.3	?Limitations of RSRG?	73
8	Discussion	75
II	Periodically driven quantum systems with spatial inhomogeneity	
9	Concepts: time crystals in Floquet systems	79
9.1	Floquet systems	79
9.2	Thermalization in Floquet systems	79
9.3	Time crystals	79
10	Spatially-varying drive	81
11	Outlook: Observation of a time crystal in the Rydberg Experiment?	93
12	Discussion	95
III	Summary	
13	Summary	99
	Bibliography	101

LIST OF FIGURES

Figure 2.1	Schematic of the l-bit picture.	5
Figure 2.2	Schematic of the avalanche thermalization.	6
Figure 2.3	Maybe schematic of the resonance counting? Take from yao paper (with permission)?	7
Figure 2.4	Schematic of pair localization	7
Figure 3.1	Increasing density reduces the randomness in the distances by forcing atoms closer together.	9
Figure 6.1	Steady-state magnetization curves of the sim- ple two-component model using the same color scheme as Fig. 2 (d) and (e) of [C]. Parameters, α and d correspond to (a) Fig. 2 (b) Fig. 4. The inset show a zoom around $\Omega = 0$ to highlight the qualitative difference between the curves. 71	71

NOTATION

We will work with natural units $\hbar = k_B = c = 1$. Furthermore, we will denote matrices as uppercase letters O , operators as boldface letters \mathbf{O} , vectors using arrows \vec{o} and scalars as lowercase letters o . In special instances, we will use a calligraphic font, such as \mathcal{H} to denote Hilbert spaces. All other notation is explained at the first point of occurrence.

INTRODUCTION

Let's cite everything [A–F]. And some more [1, 2].

Classical ice cream always melts, when forgotten on a table or, as a physicist might say, it thermalizes as do all classical systems without too many conservation laws. However, in the quantum realm things might be more complicated. While it is observed that in fact most quantum systems will reach some sort of equilibrium, it is generally poorly understood whether this state can be considered thermal.

Classical equations of motion are reversible, chaos, ergodicity, phase space configurations, statistical mechanics, thermalization is a statistical effect, gas in box with divider

Quantum equation of motion/Schrödinger equation is also reversible, unitary evolution, no direct notion of phase space with probability distribution, only quasi-probability. Quantum chaos, OTOCs, ergodicity
Insight: Cannot expect thermalization for all things, e.g. projectors on eigenstates of the Hamiltonian are conserved. Only local observables thermalize, e.g. magnetization. Can show that dephasing between eigenstates leads to equilibration, but this can be exponentially slow in principle. So why do we see rapid thermalization?

ETH: all eigenstates are look locally thermal, i.e. all eigenstates expectation values are a smooth functions of the eigenstate energy. It follows, if the initial state is reasonably sharp in energy, then the dephasing between eigenstates leads to rapid thermalization. Rapid because eigenstates close already have the same value and eigenstates far apart dephase quickly.

The corresponding dynamical picture: The dynamics cause rapid build-up entanglement in the system, which distributes the initially local information across the whole system, so it cannot be recovered locally. In this sense entanglement is the main driver behind thermalization.

Disordered systems, glasses break ergodicity.

Part I

PAIR LOCALIZATION IN SPATIALLY DISORDERED HEISENBERG SPIN MODELS

2

CONCEPTS: THERMALIZATION AND ABSENCE THEREOF

2.1 THERMALIZATION

equilibration is generic: [3, 4]

thermalization from first principles: ETH [5–7]

reviews: [8–11]

experiments?

Interestingly, even in ordered system for $\alpha < 1$ ETH is violated [12].

2.1.1 Prethermalization

review: [11]

2.2 MANY-BODY LOCALIZATION (MBL)

Seminal work by Anderson [13]

2.2.1 L-bit picture

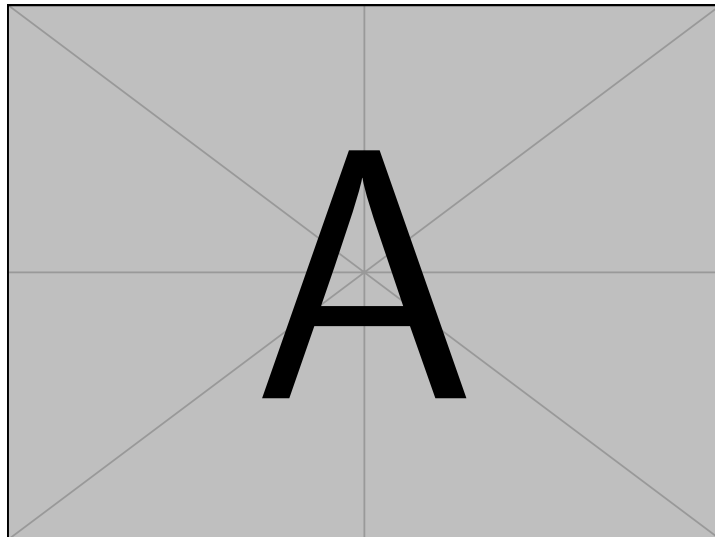


Figure 2.1: Schematic of the l-bit picture.

phenomenology review: [14]

Still number entropy can grow albeit very slowly [15, 16]

Entanglement entropy similarly [17], proven later [18]

Interactions can help[19]

2.2.2 Does MBL exist?

Existence proof (TFIM): [20]

However, MBL might be finite size

Avalanche thermalization

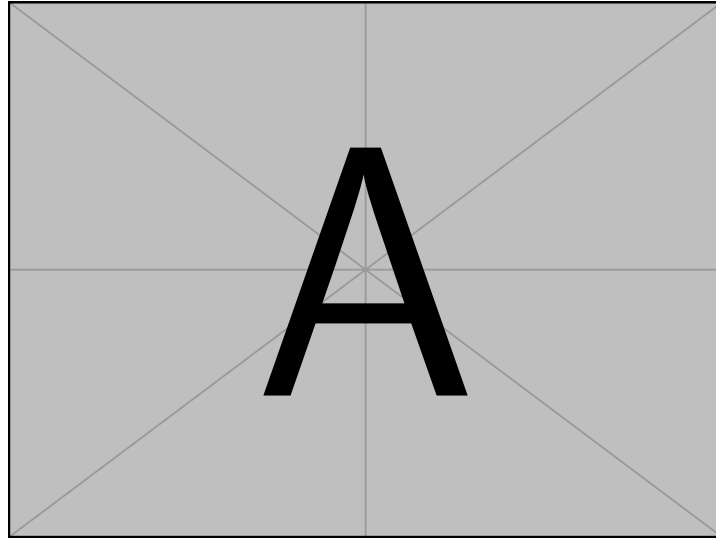


Figure 2.2: Schematic of the avalanche thermalization.

2.2.3 Long-range

heuristic resonance counting, no MBL for $\alpha \leq d$ in XXZ [21–23] or Anderson model [24] with somewhat mixed behavior for $\alpha \leq 2d$ (Anderson localization at zero temperature, other pair forms for Yao XXZ). Refined by [25] for XX model to $\alpha > \frac{3d}{2}$.

Powerlaw with random on-site potentials chain:

[26] confirm MBL using dynamics, half-chain entanglement entropy grows with $1/\alpha$. Different critical α_c for XX ($\alpha_c \sim 1$) and XXX ($\alpha_c \sim 2$). [27] confirm MBL using spectral indicators (half-chain entropy, level spacing ratio, variance of HCE). Find $\alpha_c \approx 1.16 \pm 0.17$. Mobility edge found in[28].

These works conceptually continue the random potential line of thought and just tack on some powerlaw interactions with random coefficients. This is a different regime than what I study where the main disorder does not stem from random potentials but is due to widely varying interaction strengths. To make this difference clear, I note that without random fields, these early works claim MBL to be impossible, as any spin is resonant with every other spin. However, RSRG tells us that each spin effectively interacts with its *strongest* resonant partner. Their fast interaction then effectively decouples the pair from the rest

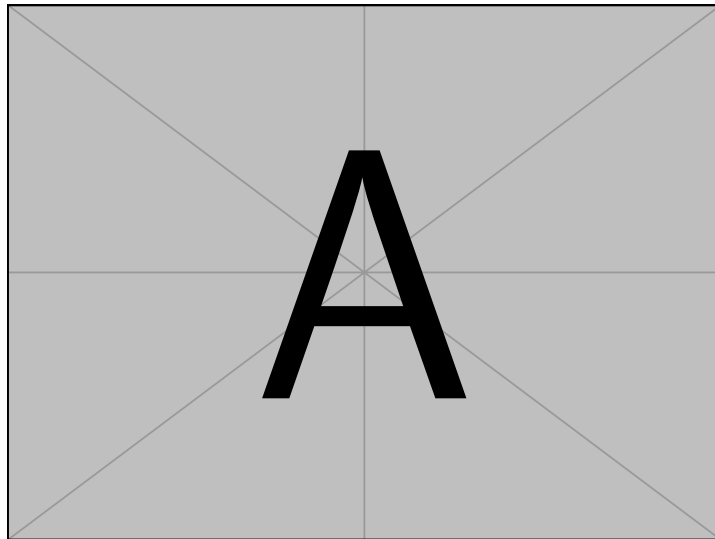


Figure 2.3: Maybe schematic of the resonance counting? Take from yao paper (with permission)?

of the spins. That's why this resonance counting is not relevant for localization for truly bond-disordered systems and raises the question about possible differences between random field models with some random long-range interaction and bond-disordered models with some random fields.

2.2.4 Localization in long-range, bond-disordered systems

Long-range bond-disorder: [29–31]

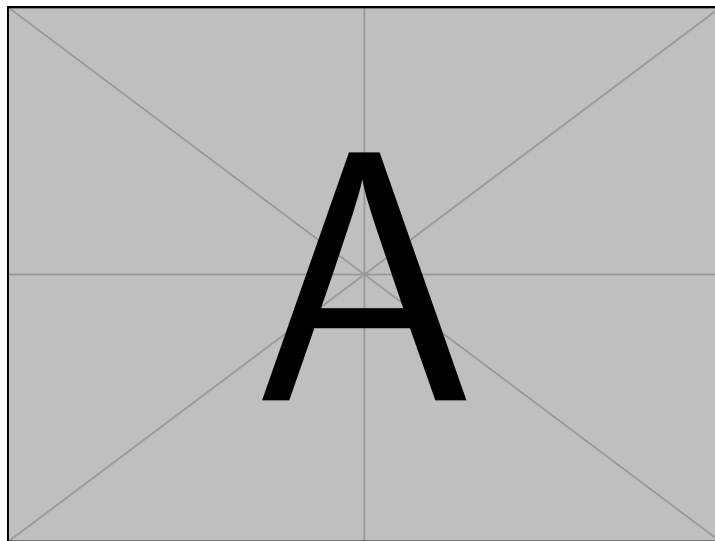


Figure 2.4: Schematic of pair localization

3

COLD RYDBERG GASES AS EXPERIMENTAL PLATFORM

highly excited atomic states, like small dipoles (bar magnets) with quantum properties

highly tunable, long-coherence times

Rydberg blockade, tunable disorder

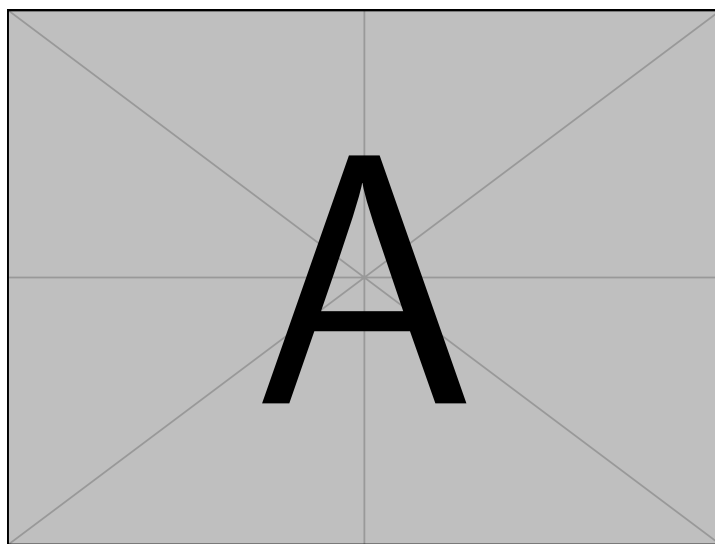


Figure 3.1: Increasing density reduces the randomness in the distances by forcing atoms closer together.

dipolar exchange interaction, Heisenberg hamiltonian

4

PAIR LOCALIZATION TRANSITION

Natural first question: Does this system exhibit a localization transition? If so: what are the conserved quantities? To tackle this question, we study the level-spacing ration, the half-chain entanglement entropy of eigenstates, Thouless parameters with respect to different local observables and participation ratios with different bases.

Pair localization in dipolar systems with tunable positional disorder

Adrian Braemer^{1,*}, Titus Franz^{1,†}, Matthias Weidemüller^{1,‡}, and Martin Gärttner^{1,2,3,†}

¹Physikalisches Institut, Universität Heidelberg, Im Neuenheimer Feld 226, 69120 Heidelberg, Germany

²Kirchhoff-Institut für Physik, Universität Heidelberg, Im Neuenheimer Feld 227, 69120 Heidelberg, Germany

³Institut für Theoretische Physik, Universität Heidelberg, Philosophenweg 16, 69120 Heidelberg, Germany



(Received 30 July 2022; accepted 16 October 2022; published 31 October 2022)

Strongly interacting quantum systems subject to quenched disorder exhibit intriguing phenomena such as glassiness and many-body localization. Theoretical studies have mainly focused on disorder in the form of random potentials, while many experimental realizations naturally feature disorder in the interparticle interactions. Inspired by cold Rydberg gases, where such disorder can be engineered using the dipole blockade effect, we study a Heisenberg XXZ spin model where the disorder is exclusively due to random spin-spin couplings, arising from power-law interactions between randomly positioned spins. Using established spectral and eigenstate properties and entanglement entropy, we show that this system exhibits a localization crossover and identify strongly interacting pairs as emergent local conserved quantities in the system, leading to an intuitive physical picture consistent with our numerical results.

DOI: [10.1103/PhysRevB.106.134212](https://doi.org/10.1103/PhysRevB.106.134212)

I. INTRODUCTION

Understanding how an isolated quantum system prepared out of equilibrium can exhibit thermal properties at late times, i.e., how it thermalizes, has challenged quantum physicists for almost a century. The eigenstate thermalization hypothesis (ETH) [1,2] offers a generic mechanism to explain this phenomenon but makes strong assumptions on the structure of energy eigenstates in terms of the matrix elements of local operators. Nonetheless, it has been shown numerically that a large class of quantum systems complies with ETH and thermalizes [3,4]. A notable exception are strongly disordered systems in which transport is absent and the system retains memory of the initial state at arbitrary times [5–8].

This phenomenon, called many-body localization (MBL), has been verified for small systems including, but not limited to, spin systems with random potentials [9–11], random nearest [12–14], and next-nearest-neighbor interactions [15,16], and power-law interactions [17–21] using a combination of exact numerical approaches and heuristic arguments like the strong disorder renormalization group (SDRG) [22–25] to generalize to large systems.

Recently, claims have been made that this localization phenomenology may not be stable in the thermodynamic limit due to thermal inclusions [26–34]. These are small, more ordered subregions thought to thermalize with their surroundings and thus slowly pushing the system toward thermalization. Unfortunately, these regions are very rare and thus only start appearing in large systems far beyond the reach of numerical methods. This raises the question whether this instability is relevant for quantum simulation experiments, being finite in

size and limited by coherence time. In this paper, we only focus on the phenomenology of localization in finite systems and subsequently use the term localized regime instead of a phase, following the terminology of Ref. [28].

Complementary to numerical works, there are a number of experimental results falling into roughly two classes: Experiments with single-particle resolution, including optical lattices [35–38] and trapped ions [39], and experiments based on macroscopic samples, like NV centers in diamond [40] or NMR systems [41]. The former offer precise control, but are rather limited in size, while the latter can realize much larger systems at the expense of flexibility, in particular, lack of programmable disorder. Cold gases of Rydberg atoms implement dipolar dynamics with random couplings (similar to NMR systems or NV centers) and allow for control of the disorder strength and even the power law of the interaction at rather large particle numbers [42], which makes them a powerful platform for studying localization phenomena.

Motivated by recent progress on quantum simulations with Rydberg atoms [42–45], we consider a power-law interacting spin system where the disorder is due to randomly positioned spins respecting a blockade condition, which induces disordered couplings. In this setup, the strength of the disorder can be tuned by changing the density of particles or, equivalently, the minimal distance between them. Starting in an ordered system, where the blockade radius is of order of the mean interparticle distance, we show numerically that this system exhibits a crossover to a localized regime at small blockade and apply a SDRG approach to derive a simple model based on strongly interacting pairs, which captures the properties of the eigenstates in the localized regime well. Our study thus adds to the body of numerical works on MBL, focusing on dipolar systems with tunable positional disorder, and is highly relevant to experimental efforts, as a wide range of quantum simulation platforms feature dipolar interactions.

*adrian.braemer@kip.uni-heidelberg.de

†martin.gaerttner@kip.uni-heidelberg.de

II. LOCALIZATION IN A RYDBERG GAS

A. System

We consider the Heisenberg XXZ spin model described by the Hamiltonian ($\hbar = 1$)

$$\hat{H} = \frac{1}{2} \sum_{i \neq j} J_{ij} \underbrace{\left(\hat{S}_x^{(i)} \hat{S}_x^{(j)} + \hat{S}_y^{(i)} \hat{S}_y^{(j)} + \Delta \hat{S}_z^{(i)} \hat{S}_z^{(j)} \right)}_{\equiv H_{\text{pair}}^{(i,j)}}, \quad (1)$$

where $\hat{S}_{\alpha}^{(k)}$ (with $\alpha \in \{x, y, z\}$) denotes the spin- $\frac{1}{2}$ operators acting on the k th spin. The coupling J_{ij} between spins i and j at positions x_i and x_j is given by $J_{ij} = \frac{C_{\alpha}}{|x_i - x_j|^{\alpha}}$, where C_{α} is an interaction coefficient which we set to $C_{\alpha} = 1$. In experimental realizations of this model with Rydberg atoms, the values of the anisotropy parameter Δ and interaction exponent α are controllable via the choice of the Rydberg states encoding the two spin states. The cases $\alpha = 3$, $\Delta = 0$ (dipolar exchange) and $\alpha = 6$, $\Delta \approx -0.7$ (van der Waals) have been realized experimentally [42,44]. For typical cloud temperatures and timescales of the spin dynamics, the atom positions can be regarded as fixed (frozen gas approximation).

During the initial Rydberg excitation, the spins are subjected to the Rydberg blockade [46], which means no two spins can be closer than some distance r_b , called the blockade radius. This feature allows one to tune the strength of disorder via the sample's density: In a very dilute sample, the mean interspin distance is much larger than the blockade radius r_b and thus positions are essentially uncorrelated. In the other extreme, the spins are tightly packed and exhibit strong spatial correlations.

We quantify the strength of disorder by the ratio W of the system's total volume V over total blocked volume V_{block} or, equivalently, by the ratio of Wigner-Seitz radius a_0 , which is half of the mean interspin distance, to the blockade radius r_b to the power of the dimension d :

$$W = \frac{V}{V_{\text{block}}} = \left(\frac{a_0}{r_b} \right)^d. \quad (2)$$

For $d = 1$, the minimal value of $W_{\min} = \frac{1}{2}$ is attained for a translationally invariant chain with spacing $2a_0 = r_b$, as illustrated in Fig. 1(a).

B. Effective pair description

This model differs from the random field Heisenberg model, which has been studied extensively in the MBL literature, as no disordered potentials are considered. Thus it may not be immediately apparent why this system features localization and what constitutes the local conserved quantities akin to the l -bits [47] in the standard scenario. Here we provide a phenomenological picture in the spirit of the SDRG, suggesting that localization should appear due to strongly interacting pairs.

Consider a strongly disordered cloud of N spins described by Eq. (1) like the example depicted in Fig. 1(b). Due to the power-law interactions, coupling strengths vary strongly between different pairs of atoms, symbolized by the width and brightness of the green lines. This motivates us to employ a perturbative treatment, in which we single out the strongest

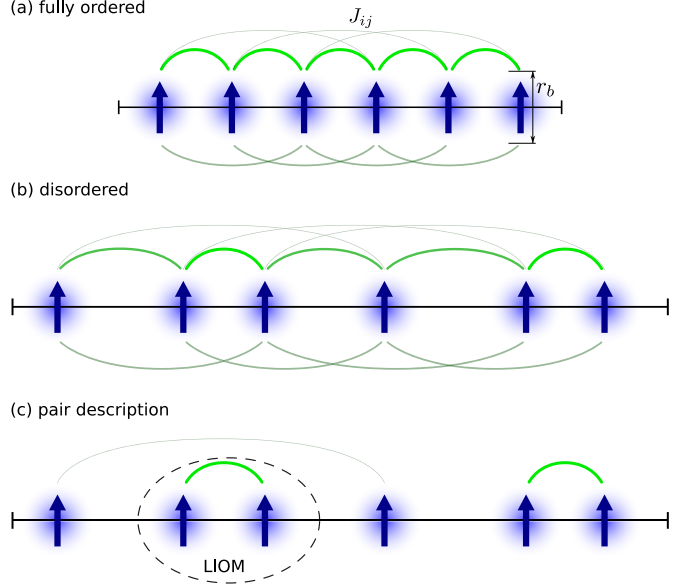


FIG. 1. Pair description. The blockade constraint (blue shadings) enables tuning of disorder in the couplings (green lines) from fully ordered (a) to disordered (b). In the latter case, a perturbative treatment to first order yields a description in terms of strongly correlated pairs (c) subject to an Ising-like interaction (not depicted). These pairs constitute local integrals of motion (LIOM).

pair coupling and consider all other couplings as a perturbation. In the example shown in Fig. 1(b), the two rightmost spins share the strongest coupling and we can see that it is much stronger than the other couplings of either one of the spins to the rest of the system. Using perturbation theory to first order, we find that the pair of spins almost decouples from the rest of the system, leaving only an effective Ising-like interaction, which is unimportant for the further procedure and thus not shown in the figure. For details on the calculations involved, see Appendix A.

We may now repeat this procedure of eliminating couplings between the pairs and the rest of system by identifying the next strongest interaction among the remaining spins which, in this example, is the coupling between the second and third spin. Eliminating the respective couplings as well leaves us with the effective pairs shown in Fig. 1(c). Note that in an ordered system, as shown in Fig. 1(a), this perturbative treatment is not applicable as not all neglected couplings can be considered small. We also note that the order of eliminations is not important as long as each time the inner-pair coupling is much larger than the couplings between the pair and the rest. Concretely, for the given example, choosing the coupling between spins 2 and 3 in Fig. 1(b) first in the pair elimination process does not change the result.

The great advantage of this ansatz is that we can now give a simple description of the whole many-body spectrum. Diagonalizing H_{pair} [see Eq. (1)], we find two maximally entangled eigenstates $|\pm\rangle = 1/\sqrt{2}(|\uparrow\downarrow\rangle \pm |\downarrow\uparrow\rangle)$ at energies $E_{\pm} = \pm 2 - \Delta$ and two degenerate states $|\uparrow\uparrow\rangle, |\downarrow\downarrow\rangle$ at energy $E_d = \Delta$, which we will refer to as $|\uparrow\uparrow\rangle, |\downarrow\downarrow\rangle$. The Ising-like interaction between pairs does not act on the entangled states $|\pm\rangle$ and is diagonal with respect to $|\uparrow\uparrow\rangle, |\downarrow\downarrow\rangle$. Thus, in the pair picture, the

eigenstates of the full system are now given by tensor products of these four pair eigenstates. We refer to this basis as the pair basis.

In the many-body spectrum, the degeneracy between the pair states $|\uparrow\uparrow\rangle$ and $|\downarrow\downarrow\rangle$ is lifted due to the emerging Ising-like interaction. However, we note that this splitting is small compared to the splitting between the other pair eigenstates as it emerges from first-order perturbation theory.

The pair picture is analogous to the l -bit picture often used in MBL, where strong local disorder potentials lead to the emergence of quasilocal conserved quantities $\hat{\tau}^{(i)} \sim \hat{\sigma}_z^{(i)}$ [47,48]. Here, we see that each projector on a pair's eigenstate constitutes an approximately conserved quantity and hence is a local integral of motion (LIOM). Thus, we established a description akin to the l -bit picture of MBL for this disordered Heisenberg model, where the role of LIOMs is taken by strongly interacting pairs.

While this ansatz is heuristic and neglects all higher resonances, that may play a crucial role in delocalizing the system, it will nonetheless turn out to be useful for interpreting and understanding the spectral and eigenstate properties reported in the following.

III. NUMERICAL RESULTS

To minimize boundary effects, we consider a one-dimensional system with periodic boundary conditions [49] of up to $N = 16$ spins governed by Eq. (1) and perform exact diagonalisation on the sector of smallest positive magnetization. We fix the interaction exponent to $\alpha = 6$, corresponding to a Van der Waals interactions, and set $\Delta = -0.73$ (cf. Ref. [42]). We do not expect a strong dependence of our results on the precise value of Δ as long as one steers clear from regions around points where additional symmetries emerge.

For each disorder strength W , we generate 2000 configurations of random spin positions, perform a full diagonalization and compute several well-established indicators for the localization transition from the spectrum. We always average over all eigenstates/-values as restricting to the bulk of the spectrum does not lead to qualitative changes in the observed behavior. The statistical error resulting from disorder averaging is smaller than the thickness of the lines in all figures unless indicated otherwise. For a description of the algorithm for choosing the configurations, we refer to Appendix C. All code used for this paper can be found in Ref. [50].

The following sections discuss different indicators of localization with the aim to establish the localization crossover in this model and employ the pair model for interpretation and predictions. The last section directly compares the pair basis to the eigenstates, thus demonstrating its validity.

A. Level spacing ratio

The spectral average of the level spacing ratio (LSR), defined as [51]

$$\langle r \rangle = \frac{1}{|\mathcal{H}|} \sum_n \min \left(\frac{E_{n+2} - E_{n+1}}{E_{n+1} - E_n}, \frac{E_{n+1} - E_n}{E_{n+2} - E_{n+1}} \right), \quad (3)$$

is a simple way of characterizing the distribution of differences between adjacent energy levels. For thermalizing

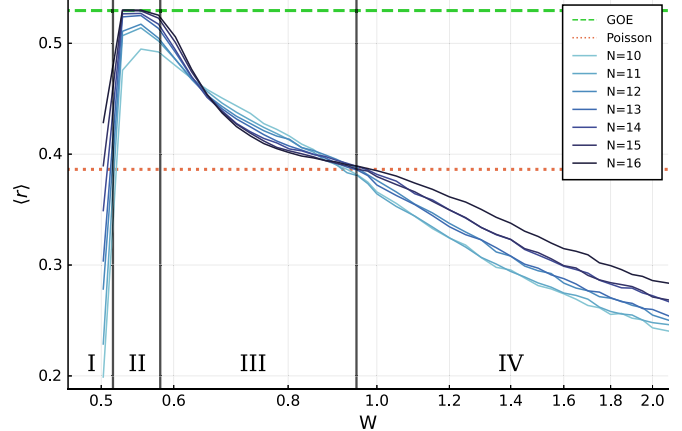


FIG. 2. Level-spacing ratio. With increasing disorder, the LSR shows a crossover from an ergodic value to its Poissonian value and below. We identify four major regions where the physics is governed by (I) translational symmetry breaking, (II) thermal behavior, (III) the localization crossover and (IV) localization. The horizontal lines show random-matrix theory predictions.

(ergodic) systems, the Hamiltonian is expected to show a mean LSR resembling a random matrix from the Gaussian orthogonal ensemble because its eigenvectors essentially look like random vectors. Thus one can use random matrix theory to obtain $\langle r \rangle_{\text{thermal}} = 4 - 2\sqrt{3} \approx 0.536$ [52].

On the other hand, in localized systems the eigenvalues follow a Poisson distribution, since they are essentially sums of randomly distributed energies from the l -bits the system consists of. Computing the mean LSR in this case yields $\langle r \rangle_{\text{MBL}} = 2 \ln 2 - 1 \approx 0.386$ [52].

Comparing with the numerical results in Fig. 2 and focusing on the central parts first, we find the mean LSR reaches its thermal value for large enough systems and weak disorder (II) dropping toward the Poissonian value for stronger disorder (III). With growing system size, the thermal plateau (II) broadens, marking a parameter region where the system appears ergodic. But while the plateau broadens, the drop-off (III) for increasing disorder strength becomes steeper, meaning the crossover becomes sharper as the system gets larger.

Considering very strong disorder (IV), the mean LSR drops even below the Poissonian value, which indicates level attraction. This effect can be explained by the pair model: As stated earlier, the $|\uparrow\uparrow\rangle$ and $|\downarrow\downarrow\rangle$ states' degeneracy is lifted by the effective Ising-like terms from first-order perturbation theory, which means the split is of smaller magnitude compared to the intra-pair interactions. For small systems with comparatively low spectral density, this means that the small lifting likely fails to mix the formerly degenerate states into their surrounding spectrum. Thus, the LSR still reflects the near degeneracy within the pairs, leading to level attraction. Based on this interpretation, we expect this effect to diminish for larger systems with the spectral density growing. In fact, this trend is already visible in Fig. 2.

A similar argument can be made at very weak disorder (I): Here the source of the degeneracy is the proximity to the perfectly ordered case at $W = 0.5$, which has an additional translation invariance. Weak disorder breaks that symmetry

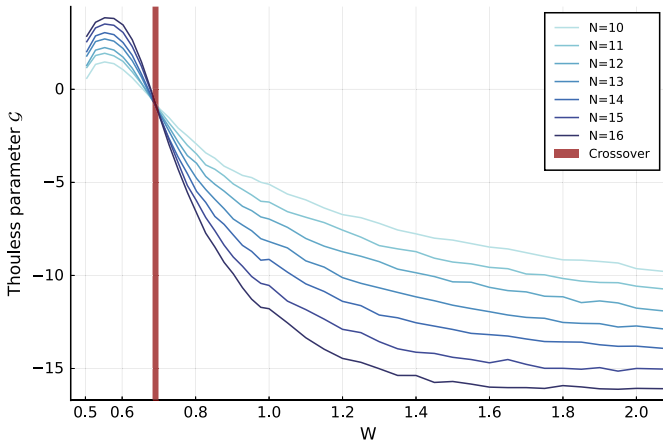


FIG. 3. Thouless parameter. Spectral and disorder averaged \mathcal{G} versus disorder strength W . Data shown uses local operator $\hat{V}_1 = 2\hat{S}_z^{(1)}$

but couples the symmetry sectors only weakly, leading again to a very small energetic splitting of degenerate states. We want to emphasize the reason for level attraction being very different in nature in (I) and (IV): Whereas in (I) the system is close to a system with obvious conserved quantities due to symmetries, in (IV) there is the emergent integrability of the MBL regime [8]. Nevertheless, we expect region (I) to become less pronounced for larger systems continuing the trend visible in Fig. 2.

We conclude that, in analogy to standard MBL, we find a crossover in the level spacing distribution from a regime with level repulsion to Poissonian gaps indicating a localization crossover. At very strong disorder, we even find a region with level attraction, the source of which can be explained by the effective pair model.

B. Thouless parameter

Complementary to eigenvalue statistics, we also probe eigenstate properties by computing the Thouless parameter

$$\mathcal{G}_n = \ln \frac{|\langle n | \hat{V} | n+1 \rangle|}{E'_{n+1} - E'_n}, \quad (4)$$

introduced by Serbyn *et al.* [53]. This quantity is akin to the Thouless conductance in single particle systems and quantifies how well two states $|n\rangle, |n+1\rangle$ with perturbed energies $E'_n = E_n + \langle n | V | n \rangle$ are coupled by a local perturbation \hat{V} . In the thermal phase, states of similar energy will have similar spatial structures, whereas in the localized phase, eigenstates are products of LIOM eigenstates and thus typically vary drastically from one to the next. One can derive the scaling of the average \mathcal{G} in the thermal regime to be $\mathcal{G} \propto \log |\mathcal{H}|$ and in the localized regime to be $\mathcal{G} \propto -\log |\mathcal{H}|$, leading to the natural definition of the location of the crossover to be the point where $\mathcal{G} = \text{const}$ [53].

Figure 3 shows results using local operator $\hat{V}_1 = 2\hat{S}_z^{(1)}$. Data for local operators $\hat{V}_2 = 4\hat{S}_z^{(1)}\hat{S}_z^{(2)}$ and $\hat{V}_3 = \hat{S}_+^{(1)}\hat{S}_-^{(2)} + \text{H.c.}$ is visually identical. There is a very clear point where all curves intersect each other, indicating the crossover's location.

To the right of the crossing point in the localized regime, the curves are roughly evenly spaced, reflecting the expectation of $\mathcal{G} \propto -\log |\mathcal{H}|$, clearly signaling the localized regime. The apparent absence of a drift of the transition point with system size is in contrast to observations in power-law interacting models with on-site disorder and will be further discussed in the next subsection.

C. Half-chain entropy

Having shown the presence of a localization crossover, we now demonstrate that our effective pair model is indeed a good approximation. We start by probing the half-chain entropy, $S = -\text{Tr} \rho_A \log_2 \rho_A$, with $\rho_A = \text{Tr}_B(\rho)$, i.e., the entanglement entropy between two halves of the chain. For that, we select $\lfloor \frac{N}{2} \rfloor$ consecutive spins and trace out the rest, resulting in two cuts due to the periodic boundary conditions, and average over all N possible choices of connected subsystems and all eigenstates.

In an ergodic system, all bulk states should exhibit volume-law entanglement, meaning $S \propto N$. In contrast, in a localized setting all states show area-law entanglement, which for $d = 1$ means $S = \text{const}$ [3,54].

To compute the half-chain entropy predicted by the pair model, we need to determine how many pairs are divided by each cut and how often these pairs are found in one of the entangled states $|\pm\rangle = 1/\sqrt{2}(|\uparrow\downarrow\rangle \pm |\downarrow\uparrow\rangle)$. Not all pairs consist of adjacent spins [see Fig. 1(c)], so a cut can separate more than one pair. The amount of cut bonds is easily determined from the position data alone by adding up the distances between paired spins. Respecting periodic boundary conditions of the system yields an additional factor of 2, since there are two cuts needed to divide the chain.

Considering the entropy contribution of a single bond, if we were to average over all possible configurations of pair states, each cut bond would contribute half a bit of entanglement on average, as half of the pair states are maximally entangled and the other half not entangled at all. However, here we consider the sector of smallest positive magnetization, which yields a slightly larger entropy, because it favors the entangled states $|\pm\rangle$ (which have zero net magnetization) over the fully polarized ones. This modification can be computed exactly (see Appendix B for details).

Taking into account both the effects of extended pairs and of the fixed total magnetization, we can compute a prediction for the entanglement entropy directly from the interaction matrix J_{ij} . Figure 4 shows both the numerically computed values for different system sizes (solid) and pair-model prediction (dashed).

We clearly see the change between the ergodic and localized regime for the numerically computed data. For strong disorder, all lines collapse, confirming on one hand the area law entanglement expected in the localized phase and, on the other hand, validating the pair model as it predicts the strong-disorder limit with high accuracy. Figure 4(b) magnifies the strong-disorder regime showing that the pair-model prediction in fact slightly overestimates the half-chain entropy for very strong disorder. This might indicate that there are spins that do not pair up perfectly, not forming a maximally entangled Bell pair. It is plausible that this happens at late stages of the

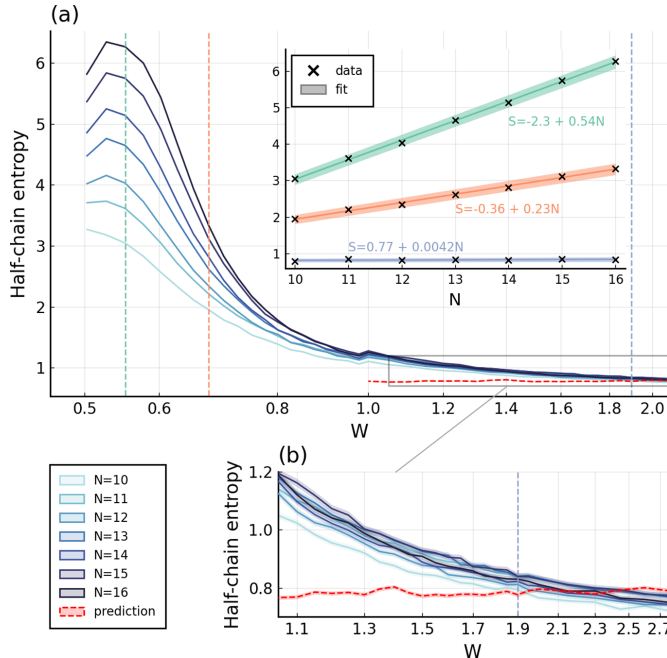


FIG. 4. Half-chain entropy. Average over possible cut locations and over disorder realizations for different system sizes as a function of disorder strength. Also shown is the prediction derived from a pair description, computed from position data for $N = 16$ (red dashed line), see B for details. Inset: Linear fits at fixed disorder strengths indicated by the vertical dashed lines in the main panel. Shaded areas indicate uncertainty from the fit; (b) magnifies the strongly disordered regime of (a). Shaded areas indicate statistical uncertainty from disorder averaging.

pair elimination procedure described in Sec. II B when the spins of a pair can have couplings that are stronger than the pair's internal coupling but the spins associated with these stronger couplings are already eliminated. We thus interpret this feature as an indication of the limitations of a simple pair description.

Another piece of information that we can readily access via the half-chain entropy is the location of the crossover. To determine it, we calculate the variance of the half-chain entropy over different disorder realizations and extract the maximum for each chain length N via a quadratic fit [15,55]. Figure 5 shows no strong dependence of the crossover point on N in the range of accessible system sizes. Indeed, the crossover does not seem to drift significantly, which is in contrast to models with onsite disorder, see, e.g., Refs. [18,55,56], where finite-size drifts of the transition point are commonly observed.

Interestingly, the crossover location is very close to the density given by Rényi's parking constant, or jamming limit, which is the maximal density attainable by randomly placing nonoverlapping unit intervals on the number line [57]. As in experiments with Rydberg spins, atom positions result from such a random process; this could imply that these experiments might not be able to reach the densities required for observing the fully ergodic regime. However, it is unclear how the crossover location generalizes to higher dimensions and larger systems.

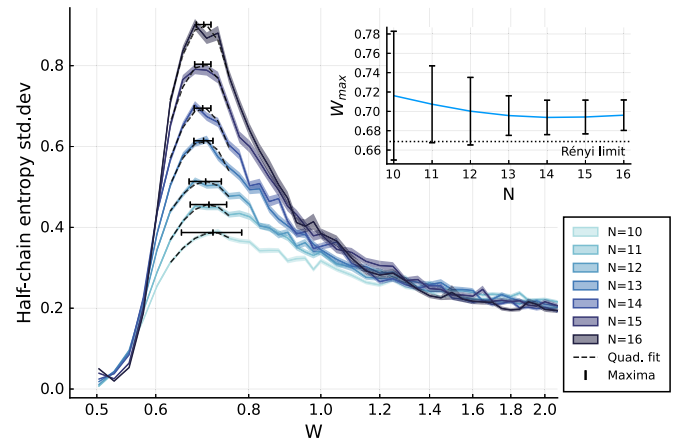


FIG. 5. Standard deviation of half-chain entropy. The main plot shows the standard deviation of the half-chain entropy across disorder realizations exhibiting a clear maximum around which a quadratic polynomial is fitted. Shaded areas indicate statistical uncertainty. Inset: Position of the maximum as extracted by the fits. Errors shown are statistical errors from the fits.

D. Participation ratio

Now that we have seen that the pair model captures the spatial entanglement structure of the exact eigenstates, we compare the predicted eigenstates directly to the exact ones by computing the participation ratio (PR). Intuitively, it measures how many states of a reference basis $\mathcal{B} = \{|b\rangle\}$ contribute to a given eigenstate $|\phi_n\rangle$:

$$\text{PR}_{\mathcal{B}}(|\phi_n\rangle) = \left(\sum_{b \in \mathcal{B}} |\langle b | \phi_n \rangle|^4 \right)^{-1}. \quad (5)$$

Usually, in the MBL context, one chooses a product basis as reference because a low PR relative to product basis means the eigenstates are close to product states. “Low” in this context means a sublinear scaling of PR with the dimension of the Hilbert space \mathcal{H} : $\text{PR} \propto |\mathcal{H}|^\tau$, where $\tau < 1$. In contrast, a thermalizing system always has $\text{PR} \propto |\mathcal{H}|$ with respect to any product basis [58–60].

Here we compare two different reference bases, the z -basis $\mathcal{Z} = \{|\uparrow\rangle, |\downarrow\rangle\}^{\otimes N}$ and the pair basis $\mathcal{P} = \{|\pm\rangle, |\uparrow\downarrow\rangle\}^{\otimes N/2}$, introduced above, to determine how well the pair model describes the eigenstates. If the pair basis \mathcal{P} was exactly equal to the eigenbasis, its PR would be exactly 1. In this case, the expected PR with respect to the z -basis, averaged over the Hilbert space, \mathcal{Z} will be $1.5^{N/2}$, because a single pair has an average PR of 1.5. However, we only consider the sector of smallest positive magnetization, which increases the expected PR by a similar line of reasoning as for the entropy in the previous section.

Figure 6(a) shows the PR relative to the two reference bases as a fraction of the Hilbert space dimension $|\mathcal{H}|$. We see that the weakly disordered regime indeed has ergodic eigenstates as the curves collapse onto each other. The small offset between the two reference bases is plausible, since a thermal systems eigenstates express volume law entanglement and thus the overlap with a product basis like \mathcal{Z} is minimal. The states of the pair basis contain pairwise entanglement and

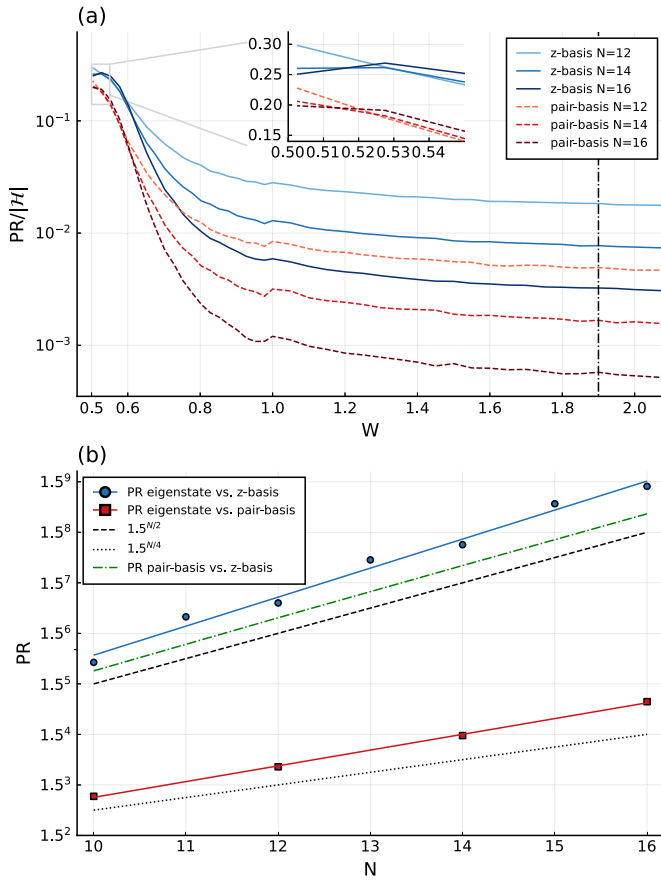


FIG. 6. Participation ratio. (a) PR relative to Hilbert space dimension $|\mathcal{H}|$ for different reference bases: z -basis in blue, pair basis in red. The inset shows a magnification of the region toward perfectly ordered systems. (b) shows the growth in absolute PR with increasing system size in the localized regime. The used value of W is indicated by the dash-dotted line in (a).

are thus a bit closer, which manifest as slightly lower PR. Around $W = 0.6$, the scaling with $|\mathcal{H}|$ starts to change to a sublinear relation as we crossover to the localized regime.

Checking the PR deep in the localized phase (at $W = 1.9$) in Fig. 6(b), we can see that the PR relative to the z -basis (blue line) is slightly, but systematically, larger than the pair model's prediction (dashed green line). Consistent with this observation, we see that the PR relative to the pair basis (red line), while being much smaller, is still not constant across system sizes.

We conclude that the pair states offer a good first-order approximation of the true eigenstates, but there are higher order resonances that lead to further hybridization for some states. The exponent of the remaining dependence on system size is close to $N/4$, which hints at effects stemming from interactions between pairs.

IV. CONCLUSIONS

We analyzed a disordered Heisenberg XXZ spin model with power-law interaction and positional disorder, which is naturally realized by many quantum simulation platforms. Among these, cold Rydberg gases allow for easy tuning of the

disorder via the sample's density due to the Rydberg blockade. By using standard MBL indicators, we showed numerically that this system undergoes a localization crossover, which we interpreted in terms of a simple physical model derived using an SDRG ansatz. This model, consisting of an effective Ising model of strongly interacting pairs of spins, was verified by considering the PR of eigenstates with the conjectured basis, which is drastically reduced compared to the PR relative to the z -basis. Still, there was a weak dependence on system size left, which means there are higher order corrections to our model. Nonetheless, we also showed that this simple model can already predict the entanglement entropy of the system nearly perfectly.

With this model at hand, we can now make predictions for large systems which may be tested in quantum simulation experiments. Of course, one of the most interesting questions will be whether the location of the crossover shifts toward stronger disorder for large systems, indicating a transition at infinite disorder strength in the thermodynamic limit. For this purpose, the easy tunability of the disorder is a great advantage as both sides of the crossover can be probed on the same platform by changing the system parameters. Remarkably, our small-scale numerical study showed almost no finite-size drift. This could indicate that localization in this model is more stable than in similar models against resonances. We leave this investigation for future work.

Note that the pair model cannot be used to predict the crossover itself as it essentially requires the assumption that one can find strongly interacting pairs, which is only justified in the strongly disordered regime. Recent arguments for the absence of localization postulate the existence of rare thermal subregions within the system [26,26–34]. This would of course break the base assumption of the pair model. A possible direction for future research would be to extend the model to include not only pairs but also larger clusters, which would require one to track all kinds of interactions between clusters of different sizes.

Interestingly, the dimensionality of the system does not directly influence the pair model. As long as the couplings are sufficiently disordered, such that pairs can be defined, it will be a good approximation. Thus, it suffices to study how the distribution of couplings changes with respect to the dimensionality d of the space and coupling power α . Similar to resonance counting arguments [61], we conjecture the requirement $d < \alpha$ for the pair model to be applicable. Hence, we expect our results, while acquired in $d = 1$, to generalize well to $d > 1$.

ACKNOWLEDGMENTS

We thank Dima Abanin for his stimulating input. For numerical simulations, we used the Julia programming language [62]. The authors acknowledge support by the state of Baden-Württemberg through bwHPC and the German Research Foundation (DFG) through Grant No. INST 40/575-1 FUGG (JUSTUS 2 cluster). This paper is supported by the Deutsche Forschungsgemeinschaft (DFG, German Research Foundation) under Germany's Excellence Strategy EXC No. 2181/1-390900948 (the Heidelberg STRUCTURES

TABLE I. Eigensystem of H_{pair} .

State k	Energy E_k	Vector $ k\rangle$
1	$2 - \Delta$	$\sqrt{2}^{-1}(\uparrow\downarrow\rangle + \downarrow\uparrow\rangle)$
2	Δ	$ \uparrow\uparrow\rangle$
3	Δ	$ \downarrow\downarrow\rangle$
4	$-2 - \Delta$	$\sqrt{2}^{-1}(\uparrow\downarrow\rangle - \downarrow\uparrow\rangle)$

Excellence Cluster) and under SFB 1225 ISOQUANT No. 273811115.

APPENDIX A: DERIVATION OF PAIR PICTURE

Here we derive the pair model of the main text by means of Schrieffer-Wolff transformations [63]. Starting with the full Hamiltonian of the system,

$$\hat{H} = \frac{1}{2} \sum_{i \neq j} J_{ij} \underbrace{(\hat{S}_x^{(i)} \hat{S}_x^{(j)} + \hat{S}_y^{(i)} \hat{S}_y^{(j)} + \Delta \hat{S}_z^{(i)} \hat{S}_z^{(j)})}_{\equiv H_{\text{pair}}^{(i)(j)}}. \quad (\text{A1})$$

Suppose without loss of generality that $J_{12} \gg J_{1j}, J_{2j}$ and set $H_0 = J_{12} H_{\text{pair}}^{(1)(2)}$ and $V = H_{XXZ} - H_0$. We label the eigenvectors and eigenenergies of H_{pair} as shown in Table I.

The projectors on these states are consequently named $P_k = |k\rangle\langle k| \otimes \mathbb{1}$, but since the middle two states are degenerate, we need to use the projector on the full eigenspace and call it $P_{23} = P_2 + P_3$.

To first order, only diagonal terms $P_k V P_k$ contribute, which in this case means the pair decouples and only an effective Ising term remains:

$$\hat{H} = \sum_{i,j} J_{ij} \hat{H}_{\text{pair}}^{(i)(j)} \quad (\text{A2})$$

$$\approx J_{12} \hat{H}_{\text{pair}}^{(1)(2)} + \sum_{i,j>2} J_{ij} \hat{H}_{\text{pair}}^{(i)(j)} + \hat{S}_z^{(1)(2)} \sum_{i>2} \tilde{\Delta}_i \hat{S}_z^{(i)} + O(\hat{V}^2), \quad (\text{A3})$$

where $2\hat{S}_z^{(1)(2)} = |\uparrow\uparrow\rangle\langle\uparrow\uparrow| - |\downarrow\downarrow\rangle\langle\downarrow\downarrow|$ is akin to a spin-1 magnetization operator and $\tilde{\Delta}_i = \Delta(J_{1i} + J_{2i})$ is the renormalized Ising coupling. Note that this first order term lifts the apparent degeneracy of the $|\uparrow\uparrow\rangle$ and $|\downarrow\downarrow\rangle$ states. This elimination is a good approximation if the interaction within the pair is much stronger than any other interaction between a spin of the pair and some other spin.

We can now repeat this elimination step with remaining spins by incorporating the effective Ising terms into V . This is justified because its coupling is small and is already first-order perturbation theory, and thus including it into the zeroth order of the next pair would mix expansion orders inconsistently.

Further eliminations now generate effective Ising terms between the states $|\uparrow\uparrow\rangle$ and $|\downarrow\downarrow\rangle$ of the eliminated pairs. After pairing up all spins, we find

$$\hat{H} = \sum_{i,j} J_{ij} \hat{H}_{\text{pair}}^{(i)(j)} \quad (\text{A4})$$

$$\approx \sum_{(i,j)} J_{ij} \hat{H}_{\text{pair}}^{(i)(j)} + \sum_{(i,j), (i',j')} \tilde{\Delta}_{(i,j), (i',j')} \hat{S}_z^{(i)(j)} \hat{S}_z^{(i')(j')} \quad (\text{A5})$$

where the sum over $\langle i, j \rangle$ denotes pairs of spins and $\tilde{\Delta}_{(i,j), (i',j')} = \Delta(J_{i,i'} + J_{j,i'} + J_{i,j'} + J_{j,j'})$.

Also note that with each elimination step, the mean interparticle distance grows and thus the disorder in the system increases [64,65] making it more likely for later elimination steps to be good approximations.

APPENDIX B: PAIR ENTROPY IN A SPECIFIC MAGNETIZATION SECTOR

Averaged over all states, each cut separating a pair gives an average entropy of $\frac{1}{2}$, since two of the pair's eigenstates are fully entangled and the other two possess no entanglement. However, when we consider a sector of fixed magnetization, this simple argument no longer holds as there are now dependencies among the eigenstates given by the external constraint. Sectors around zero magnetization will have more entropy on average and strongly magnetized sectors less, simply because the strongest magnetized eigenstates possess no entropy.

Given N the number pairs of spins where N_+ , N_- , and N_0 pairs occupy the states $|\uparrow\uparrow\rangle$, $|\downarrow\downarrow\rangle$, and $|\uparrow\downarrow\rangle \pm |\downarrow\uparrow\rangle$, we find the number of possible configuration with these amounts to be

$$C(N_+, N_-, N_0) = \binom{N}{N_0} \binom{N - N_0}{N_+} 2^{N_0}. \quad (\text{B1})$$

In the end, we need the number of configurations $\mathcal{C}(N, r) = \sum_{N_0} C(N, r, N_0)$ given a total amount of pairs N and a magnetization imbalance $r = N_+ - N_-$, where

$$\mathcal{C}(N, r, N_0) = \sum_{0 \leq N_+ \leq N} C(N_+, N_-, N_0) \delta_{N, N_+ + N_- + N_0} \delta_{r, N_+ - N_-}. \quad (\text{B2})$$

To evaluate this expression, we compute the generating function

$$\mathcal{Z}(x, y, z) = \sum_{N>0} x^N \sum_{-N \leq r \leq N} y^r \sum_{N_0>0} z^{N_0} C(N, r, N_0) \quad (\text{B3})$$

$$= \sum_{0 \leq N_+, N_-, N_0} x^{N_+ + N_0 + N_-} y^{N_+ - N_-} z^{N_0} C(N_+, N_-, N_0) \quad (\text{B4})$$

$$= \sum_{0 \leq N_-} \left(\frac{x}{y}\right)^{N_-} \sum_{0 \leq N_+} (xy)^{N_+} \binom{N_+ + N_-}{N_+} \times \sum_{N_0} \binom{N}{N_0} (2z)^{N_0} \quad (\text{B5})$$

$$= \frac{y}{y - 2xyz - xy^2 - x}, \quad (\text{B6})$$

where we used the fact that $(1-x)^{-k-1} = \sum_n \binom{n+k}{k} x^n$ twice and then a geometric series.

From that, it follows directly that

$$\mathcal{Z}(x, y, 1) = \sum_{N>0} x^N \sum_{-N \leq r \leq N} y^r \mathcal{C}(N, r) \quad (\text{B7})$$

$$= \frac{y}{y - 2xy - xy^2 - x} \quad (\text{B8})$$

$$= \frac{1}{1 - x \frac{(y+1)^2}{y}} \quad (B9)$$

$$= \sum_{0 \leq k} x^k \left(\frac{(y+1)^2}{y} \right)^k \quad (B10)$$

$$= \sum_{0 \leq k} x^k \sum_{0 \leq l \leq 2k} y^{l-k} \binom{2k}{l}, \quad (B11)$$

and thus by identification of terms

$$\mathcal{C}(N, r) = \binom{2N}{r+N}. \quad (B12)$$

Singling out a specific pair and asking how often it is in one of the entangled states given a set of configurations described by values for (N_+, N_0, N_-) , we find that its the case in

$$S(N_+, N_-, N_0) = 2C(N_+, N_-, N_0 - 1) = \frac{N_0}{N} C(N_+, N_-, N_0) \quad (B13)$$

configurations. Again we want to find this number for a total amount of pairs N and an magnetization imbalance $r = N_+ - N_-$. Fortunately, we can find the generating function $\mathcal{Z}_S(x, y, z)$ of $S(N, r, N_0) = \frac{N_0}{N} C(N, r, N_0)$ by means of \mathcal{Z} :

$$\mathcal{Z}_S(x, y, z) = \int \frac{dx}{x} z \frac{\partial}{\partial z} \mathcal{Z}(x, y, z). \quad (B14)$$

So, we compute

$$\mathcal{Z}_S(x, y, z=1) = \sum_N x^N \sum_r y^r \mathcal{S}(N, r) \quad (B15)$$

$$= \int \frac{dx}{x} \frac{2xy^2}{(y - x(y+1))^2} \quad (B16)$$

$$= \frac{2y^2}{(y+1)^2} \frac{1}{y - x(y+1)^2} \quad (B17)$$

$$= 2 \sum_k x^k \sum_l y^{l-k+1} \binom{2k-2}{l} \quad (B18)$$

$$\Rightarrow \mathcal{S}(N, r) = 2 \binom{2N-2}{r+N-1}. \quad (B19)$$

Thus, cutting a single pair contributes

$$\bar{\mathcal{S}}(N, r) = \frac{\mathcal{S}(N, r)}{\mathcal{C}(N, r)} \quad (B20)$$

$$= 2 \frac{N^2 - r^2}{4N^2 - 2N} \quad (B21)$$

bits of entropy, on average, over all states in a given magnetization sector (cf. Fig. 7).

For the prediction of the average entropy in Fig. 4, we extracted the size of the pairs from the position data, which directly determines how many times a pair is cut, when moving along the chain. The number of cut pairs is then divided by the

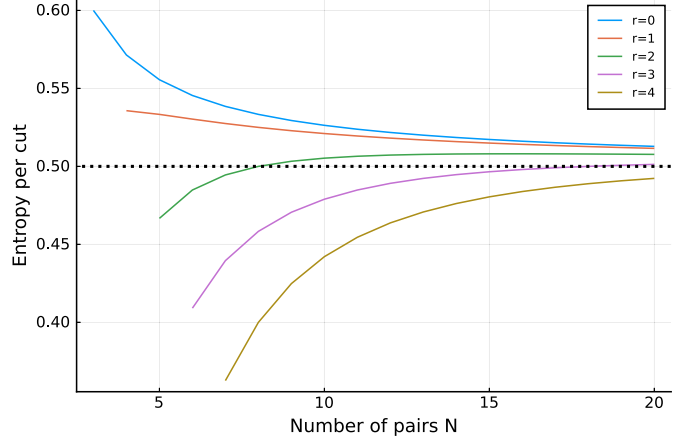


FIG. 7. Entropy value of a single cut for different magnetization sectors.

number of cuts made—which equal the number of spins—and multiplied by the average entropy contributed by cutting a pair, computed here.

APPENDIX C: DRAWING BLOCKADED POSITIONS

In the following, we restrict ourselves to N spins in $d = 1$ dimension and measure every distance in units of the blockade radius r_b . We define the density of spins $0 \leq \rho = \frac{1}{2W} \leq 1$, the corresponding volume of the space $L = \frac{N}{\rho}$, and set out to construct a scheme to efficiently generate a set of independently drawn positions $\{x_i\}$, that respect the blockade condition

$$|x_i - x_j| \geq r_b \quad \forall i \neq j. \quad (C1)$$

A priori, all positions are drawn i.i.d. from a uniform distribution over the full space $\mathcal{U}[0, L]$ and the naive way would be to just draw N positions and reject the sample if the blockade condition [Eq. (C1)] is violated. This is essentially equivalent to a random sequential adsorption process where the expected density in $d = 1$ is given by Renyi's parking constant $m \approx 0.748$ [57]. It directly follows that the rejection rate will become essentially 1 for any $\rho > m$ and we certainly will not get close to the fully ordered regime.

To circumvent this problem, we parameterize the positions like

$$x_i = is + \sigma_i, \quad (C2)$$

where $s = \frac{1}{\rho} = 2W$ is the mean interspin distance and $\sigma_i \sim \mathcal{U}[-\sigma, \sigma]$ are i.i.d. random variables. For $\sigma = \frac{L}{2}$, this ansatz is certainly equivalent to the naive scheme.

Note that, in the highly ordered case $\rho = 1 - \epsilon$, where ϵ is small, each realization of the experiment looks essentially like a regularly spaced chain with $s = \frac{1}{1-\epsilon} \approx r_b(1 + \epsilon)$ where each site has small fluctuations around the mean. This means, in this limit, we get away with choosing $\sigma \approx \epsilon$.

For our simulations, we used the just-described method in the region $W < 1.0$ and chose $\sigma = 1.5(\frac{1}{\rho} - 1)$. For $W \geq 1.0$,

we used the naive sampling strategy. One can see a slight jump in all plots at $W = 1.0$ where the sampling method changes.

-
- [1] M. Srednicki, *Phys. Rev. E* **50**, 888 (1994).
- [2] J. M. Deutsch, *Rep. Prog. Phys.* **81**, 082001 (2018).
- [3] C. Gogolin and J. Eisert, *Rep. Prog. Phys.* **79**, 056001 (2016).
- [4] L. D'Alessio, Y. Kafri, A. Polkovnikov, and M. Rigol, *Adv. Phys.* **65**, 239 (2016).
- [5] R. Nandkishore and D. A. Huse, *Annu. Rev. Condens. Matter Phys.* **6**, 15 (2015).
- [6] D. A. Abanin and Z. Papić, *Ann. Phys.* **529**, 1700169 (2017).
- [7] R. M. Nandkishore and S. L. Sondhi, *Phys. Rev. X* **7**, 041021 (2017).
- [8] D. A. Abanin, E. Altman, I. Bloch, and M. Serbyn, *Rev. Mod. Phys.* **91**, 021001 (2019).
- [9] M. Žnidarič, T. Prosen, and P. Prelovsek, *Phys. Rev. B* **77**, 064426 (2008).
- [10] D. J. Luitz, N. Laflorencie, and F. Alet, *Phys. Rev. B* **91**, 081103(R) (2015).
- [11] P. Sierant, M. Lewenstein, and J. Zakrzewski, *Phys. Rev. Lett.* **125**, 156601 (2020).
- [12] R. Vasseur, A. J. Friedman, S. A. Parameswaran, and A. C. Potter, *Phys. Rev. B* **93**, 134207 (2016).
- [13] I. V. Protopopov, R. K. Panda, T. Parolini, A. Scardicchio, E. Demler, and D. A. Abanin, *Phys. Rev. X* **10**, 011025 (2020).
- [14] T. Chanda, P. Sierant, and J. Zakrzewski, *Phys. Rev. Res.* **2**, 032045(R) (2020).
- [15] J. A. Kjäll, J. H. Bardarson, and F. Pollmann, *Phys. Rev. Lett.* **113**, 107204 (2014).
- [16] M. S. Bahovadinov, D. V. Kurlov, S. I. Matveenko, B. L. Altshuler, and G. V. Shlyapnikov, *Phys. Rev. B* **106**, 075107 (2022).
- [17] A. L. Burin, *Phys. Rev. B* **91**, 094202 (2015).
- [18] S. Schiffer, J. Wang, X.-J. Liu, and H. Hu, *Phys. Rev. A* **100**, 063619 (2019).
- [19] S. Roy and D. E. Logan, *SciPost Phys.* **7**, 042 (2019).
- [20] A. Safavi-Naini, M. L. Wall, O. L. Acevedo, A. M. Rey, and R. M. Nandkishore, *Phys. Rev. A* **99**, 033610 (2019).
- [21] Y. Mohdeb, J. Vahedi, and S. Kettemann, *Phys. Rev. B* **106**, 104201 (2022).
- [22] D. Pekker, G. Refael, E. Altman, E. Demler, and V. Oganesyan, *Phys. Rev. X* **4**, 011052 (2014).
- [23] A. C. Potter, R. Vasseur, and S. A. Parameswaran, *Phys. Rev. X* **5**, 031033 (2015).
- [24] R. Vosk, D. A. Huse, and E. Altman, *Phys. Rev. X* **5**, 031032 (2015).
- [25] C. Monthus, *J. Phys. A: Math. Theor.* **51**, 275302 (2018).
- [26] W. De Roeck and F. Huveneers, *Phys. Rev. B* **95**, 155129 (2017).
- [27] D. J. Luitz, F. Huveneers, and W. De Roeck, *Phys. Rev. Lett.* **119**, 150602 (2017).
- [28] A. Morningstar, L. Colmenarez, V. Khemani, D. J. Luitz, and D. A. Huse, *Phys. Rev. B* **105**, 174205 (2022).
- [29] D. Sels and A. Polkovnikov, *Phys. Rev. E* **104**, 054105 (2021).
- [30] D. Sels and A. Polkovnikov, *arXiv:2105.09348*.
- [31] D. Sels, *Phys. Rev. B* **106**, L020202 (2022).
- [32] T. Thiery, F. Huveneers, M. Müller, and W. De Roeck, *Phys. Rev. Lett.* **121**, 140601 (2018).
- [33] P. Ponte, C. R. Laumann, D. A. Huse, and A. Chandran, *Philos. Trans. R. Soc. London A* **375**, 20160428 (2017).
- [34] M. Pandey, P. W. Claeys, D. K. Campbell, A. Polkovnikov, and D. Sels, *Phys. Rev. X* **10**, 041017 (2020).
- [35] S. S. Kondov, W. R. McGehee, W. Xu, and B. DeMarco, *Phys. Rev. Lett.* **114**, 083002 (2015).
- [36] M. Schreiber, S. S. Hodgman, P. Bordia, H. P. Lüschen, M. H. Fischer, R. Vosk, E. Altman, U. Schneider, and I. Bloch, *Science* **349**, 842 (2015).
- [37] P. Bordia, H. P. Lüschen, S. S. Hodgman, M. Schreiber, I. Bloch, and U. Schneider, *Phys. Rev. Lett.* **116**, 140401 (2016).
- [38] A. Lukin, M. Rispoli, R. Schittko, M. E. Tai, A. M. Kaufman, S. Choi, V. Khemani, J. Léonard, and M. Greiner, *Science* **364**, 256 (2019).
- [39] J. Smith, A. Lee, P. Richerme, B. Neyenhuis, P. W. Hess, P. Hauke, M. Heyl, D. A. Huse, and C. Monroe, *Nat. Phys.* **12**, 907 (2016).
- [40] G. Kucsko, S. Choi, J. Choi, P. C. Maurer, H. Zhou, R. Landig, H. Sumiya, S. Onoda, J. Isoya, F. Jelezko, E. Demler, N. Y. Yao, and M. D. Lukin, *Phys. Rev. Lett.* **121**, 023601 (2018).
- [41] K. X. Wei, C. Ramanathan, and P. Cappellaro, *Phys. Rev. Lett.* **120**, 070501 (2018).
- [42] A. Signoles, T. Franz, R. F. Alves, M. Gärtner, S. Whitlock, G. Zürn, and M. Weidemüller, *Phys. Rev. X* **11**, 011011 (2021).
- [43] A. P. Orioli, A. Signoles, H. Wildhagen, G. Günter, J. Berges, S. Whitlock, and M. Weidemüller, *Phys. Rev. Lett.* **120**, 063601 (2018).
- [44] S. Geier, N. Thaicharoen, C. Hainaut, T. Franz, A. Salzinger, A. Tebben, D. Grimshndl, G. Zürn, and M. Weidemüller, *Science* **374**, 1149 (2021).
- [45] T. Franz, S. Geier, C. Hainaut, A. Signoles, N. Thaicharoen, A. Tebben, A. Salzinger, A. Braemer, M. Gärtner, G. Zürn, and M. Weidemüller, *arXiv:2207.14216*.
- [46] M. D. Lukin, M. Fleischhauer, R. Cote, L. M. Duan, D. Jaksch, J. I. Cirac, and P. Zoller, *Phys. Rev. Lett.* **87**, 037901 (2001).
- [47] D. A. Huse, R. Nandkishore, and V. Oganesyan, *Phys. Rev. B* **90**, 174202 (2014).
- [48] M. Serbyn, Z. Papić, and D. A. Abanin, *Phys. Rev. Lett.* **111**, 127201 (2013).
- [49] Only the closest copy of each spin is considered for the interaction.
- [50] <https://github.com/abraemmer/Pair-localization-paper>.
- [51] V. Oganesyan and D. A. Huse, *Phys. Rev. B* **75**, 155111 (2007).
- [52] Y. Y. Atas, E. Bogomolny, O. Giraud, and G. Roux, *Phys. Rev. Lett.* **110**, 084101 (2013).
- [53] M. Serbyn, Z. Papić, and D. A. Abanin, *Phys. Rev. X* **5**, 041047 (2015).
- [54] J. Eisert, M. Cramer, and M. B. Plenio, *Rev. Mod. Phys.* **82**, 277 (2010).
- [55] V. Khemani, S. P. Lim, D. N. Sheng, and D. A. Huse, *Phys. Rev. X* **7**, 021013 (2017).

- [56] D. Abanin, J. Bardarson, G. De Tomasi, S. Gopalakrishnan, V. Khemani, S. Parameswaran, F. Pollmann, A. Potter, M. Serbyn, and R. Vasseur, [Ann. Phys.](#) **427**, 168415 (2021).
- [57] A. Rényi, [Publ. Math. Inst. Hung. Acad. Sci.](#) **3**, 109 (1958).
- [58] M. Serbyn, Z. Papić, and D. A. Abanin, [Phys. Rev. B](#) **96**, 104201 (2017).
- [59] N. Macé, F. Alet, and N. Laflorencie, [Phys. Rev. Lett.](#) **123**, 180601 (2019).
- [60] D. J. Luitz, I. Khaymovich, and Y. Bar Lev, [SciPost Phys. Core](#) **2**, 006 (2020).
- [61] N. Y. Yao, C. R. Laumann, S. Gopalakrishnan, M. Knap, M. Müller, E. A. Demler, and M. D. Lukin, [Phys. Rev. Lett.](#) **113**, 243002 (2014).
- [62] J. Bezanson, A. Edelman, S. Karpinski, and V. B. Shah, [SIAM Rev.](#) **59**, 65 (2017).
- [63] S. Bravyi, D. P. DiVincenzo, and D. Loss, [Ann. Phys.](#) **326**, 2793 (2011).
- [64] D. S. Fisher, [Phys. Rev. B](#) **50**, 3799 (1994).
- [65] R. Vasseur, A. C. Potter, and S. A. Parameswaran, [Phys. Rev. Lett.](#) **114**, 217201 (2015).

5

EFFICIENT TIME EVOLUTION OF PAIR LOCALIZED SYSTEMS

can we exploit the knowledge about the conserved quantities to make numerics more efficient?

Cluster truncated Wigner approximation for bond-disordered Heisenberg spin models

Adrian Braemer,^{1,*} Javad Vahedi,^{2,†} and Martin Gärtnner^{2,‡}

¹*Physikalisches Institut, Universität Heidelberg, Im Neuenheimer Feld 226, 69120 Heidelberg, Germany*

²*Institute of Condensed Matter Theory and Optics,*

Friedrich-Schiller-University Jena, Max-Wien-Platz 1, 07743 Jena, Germany

(Dated: July 3, 2024)

We present a comprehensive numerical investigation of the cluster Truncated Wigner Approximation (cTWA) applied to quench dynamics in bond-disordered Heisenberg spin chains with power-law interactions. We find that cTWA yields highly accurate results over a wide parameter range. However, its accuracy hinges on a suitable choice of clusters. By using a clustering strategy inspired by the strong disorder renormalisation group (SDRG)/real-space renormalization group (RSRG), clusters of two spins are sufficient to obtain essentially exact results in the regime of strong disorder. Surprisingly, even for rather weak disorder, e.g. in the presence of very long-range interactions, this choice of clustering outperforms a naive choice of clusters of consecutive spins. Additionally, we develop a discrete sampling scheme for the initial Wigner function, as an alternative to the originally introduced scheme based on Gaussian approximations. This sampling scheme puts cTWA on the same conceptional footing as regular dTWA for single spins and yields some reduction in the Monte Carlo shot noise compared to the Gaussian scheme.

I. INTRODUCTION

Long-range interactions arise in several physical scenarios within disordered quantum many-body systems. For example, in doped semiconductors containing randomly positioned magnetic impurities, interactions occur via exchange couplings that depend on their spatial separation [1–3]. These interactions exhibit different behaviors depending on the state of the system. In insulating phases, the interaction strength decreases exponentially, as denoted by $J(r) \propto \exp(-r/\xi)$, while in metallic phases the interactions operate through the RKKY mechanism, following a power-law decay described by $J(r) \propto r^{-d}$, where d represents the dimension of the host system. Interestingly, sufficiently random, power-law interacting systems can even feature ultra-slow relaxation known from classical spin glasses as observed in local two-level systems formed by tunneling ions interacting through dipole-dipole and elastic forces [4, 5].

Moreover, recent experimental progress has enabled the manipulation and investigation of cold atoms or molecules featuring strong dipole-dipole interactions in diverse setups, including optical lattices [6–8], Rydberg gases [9–11], and trapped ions [12–16]. This has, in turn, spurred theoretical interest in studying quantum many-body dynamics in systems characterized by varying interaction ranges.

However, the potential of these studies is often limited by the lack of suitable computational tools. Considering that the Hilbert space of the system grows exponentially with the system size, the exact solution of quantum dynamics is limited to rather small systems. Even

employing sophisticated tools, e.g. based on Krylov subspaces [17–21], typically allows simulating systems of a only few tens of spins. Leaving the realm of exact methods, one usually tries to approximate the wave functions with a variational ansatz such as matrix product states (MPS) [22] and solves the dynamics within this variational manifold. While these MPS based methods, such as time-dependent density matrix renormalization group, have been used very successfully to simulate large, one-dimensional many-body systems with nearest neighbor interactions [23, 24], they struggle for higher dimensional or long-range interacting systems due to the rapid generation of entanglement [25, 26].

In the search for effective approaches to deal with many-body systems and the entanglement problem, phase-space methods have emerged as promising candidates. Among them, the truncated Wigner approximation (TWA) [27, 28], based on the Wigner-Weyl correspondence, stands out as a practical and widely adaptable strategy for exploring the dynamics of quantum many-body systems, even in higher-dimensional settings with long-range interactions [29–32]. At its heart, TWA approximates the dynamics of the Wigner function, i.e. the phase space analogue of the wave function, by particles following the classical mean-field equations of motions. The initial conditions of these particles are sampled from a Gaussian approximation of the initial Wigner function. While a priori TWA is exact only for short times, numerical experiments have shown it to yield accurate results at intermediate or even late times in some cases [33].

Although TWA was originally developed in the context of bosonic systems where a clear classical limit exists, it can also be applied to spin systems. Remarkably, for finite-dimensional quantum systems there exists a discrete formulation of the quantum phase-space [34]. For spin systems prepared in a product state, discrete TWA (dTWA) exploits this to dramatically improve ac-

* adrian.braemer@physi.uni-heidelberg.de

† javad.vahedi@uni-jena.de

‡ martin.gaerttner@uni-jena.de

curacy [35] and to capture quantum revivals [16, 36–45].

Another extension aims at incorporating more quantum interactions into the equations of motion, which in traditional TWA are essentially mean-field equations for single particles [46]. This so-called cluster TWA (cTWA) does so by grouping spins together into clusters and then assigning classical variables to all degrees of freedom within these clusters [47]. Thus all quantum interaction within a cluster is treated exactly and only interactions between clusters are approximated semi-classically. In the limit of clusters consisting of single spins, cTWA is identical to (d)TWA while in the opposing limit, where the whole system constitutes a single cluster the exact quantum evolution is recovered. Thus one has a tuning parameter to assess the convergence of the simulation which the usual (d)TWA lacks. While in principle cTWA is compatible with the discrete phase space formulation, literature on their combination is quite sparse. A conceptual precursor, dubbed GDTWA, exists in [48] where the discrete sampling was extended to larger $SU(N)$ spins. In a recent preprint a variant of discrete sampling is applied to a Bose-Hubbard model [49].

In this paper, we present a generalization of both cTWA and dTWA combining the discrete sampling scheme of the latter with the capability of treating clusters of spins of the former, which we term dcTWA. We then systematically evaluate the performance of these methods in the context of quench dynamics for bond disordered XX and XXZ long-range interacting spin 1/2 models. More precisely, we study the dynamics of an initial Néel state by means of the decay of the staggered magnetization and the buildup of Rényi entropy in a two-spin subsystem for different interaction ranges and disorder strengths and compare the results from the semi-classical methods to exact diagonalization. While in the weakly disordered regime a bigger cluster size is beneficial generally, we find that in the strongly disordered regime the physics is well captured by clusters of size 2 if they are chosen following a pairing rule known from the real space renormalization group (RSRG) approach to bond-disordered systems. Our analysis of the statistical uncertainties reveals that although the averaged results from cTWA and dcTWA are similar, dcTWA shows less sampling noise and thus converges faster.

II. MODEL AND METHODS

A. Model

We study the behavior of a disordered spin chain with long-range interactions, described by the Hamiltonian

$$H = \sum_{i < j} J_{ij} (\hat{s}_i^x \hat{s}_j^x + \hat{s}_i^y \hat{s}_j^y + \Delta \hat{s}_i^z \hat{s}_j^z) \quad (1)$$

where N spins ($\hat{s}_i = \frac{1}{2}\hat{\sigma}_i$) are randomly positioned at locations r_i along a lattice of length L with lattice spac-

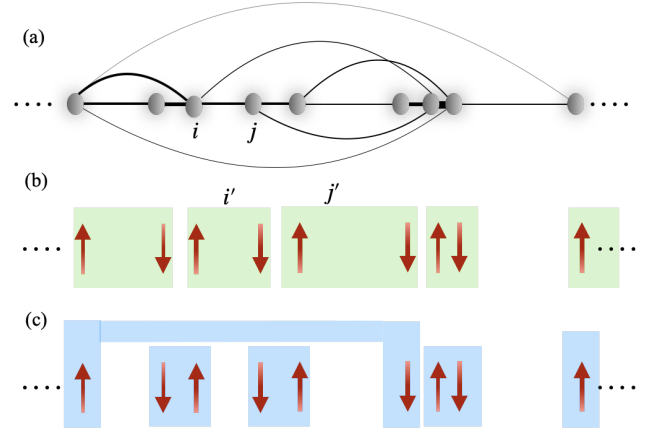


FIG. 1. (a) This diagram shows a long-range bond disorder spin chain where spins are randomly positioned along a lattice. The couplings are represented by solid lines, J_{ij} , while stronger bonds are indicated by thicker lines. (b) The initial state is the Néel state, represented as $|\Psi_0\rangle = |\uparrow\downarrow\cdots\uparrow\downarrow\rangle$, where each arrow represents the spin direction. The green shaded box illustrates a naive clustering of spins into clusters of size-2. (c) Clustering inspired by the real space renormalization group, as explained in the text.

ing a , resulting in a density $f = N/L$. The interactions J_{ij} between pairs of sites i and j are long-range, characterised by a power-law decay with parameter α : $J_{ij} = J_0|(r_i - r_j)/a|^{-\alpha}$. Throughout our study we set $J_0 = 1$ and $a = 1$, and employ open boundary conditions.

The disorder in this model arises from the random arrangement of spins along the chain, leading to different spin-spin couplings. The ground-state entanglement properties of this system (with $\Delta = 0$) have been previously studied in Ref. [50], where it was found that the entanglement entropy (EE) exhibits a logarithmic enhancement at zero temperature, independent of the parameter α . Moreover, it was found that for $\alpha > \alpha^*$ the EE of the excited eigenstates reflects the logarithmic divergence observed in the ground state. Conversely, for $\alpha < \alpha^*$, the EE exhibits an algebraic growth with respect to the subsystem size l , characterised by $s_l \sim l^\beta$, where $0 < \beta < 1$ [51, 52].

We explore the system dynamics by initializing it in a Néel state and subsequently computing dynamic observables. These observables encompass the staggered magnetization $M^{\text{st}}(t) = \sum_i (-1)^i \langle \hat{\sigma}_i^z(t) \rangle / N$ and the Rényi-2 entropy $S_2(t)$ evaluated over a two-spin subsystem. The Rényi-2 entropy belongs to a continuum of entropy measures defined as $S_\gamma(\hat{\rho}_A(t)) = \frac{1}{1-\gamma} \log_2 (\text{tr}[\hat{\rho}_A(t)^\gamma])$, where $\gamma \geq 1$. In this context, $\hat{\rho}_A(t) \equiv \text{Tr}_B \hat{\rho}(t)$ signifies the reduced density matrix associated with a subsystem A , and $\hat{\rho}(t)$ represents the density matrix of the entire system. Expanding the two-site reduced density matrix $\hat{\rho}_{ij} = \frac{1}{4} \sum_{\alpha\beta} \langle \hat{\sigma}_i^\alpha \hat{\sigma}_j^\beta \rangle \hat{\sigma}_i^\alpha \hat{\sigma}_j^\beta$ in a basis of Pauli strings gives a clear recipe for extracting the Rényi-2 entropy from the

expectation values of observables:

$$S_2(\hat{\rho}_{ij}(t)) = -\log_2 \left(\text{Tr} [\hat{\rho}_{ij}(t)]^2 \right) \quad (2)$$

$$= 2 - \log_2 \left(\sum_{\alpha\beta} \langle \hat{\sigma}_i^\alpha \hat{\sigma}_j^\beta \rangle^2 \right) \quad (3)$$

where we used the trace orthogonality of the Pauli strings. This expression has a clear physical meaning: The more correlations the subsystem retains after tracing out the environment, the weaker the entanglement is.

B. Cluster Truncated Wigner Approximation (cTWA)

Phase-space methods are powerful tools for simulating quantum system dynamics close to the classical limit. These methods have applications across various scientific domains, including quantum chemistry, optics, and condensed matter physics [28, 34]. Among them, the TWA maps quantum degrees of freedom onto classical phase-space variables following classical equations of motion as in a mean-field treatment. Quantum fluctuations are taken into account by Monte Carlo sampling of initial conditions from the Wigner function, which guarantees accuracy on short time scales. However, for quantum systems close to the classical limit, e.g. highly occupied bosonic modes or collective spin models, TWA has been found to yield accurate results even at late times [28].

When applying TWA to spin systems, usually one considers 3 degrees of freedom per spin: Its X , Y and Z magnetization [35]. Mapping these to classical variables treats all quantum interactions between spins on a mean-field level, which is justified if the interactions are either weak or very long-range and thus average out [33]. One avenue of incorporating more quantum effects into the dynamics, known as cluster TWA (cTWA), uses the degrees of freedom of clusters of spins instead of just the single spin ones [47]. In effect, this means all quantum dynamics within a cluster is computed exactly and only the interaction between clusters is approximated on a mean-field level. In the limit of a single cluster encompassing the whole system, cTWA is equivalent to an exact solution. Conversely, in the limit of clusters of single spins, cTWA reduces to regular TWA. Thus cTWA offers a tuning parameter to steadily tune between TWA and an exact solution by means of increasing the cluster size. In order to be self-contained, we provide an overview of this method. For a more detailed introduction, we refer the reader to the paper by Wurtz et al. [47].

To illustrate the cTWA method, consider a system of interacting spins-1/2 described by the Hamiltonian:

$$H = \sum_{ij} J_{ab}^{ij} \hat{\sigma}_a^i \hat{\sigma}_b^j + \sum_j B_a^j \hat{\sigma}_a^j \quad (4)$$

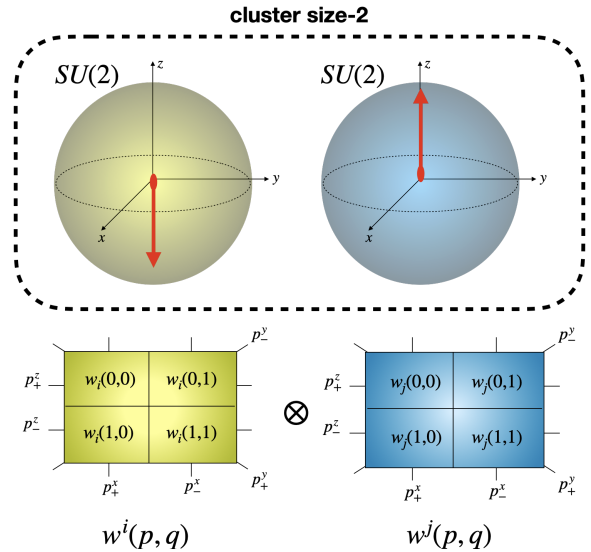


FIG. 2. A schematic of the discrete cluster truncated Wigner approximation. Considering a cluster of two spins, the individual Hilbert spaces (depicted as Bloch spheres) combine to the Hilbert space of the cluster. Shown below is a representation of the single spin discrete Wigner functions in the spirit of [35]. The probabilities of a spin pointing along the $\pm x$, $\pm y$ and $\pm z$ directions are computed by summing over the vertical, diagonal and horizontal lines, respectively. For product states within a cluster, one can simply take the tensor product of single spin discrete Wigner functions to obtain Wigner functions for the cluster. In the case of clusters of size 2, the resulting Wigner function is four-dimensional and contains 16 phase-points.

Here, $a, b \in x, y, z$ are the indices of Pauli matrices, and i, j denote distinct spins on the lattice. The couplings J_{ab}^{ij} and fields B_a^j can be either short-range or long-range.

The following steps outline the implementation of the operator cTWA:

- Divide the system into clusters indexed by $[i']$, as shown in Fig. 1(b). Define a complete operator basis $\{\hat{X}_p^{[i']}\}, p = 0, \dots, D^2 - 1$ for the Hilbert space of each cluster, where $D = 2^n$ is the dimension of the Hilbert space and n the number of spins making up the cluster. Ensure that the basis operators are trace-orthogonal and satisfy $\text{Tr}[\hat{X}_p^{[i']} \hat{X}_q^{[j']}] = D \delta_{pq} \delta^{[i'][j']}$. Then any operator $O^{[i']}$ inside a cluster $[i']$ can be written as linear combination of the basis operators $\hat{O}^{[i']} = \sum_p o_p \hat{X}_p^{[i']}$.

- Define structure constants f_{pqr} as

$$[\hat{X}_p^{[i']}, \hat{X}_q^{[j']}] = i f_{pqr} \delta_{[i'][j']} \hat{X}_r^{[i']}, \quad (5)$$

which project commutators onto the basis spanned by $\{\hat{X}_p^{[i']}\}$.

- Express the Hamiltonian in terms of cluster operators $\hat{X}_\alpha^{[i']}$.

$$\hat{H} = \sum_{[i'][j']} \mathbf{J}_{pq}^{[i'][j']} \hat{X}_p^{[i']} \hat{X}_q^{[j']} + \sum_{[j']} \mathbf{B}_p^{[j']} \hat{X}_p^{[j']} \quad (6)$$

The interactions \mathbf{J} and fields \mathbf{B} generally differ from the original parameters J_{ab}^{ij} , B_a^j . For instance, local fields now encompass connections among spins residing within a particular cluster, given that an operator $\sigma_a^i \sigma_p^j$ becomes linear in $\hat{X}_p^{[j']}$ when both spins i and j are part of the same cluster $[j']$.

- Associate basis operators $\hat{X}_p^{[i']}$ with classical phase space variables $x_\alpha^{[i']}$ satisfying canonical Poisson bracket relation, $\{x_p^{[i']}, x_q^{[j']}\} = i f_{pqr} \delta_{[i'][j']} x_r^{[i']}$ defined by the structure constants,

$$\hat{X}_p^{[i']} \rightarrow x_p^{[i']} - \frac{i}{2} x_q^{[i']} f_{pqr} \frac{\partial}{\partial x_r^{[i']}} \quad (7)$$

- Represent the Hamiltonian and observables as functions of classical phase space variables.

$$\hat{O}^{[i']} = \sum_p o_p \hat{X}_p^{[i']} \rightarrow O_{\mathbf{W}}(\{x\}) = \sum_p o_p x_p^{[i']} \quad (8)$$

with $o_p = \frac{1}{D} \text{Tr}[\hat{O} \hat{X}_p^{[i']}]$, and

$$\hat{H} \rightarrow H_{\mathbf{W}} = \sum_{[i'][j']} \mathbf{J}_{pq}^{[i'][j']} x_p^{[i']} x_q^{[j']} + \sum_{[j']} \mathbf{B}_p^{[j']} x_p^{[j']} \quad (9)$$

where index \mathbf{W} indicates that this is the Weyl symbol corresponding to symmetric operator ordering.

- Find or approximate the Weyl-symbol of the initial state, i.e. its Wigner function. While it can assume negative values, we require that it is completely positive and thus can be thought of as a probability distribution. We present two possible definitions for the Wigner function below this implementation guide.
- Solve the classical equations of motion for the phase space variables,

$$\frac{dx_p^{[i']}(t)}{dt} = -\{x_p^{[i']}, H_{\mathbf{W}}\} = f_{pqr} \frac{\partial H_{\mathbf{W}}}{\partial x_q^{[i']}} x_r^{[i']} \quad (10)$$

- Find expectation values of observables by averaging the corresponding classical functions over phase space points sampled from the Wigner function, $\langle \hat{O}(t) \rangle = \lim_{M \rightarrow \infty} \frac{1}{M} \sum_m^M O_{\mathbf{W}}(\{x(t)\}_m)$, where M denotes the number of samples.

1. Gaussian Wigner function

Wurtz et al. [47] defined an approximate Gaussian Wigner function $\mathcal{W}(\{x\})$ describing the initial conditions for the system with the only requirement that the initial state factorizes between clusters such that $\mathcal{W}(\{x\}) = \prod_{[i']} \mathcal{W}^{[i']}(\{x_\alpha^{[i']}\})$, where

$$\mathcal{W}^{[i']}(x^{[i']}) = \frac{1}{Z} \exp \left[(x_p - \rho_p^{[i']}) \Sigma_{pq}^{[i']} (x_p - \rho_q^{[i']}) \right] \quad (11)$$

is simply a Gaussian. To determine coefficients $\rho_p^{[i']}$ and $\Sigma_{pq}^{[i']}$ from the initial density matrix on cluster $[i']$, we demand (cluster index $[i']$ suppressed)

$$\text{Tr}[\hat{\rho} \hat{X}_q] = \int \prod_p dx_p x_q \mathcal{W}(\{x\}) \quad (12)$$

$$\text{Tr}[\hat{\rho} (\hat{X}_q \hat{X}_r + \hat{X}_r \hat{X}_q)] = 2 \int \prod_p dx_p x_q x_r \mathcal{W}(\{x\}) \quad (13)$$

such that the moments match to second order.

2. Discrete Wigner function

While the Gaussian approximation of the Wigner function described above is quite general, it neglects the moments beyond the second order. dTWA on the other side can capture all moments of the single-spin observables for initial states that factorize between individual spins [35]. In the following, we briefly recapitulate the derivation dTWA's sampling to introduce the notation and then generalize the method to clusters of spins.

The key idea behind the dTWA is to replace the Gaussian approximation of the Wigner function with a discrete Wigner function defined via a discrete set of phase-point operators $\hat{\mathbf{A}}^{\otimes n} = \bigotimes_i^N \hat{A}^{[i]}$ where $\hat{A}^{[i]}$ are discrete phase-point operators that span the $SU(2)$ phase-space of the i th spin. These are usually defined as $\hat{A}_{p,q}^{[i]} = (\mathbb{1} + \mathbf{r}(p,q) \cdot \hat{\sigma})/2$, $\hat{\sigma} = (\hat{\sigma}_x, \hat{\sigma}_y, \hat{\sigma}_z)$ are the Pauli matrices and $\mathbf{r}(p,q)$ denotes suitable combinations thereof (cf. [34, 35, 37]): $\mathbf{r}(0,0) = (1,1,1)$, $\mathbf{r}(0,1) = (-1,-1,1)$, $\mathbf{r}(1,0) = (1,-1,-1)$ and $\mathbf{r}(1,1) = (-1,1,-1)$. In case the wavefunction factorizes, the Wigner function of the system is then given simply by the product of single spin Wigner function given by $w^{[i]}(p,q) = \langle \hat{A}_{(p,q)} \rangle / 2$. Crucially, for all spin states pointing along one axis each value of $w^{[i]}(p,q)$ is positive and, since they sum to 1, one can interpret them as probability distribution to sample from. A schematic illustration is provided in Fig. 2.

Considering a system of n_c clusters of n spins each, we again seek to describe the state by a discrete Wigner function. The main difference to before is that each local Hilbert space is represented by a copy of $SU(D)$, where $D = 2^n$. In analogy to before, we introduce the phase-point operators $\hat{\mathbf{A}}^{\otimes n_c} = \bigotimes_{i'}^{n_c} \hat{A}_n^{[i']}$ with $\hat{A}_n^{[i']} = (\mathbb{1}_D +$

$\mathbf{r}_n^{[i']} \cdot \mathbf{X}_n)/D$, where $\mathbf{r}_n^{[i']} = (r_1^{[i']}, \dots, r_{D^2-1}^{[i']})_i$ represents a vector of $D^2 - 1 = 4^n - 1$ real-valued parameters and \mathbf{X}_n corresponds to a vector of the operators of the operator basis for a cluster of n spins as used in cTWA. Note, we can construct the operator basis \mathbf{X}_n for n spins iteratively from an operator basis \mathbf{X}_1 for a single spin by taking tensor products $\mathbf{X}_n = (\mathbf{X}_1 \otimes \mathbf{1}, \mathbf{1} \otimes \mathbf{X}_{n-1}, \mathbf{X}_1 \otimes \mathbf{X}_{n-1})$. One can construct \mathbf{r}_n analogously:

$$\mathbf{r}_n(\mathbf{p}, \mathbf{q}) = [\mathbf{r}_1(p_1, q_1), \mathbf{r}_{n-1}(\tilde{\mathbf{p}}, \tilde{\mathbf{q}}), \mathbf{r}_1(p_1, q_1) \otimes \mathbf{r}_{n-1}(\tilde{\mathbf{p}}, \tilde{\mathbf{q}})] \quad (14)$$

with $\mathbf{p}, \mathbf{q} \in \{0, 1\}^n$ and $\tilde{\mathbf{p}}$ ($\tilde{\mathbf{q}}$) denoting the vector derived from \mathbf{p} (\mathbf{q}) by dropping the first element. Suppressing the index n from now on, the Wigner function of a cluster is defined as before to be $w^{[i']}(p, q) = \langle \hat{A}_{(p,q)} \rangle / D$. If the quantum wavefunction factorizes between spins within a cluster, the Wigner function also factorizes and the result is essentially equivalent to the single spin case:

$$w^{[i']}(p, q) = \prod_i \left\langle \hat{A}_{(p_i, q_i)} \right\rangle / 2 = \prod_i w^{[i]}(p_i, q_i) \quad (15)$$

The key difference is in the phase-point vectors $\mathbf{r}_n(\mathbf{p}, \mathbf{q})$ connected to this Wigner function which now also encompass a much larger operator basis. In summary, if the initial wave function factorizes between spins, one can simply sample the initial values for the single spin operators and compute the initial values for operators acting on multiple spins by appropriate products. For a more detailed description of the sampling process, see appendix A.

As a concrete example, consider a cluster of 2 spins in a Néel state $|\uparrow\downarrow\rangle$. To generate a sample, one draws the 4 values for $\langle \hat{X}_1 \rangle$, $\langle \hat{Y}_1 \rangle$, $\langle \hat{X}_2 \rangle$, and $\langle \hat{Y}_2 \rangle$ randomly from $\{-1, 1\}$ and sets $\langle \hat{Z}_1 \rangle = -\langle \hat{Z}_2 \rangle = 1$. Then rest of the correlators are computed from the products of these, e.g. $\langle \hat{X}_1 \hat{Y}_2 \rangle = \langle \hat{X}_1 \rangle \langle \hat{Y}_2 \rangle$ and so on. This means that the initial spin vectors are randomly drawn from one of the 16 spin configurations. All other states on the Bloch sphere can be sampled using the same configurations, followed by an appropriate rotation.

C. Clustering strategies

The cTWA necessitates a choice of clustering of the spins. While in ordered systems, it makes sense to simply choose contiguous regions of desired size, in disordered systems it is not clear a priori that this is a reasonable choice. In this work, we evaluate two possible strategies for choosing the clustering:

- *Naive clustering method* (see Fig. 1-b): In this approach, clusters of spins are formed by starting from one end of the chain and grouping together every n consecutive spins. Thus, the resulting clusters are determined solely on the basis of this selection process, without taking into account any specific properties or interactions between the spins.

- *Renormalization Group clustering* [see Fig. 1(c)]: The RG clustering strategy takes inspiration from the real space renormalization group (RSRG), also known as strong disorder renormalization group (SDRG), approaches to bond-disordered models which are used to construct approximate eigenstates [53–55]. These methods identify the two spins sharing the strongest coupling in the system and treats their couplings to the environment in a perturbative manner. Since this procedure effectively decouples the pair and leaves the form of the remaining Hamiltonian invariant, one can readily repeat this procedure with the remaining spins until all spins are paired up. Instead of computing eigenstates, we simply use the resulting partition of spins into clusters of size two as input for the cTWA. In this way, the strong intra-pair interactions are treated fully quantum mechanically, while the effective interaction among pairs is treated semi-classically.

Based on the excellent results found by RSRG/SDRG, we expect the RG clustering to outperform the naive clustering method for strong disorder. However, the naive clustering scheme generalizes naturally to generate larger clusters, while it is unclear how to merge the clusters given by the RG scheme in a consistent manner.

III. RESULTS

In this section, we present the numerical results of our exploration of the quench dynamics of a disordered spin chain with long-range interactions. We compute the behavior of two dynamical observables initiated from an Néel state, namely the staggered magnetization and the Rényi entropy $S_2(t)$ evaluated over a two-spin subsystem, using the different methods detailed above and compare to results obtained with exact diagonalization (ED). Our primary focus lies on evaluating the performance of the cluster truncated Wigner approximation (cTWA) relative to standard dTWA. To this end, we consider combinations of the aforementioned clustering schemes, the naive clustering and the one based on the strong disorder renormalization group, and the two approximations of the initial state, the Gaussian cTWA (gcTWA) and discrete cTWA (dcTWA). Our analysis aims to shed light on how cTWA captures the intricate behavior of the system under bond disorder and long-range interactions, and to elucidate the extent to which this approach provides insights into the quantum dynamics of the system under consideration. All curves shown are obtained using 1000 disorder samples and 1000 Monte-Carlo trajectories unless specified otherwise. Disorder shots are identical across the methods. The code is freely available at [GitHub](#) [56]. Statistical errors due to finite sample sizes of disorder and Monte Carlo trajectories are below the width of the lines.

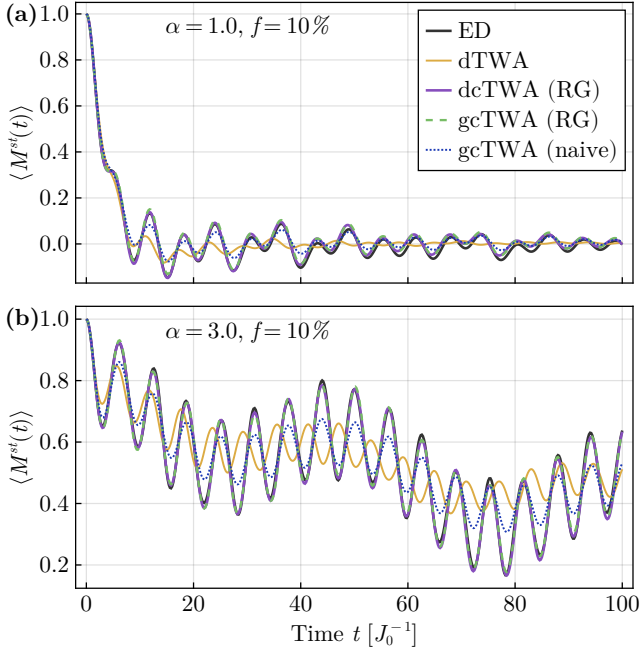


FIG. 3. The disorder-averaged staggered magnetisation $\langle M^{\text{st}}(t) \rangle$ is shown for XX chain of $N = 16$ spins with a fixed filling of $f = 10\%$. The panels show results for long-range interactions with $\alpha = 1.0$ in (a) and short-range interactions with $\alpha = 3.0$ in (b). The semi-classical cluster methods using the RG-inspired clustering (green, dashed and purple, solid) overlap the exact results (black, solid) almost completely. dTWA (yellow, solid) and gcTWA with naive clustering (blue, dotted) deviate already early on ($t \approx 10 J_0$).

A. Bond disordered XX chain

We begin our investigation by considering a bond-disordered XX chain ($\Delta = 0$). We explore various regimes by adjusting two key parameters: the power-decay exponent of the interaction, denoted as α , and the filling fraction of the lattice, denoted as f , which controls the strength of the disorder. Here a low filling fraction corresponds to strong disorder, while $f = 100\%$ represents a fully ordered system.

Fig. 3 shows the disorder-averaged time evolution of the staggered magnetisation $\langle M^{\text{st}}(t) \rangle$ with a fixed filling of $f = 10\%$, starting from the Néel state. The top panel corresponds to long-range interactions ($\alpha = 1$), while the bottom panel corresponds to short-range interactions ($\alpha = 3$). The staggered magnetisation starts at a value of one, which reflects the perfect order inherent in the initial Néel state. It then undergoes a decay, caused by the spins exchanging magnetization as system evolves. At late times, we observe equilibration to a value close zero. The general behavior is captured by all semi-classical methods.

Upon closer inspection, it becomes evident that the dTWA approach fails to accurately track the true dynamics and loses accuracy even at intermediate timescales

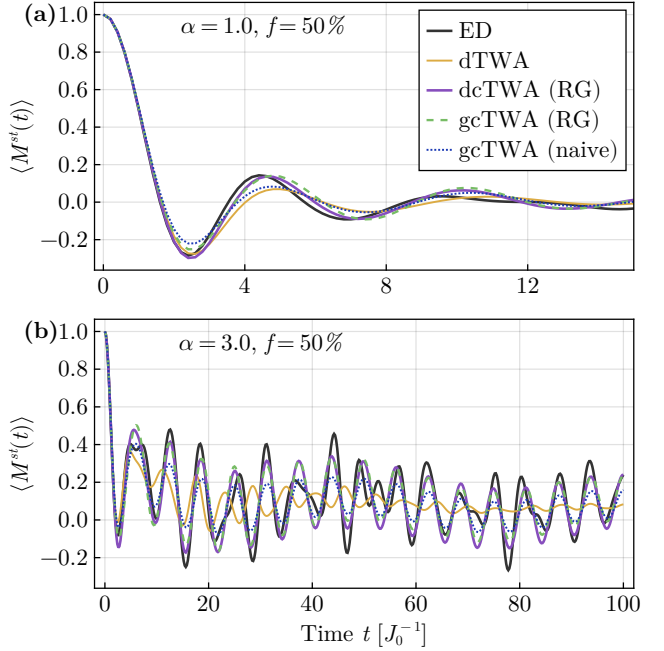


FIG. 4. Same as Fig. 3, but for filling fixed at $f = 50\%$ (weak disorder regime). Here, the methods using the RG-inspired clustering show some deviation from the exact results and for $\alpha = 1$ in panel (a) there are some differences between the Gaussian and discrete sampling schemes visible as well.

starting around $t J_0 \approx 10$. In both cases, it predicts the location of the first oscillation approximately correctly but underestimates the amplitude. Subsequently, it systematically underestimates the amplitude of the oscillations of the staggered magnetization. Interestingly, gcTWA with the naive clustering does not fare much better. While it is generally more accurate with respect to the oscillation frequency, it also underestimates the amplitude. In contrast, both cTWA variants using the RG clustering yield essentially exact results even at late times. This is a very strong indicator that the dynamics is strongly shaped by the presence of strongly interacting pairs of spins where interactions among pairs are weak [57]. With this pair model we can explain the observed curves qualitatively: It is known that dTWA is unable to correctly capture the dynamics of even a single pair and can just approximate the decay timescale (cf. App. B). If the two spins forming a strongly interacting pair are not part of the same cluster, then cTWA treats the interactions within the pair semi-classically similar to dTWA and thus faces the same problems. Consequently, using the naive clustering will result in a mixture of "correctly" and "incorrectly" chosen pairs and thus cTWA with this type of clustering provides only a slight improvement over dTWA. The RG clustering, in turn, ensures that all strongly interacting pairs are treated as clusters and thus the predictions match the exact dynamics much more closely. In turn, the high degree of agreement between cTWA with the RG clustering is also

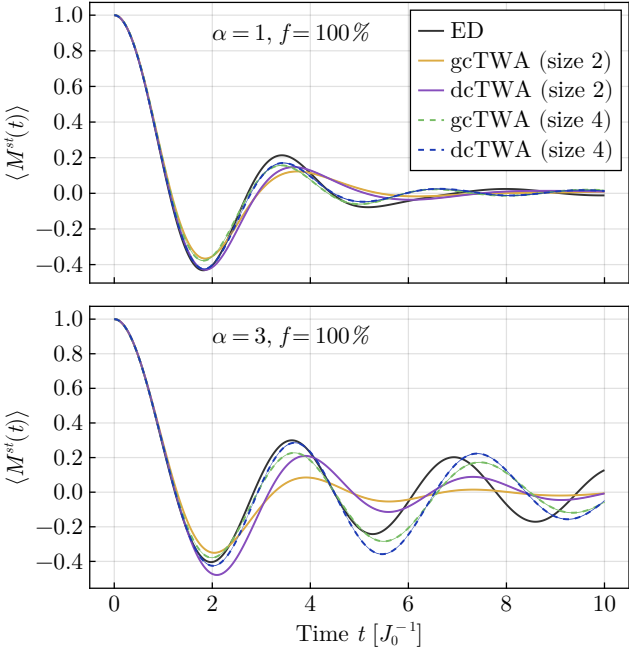


FIG. 5. Comparison of sampling schemes with different cluster sizes in a clean system (filling fraction $f = 100\%$). We compare TWA results for cluster sizes 2 (solid) and 4 (dashed) using the naive clustering and the different sampling schemes, Gaussian (lighter colors) and discrete (darker colors) to exact results (black, solid). Generally, cluster size 4 is more accurate than cluster size 2 and the discrete sampling scheme agrees with the exact results longer than the Gaussian sampling scheme. Other parameters are similar to Fig. 3.

testament to the quality of pair approximation.

To further explore the efficacy of cTWA in regimes of weak disorder, we increase the filling fraction to $f = 50\%$ and repeat the analysis (cf. Fig. 4). In this regime, we do not expect the pair approximation to be accurate anymore. Indeed, for the long-range case $\alpha = 1$ we find all semi-classical methods to overestimate the oscillation frequency similarly. Both RG clustering based methods predict the amplitudes almost exactly correct, while dTWA and cTWA with naive clustering again clearly underestimate it. In the more short-range case $\alpha = 3$, the picture is more complex. dTWA performs worst out of all the methods and does not resolve the oscillation well and cTWA with naive clustering again essentially underestimates the amplitude. Interestingly, in this case there is a clear difference on intermediate timescales $t \approx 8J_0$ between both cTWA methods with RG clustering but different choice of sampling. The discrete sampling captures the first oscillation slightly better both in position and in amplitude before at later times the prediction collapses onto the cTWA curve employing a Gaussian Wigner function. Generally, all cluster based methods still capture the dynamics qualitatively but not quite quantitatively over the whole time shown here.

For a better comparison of the sampling schemes, it

is instructive to examine a perfectly ordered regime by setting the filling factor to $f = 100\%$. In this setting, the RG and naive clustering schemes result in the same choice of clusters and we use this opportunity to check the convergence with increasing cluster size. Fig. 5 shows the staggered magnetisation results for systems with both long-range ($\alpha = 1.0$) and short-range ($\alpha = 3.0$) spin interactions and for cluster sizes 2 and 4. Similar to the weakly disordered case before, cluster size 2 is insufficient to capture the relaxation dynamics quantitatively. In the short-range case ($\alpha = 3$) gcTWA (cluster size 2) struggles to reproduce the oscillatory behavior, which is reflected better by dcTWA. This likely stems from the fact that this coherent dynamics comes about due to the discrete nature of the spin- $\frac{1}{2}$ s which is mimicked by the discrete sampling procedure [35]. Conversely, for the long-range system ($\alpha = 1$), this effect is weaker as spins hybridize more due to the stronger interactions. Interestingly, for this setting dcTWA predicts the value of the first minimum more accurately than gcTWA. Increasing the cluster size to 4 spins improves the accuracy of both methods in both cases drastically and we don't find significant differences between the sampling schemes in the long-range case. However, for the short range case, we find the discrete sampling scheme to approximate the true amplitude of the oscillation generally better than the Gaussian scheme.

To extend our investigation to more complicated, non-local observables, we study the Rényi entropy of two-spin subsystems and assess the efficacy of the semi-classical methods under scrutiny. More specifically, we consider the average Rényi entropy across all possible choices of two sites.

Starting with the strongly disordered setting at $f = 10\%$ in an analogy to above, Fig. 6 illustrates the dynamics of the average Rényi entropy with time in a strongly disordered setting. Since the initial state is a product state, entanglement starts at 0 for $t = 0$ and then starts to increase. We find, that generally the semi-classical methods are able to capture the dynamics across the different settings probed qualitatively, as shown in Fig. 6 and Fig. 7. Perhaps surprisingly at first, these methods systematically overestimate the amount of entanglement present. This conundrum can be resolved, if one considers that the Rényi entropy is computed by estimating the expectation values of all intra-pair correlators and less correlations means more entanglement of the pair with its environment (cf. Eq. 3). The semi-classical methods miss out on some of the quantum correlations, thus tend to underestimate the total amount of correlations and consequently predict too much entanglement. Again, the quality of the result depends significantly on the scheme. The deviations are most pronounced for dTWA and the cTWA with naively chosen clusters. Conversely, both dcTWA and gcTWA with the RG clustering scheme approximate the exact dynamics very closely and only overestimate the entanglement by a few percent at late times.

In summary, we find that cTWA may offer tremen-

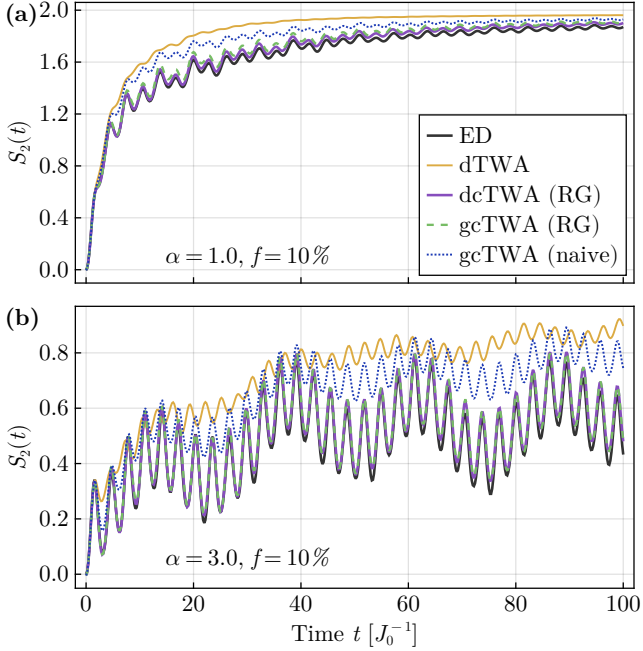


FIG. 6. The average Rényi entropy $\langle S_2(t) \rangle$ is calculated over all possible choices of two sites. This analysis is performed with the same parameter settings as in Fig. 3. The cTWA methods using the RG-inspired clustering (purple, solid and green, dashed) reproduce the exact entanglement dynamics (black, solid) almost exactly with only very slight deviations at late time. Whereas the gcTWA with naive clustering (blue, dotted) overestimates the entanglement and dTWA (yellow, solid) even more so.

dous improvements over the simpler dTWA. However, the improvement depends strongly on the choice of clusters. If the clustering does not respect the underlying physics, as is the case for the naive clustering strategy, cTWA showed only a very minor increase in accuracy. On the other hand, if the dominant physical processes are mostly contained within the chosen clusters, as is the case with the RG inspired clustering, cTWA can describe the dynamics of the system over all time intervals almost exactly. The results obtained with the Gaussian Wigner function were very similar compared to the discrete sampling with a slight advantage in favor of the discrete scheme for ordered, short-range systems.

B. Bond disordered XXZ chain

In this section, we investigate the role of the anisotropy parameter Δ in the dynamics of the system. In the pair picture, a strong anisotropy increases the energy gap between the sectors of different absolute z-magnetization. This does not alter the dynamics of a single pair initialized in a Neel state, because dynamics is fully contained within the sector of zero magnetization. As such, we expect the choice of clusters to have a large impact on the

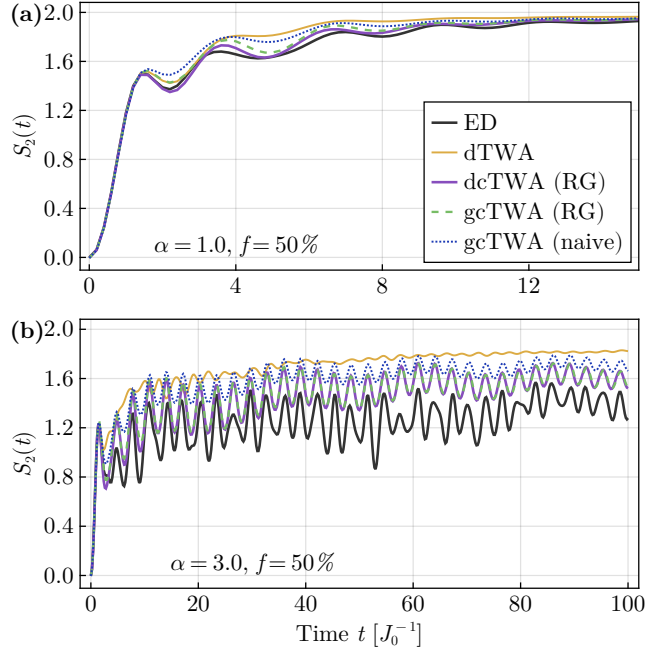


FIG. 7. Same as Fig. 6, but for density fixed at $f = 50\%$. In comparison to Fig. 6, the RG-based cTWA methods deviate from each other and also overestimate the true amount of entanglement present. In the long-range case (a) they don't capture the oscillation frequency correctly, however in the short-range case (b) they do but underestimate the amplitude.

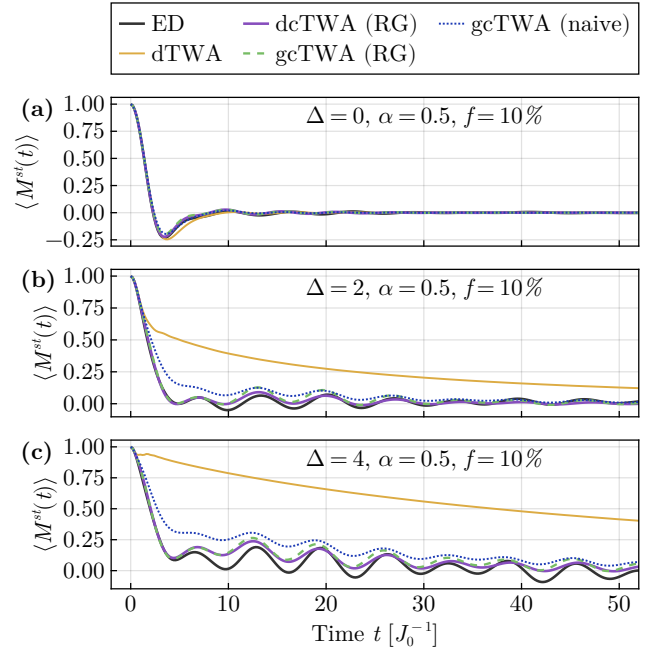
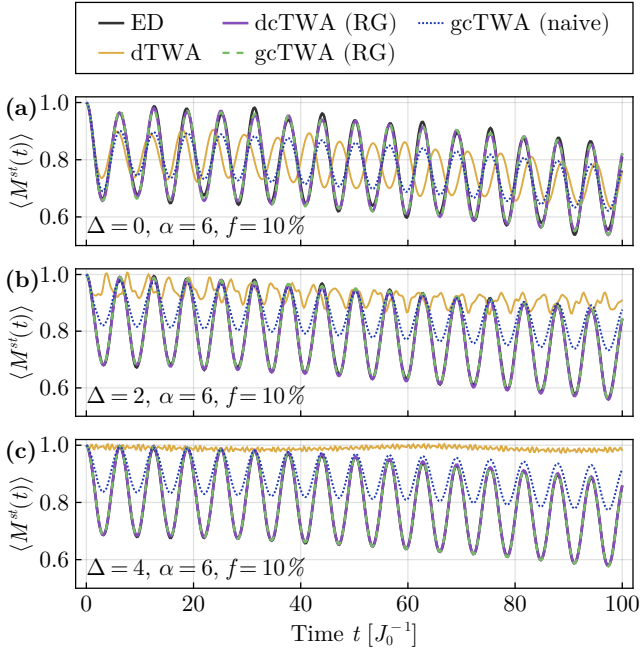
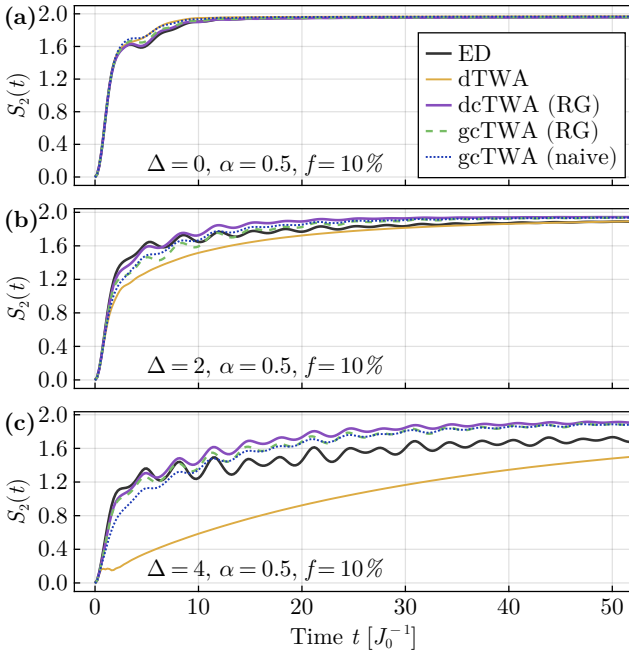
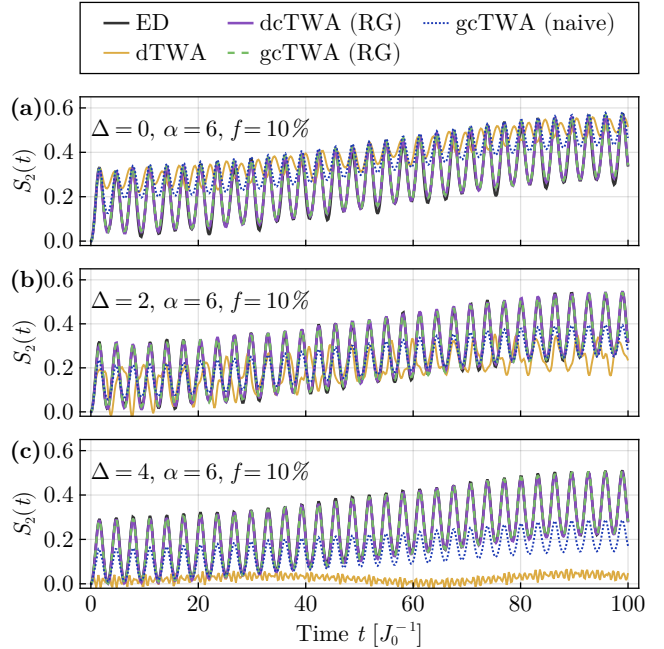


FIG. 8. The disorder-averaged staggered magnetisation $\langle M^{st}(t) \rangle$ is shown for XXZ chain of size $N = 16$ with $\alpha = 0.5$ at $f = 10\%$. Different panels are shown for different Δ . Results of cTWA, dTWA and ED are shown with solid-blue, dotted-green, and solid-blue, respectively.

FIG. 9. Same as Fig.8 but for $\alpha = 6.0$ FIG. 10. The average Rényi entropy $\langle S_2(t) \rangle$ is calculated over all possible pairs of two sites. This analysis is performed with the same parameter settings as in Fig. 8.

quality of the approximation whenever the dynamics is heavily dominated by pair dynamics. To expand the domain of our study, we employ $\alpha = 0.5$ to evaluate settings with even more long-range interactions, which in principle should play to TWA's strengths. In the short range case, we chose $\alpha = 6$, as motivated by the typical interac-

FIG. 11. Same as Fig.10 but for $\alpha = 6.0$

tion exponent of Van-der-Waals interactions in Rydberg atoms which are a possible platform to implement XXZ Heisenberg models (see e.g. [58]). We note however, that the qualitative differences to $\alpha = 3$ are minor.

Figures 8 and 9 show the dynamics of the staggered magnetisation under long-range ($\alpha = 0.5$) and short-range ($\alpha = 6$) interactions, respectively. Starting again from the Néel state, we examine the evolution of the staggered magnetization by varying Δ , assessing how these adjustments affect the dynamics and how well semi-classical methods approximate the true dynamics. At $\Delta = 0$, all semi-classical methods give results matching the exact solution over almost the entire time scale for the long-range system ($\alpha = 0.5$), while in the short range system ($\alpha = 6$) only the cTWA simulations using the RG-inspired clustering provide accurate results. dTWA performs worst by predicting oscillation with both wrong amplitude and frequency. gcTWA with naive clustering improves upon this due to the inclusion of more quantum correlations which results in a correct prediction of the frequency.

Increasing the Ising interaction [cf. Figures 8 and 9 (b) and (c)] does not alter the exact dynamics qualitatively, but dTWA increasingly deviates from the exact results vastly underestimating the rate of the initial decay. For the short range system and $\Delta = 4$ the decay is almost completely suppressed. By contrast, gcTWA with naive clustering yields significantly better results than dTWA. For both systems, the gcTWA prediction qualitatively matches the exact data but is offset by an increasing amount with increasing Δ . Interestingly, both cTWA variants using the RG-inspired clustering, match the ref-

erence rather closely over the entire time domain except for intermediate times for $\Delta = 4$ in the long-range system $\alpha = 0.5$, where the fluctuations are not reproduced exactly. Surprisingly, this hints at pairs still playing an important role for the dynamics in spite of the quite long-range interactions. For the short-range interactions with strong disorder, the precise match is no surprise as the dynamics is governed by pairs of spins on adjacent lattice sites in this regime.

Again, we employ the semi-classical methods to also extract the average pair Rényi entropy and compare to exact results. Starting with the long-range scenario, $\alpha = 0.5$, we find for $\Delta = 0$, all semi-classical approaches to converge to the true dynamics approximately (Fig. 10). Increasing Δ , we can see again how dTWA fails to capture the essential processes and predict much too slow dynamics (roughly one order of magnitude too slow). gcTWA with naive clustering fares rather well and only slightly underestimates the initial rise for $\Delta = 2$ very similar to gcTWA with RG-inspired clustering. Most interesting are the differences between gcTWA and dcTWA (both with RG clustering) since in this setting both methods seem to converge to slightly different results with dcTWA following the exact curve more closely at intermediate times (up to $t \approx 10J_0$). At late times all cTWA methods overestimate the amount of entanglement present. This trend continues for $\Delta = 4$ where the discrepancy is enhanced for all methods.

For the short-range interacting systems, we find that cTWA schemes based on the RG clustering to be in excellent agreement with the exact results, while the naive clustering gcTWA and dTWA fail to capture the dynamics. This stark contrast to the long-range interacting systems likely originates in the much broader distribution of couplings caused by the much shorter interaction range. Since the RG clustering scheme incorporates the strongest of the relevant couplings, the system can show deviations only at very late timescales.

In order to understand, why dTWA struggles to accurately capture the dynamics of even a single pair of spin interacting via an XXZ Hamiltonian $H = J(\sigma_x^1\sigma_x^2 + \sigma_y^1\sigma_y^2) + \Delta\sigma_z^1\sigma_z^2$ we need to consider its spectrum. Eigenstates of H are the maximally entangled Bell states $|\pm\rangle = (|\uparrow\downarrow\rangle \pm |\downarrow\uparrow\rangle)/\sqrt{2}$ at energies $E_{\pm} = \pm 2J - \Delta$ and the polarized states $|\uparrow\uparrow\rangle$ and $|\downarrow\downarrow\rangle$ with energy $E_p = \Delta$. Taking the Neel state $|\uparrow\downarrow\rangle = (|+\rangle + |-\rangle)/\sqrt{2}$ as initial state, the exact quantum dynamics only populates the two maximally entangled eigenstates. Since their energetic splitting depends on J only, the exact dynamics is independent of Δ and just encompasses the coherent flipping of both spins $|\uparrow\downarrow\rangle \leftrightarrow |\downarrow\uparrow\rangle$. dTWA essentially has access only to single body-terms and thus needs to approximate this process by two steps which will couple to the polarized states. This gives an intuitive understanding of the dependence on Δ for dTWA. The precise nature of this relation is quite intricate and not akin to, e.g., a two-photon transition. For further analysis of the 2 spin case with dTWA, we refer to Appendix B. At this point,

we want to remark that even cTWA of course captures the dynamics exactly if the two spins are part of the same cluster, but still the state is not represented exactly at all times. As we have shown in Appendix A, dcTWA can only represent states where the Wigner function is non-negative but one can ensure that all observables within a cluster have correct means and only higher moments deviate.

In summary, we find that even in very long-range systems and for strong Ising interactions the RG-inspired clustering yields quite accurate results at early and intermediate times. At late times, we see some deviations that increase with the strength of the Ising couplings which likely signals the breakdown of the pair approximation in this regime. For short-range interactions, the cTWA methods with RG clustering yield basically exact results in all cases studied here. Conversely, dTWA and gcTWA with the naive clustering strategy struggle due to the competition of the Ising and hopping interactions. We did not see a significant difference between discrete and Gaussian sampling in these settings.

C. Statistical Error Analysis

To highlight the merits of the discrete sampling scheme, we study the convergence of the staggered magnetization Monte-Carlo samples by extracting standard deviation of the staggered magnetization across 10.000 trajectories of a single disorder shot. While previous analyses did not show large differences in result between the sampling schemes, Fig. 12(a) reveals the higher accuracy of the discrete sampling schemes which leads to a reduced number of samples required to achieve a given level of precision. Averaged over the timescale shown, we report approximately 8% smaller standard deviation for dcTWA with cluster size 2 and 15% reduction for cluster size 4. This translates to approximately 16% respectively 28% fewer trajectories needed to achieve similar levels of accuracy.

We repeat this analysis for the Renyi entropy, where we estimate the standard deviation from 100 sets of 100 trajectories each [cf. Fig. 12(b)]. Again by averaging, we find a similar reduction of 14% and 29% reduction in standard deviation for cluster sizes 2 and 4 respectively.

IV. CONCLUSION

In this study, we conducted a comprehensive numerical investigation focusing on the Cluster Truncated Wigner Approximation (cTWA) for modelling quench dynamics in disordered spin chains with power-law interactions. Through comparisons with the Discrete Truncated Wigner Approximation (dTWA) and the Exact Diagonalisation (ED), we explored the performance of the cTWA on different time scales relevant to quench experiments and studied the influence of the choice of clusters on the

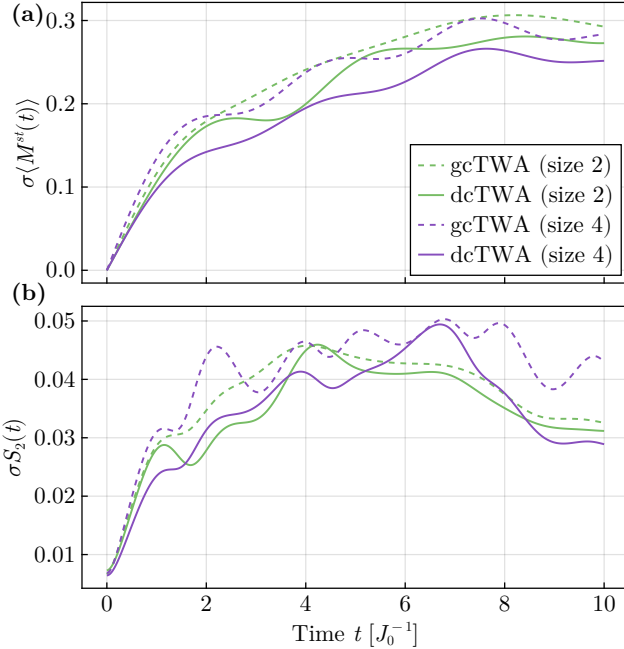


FIG. 12. Error analysis for a single shot with the parameters $\alpha = 1$, $f = 10\%$, $\Delta = 0$ and 10,000 trajectories. We compute the standard deviation of (a) the staggered magnetization and (b) average pair Renyi entropy estimated from batches of 100 trajectories. We use naive clustering to compare both cluster sizes 2 (green lines) and 4 (purple lines) as well as Gaussian sampling (dashed) and discrete sampling (solid).

prediction. Additionally, we introduced a new sampling scheme for generating Monte-Carlo trajectories which extends the discrete Wigner function known from dTWA to the realm of cTWA. Our analysis included both the XX and XXZ models with bond disorder initiated from a Néel state, and calculated dynamical observables such as staggered magnetization and two-site Rényi entropy.

We found that while cTWA generally yields improved accuracy compared to dTWA, the choice of clusters strongly impacts the results. Our results in the context of bond disorder show that a clustering strategy

inspired by the strong disorder renormalisation group could yield astonishingly precise results in the presence of strong disorder, while still being very accurate even for quite long-range interactions, weak disorder and long times. XXZ models featuring strong Ising interactions were found to be challenging for all semi-classical methods presented here and we conclude that likely larger clusters are needed to capture the relevant physical processes accurately. In all of these systems, we only found minor differences between the Gaussian and discrete sampling schemes in situations where the results were not converged in cluster size. However, a closer study of the statistical properties revealed the discrete sampling to exhibit smaller intrinsic Monte-Carlo shot noise.

In conclusion, our study provides valuable insights into the effectiveness of cTWA in studying quench dynamics in bond-disordered spin systems. If using the correct clustering strategy, even clusters of size 2 yield close to exact results, where single spin dTWA fails. Additionally, we conclude that the discrete sampling strategy introduced here is generally preferable to the Gaussian approximation due to less Monte-Carlo shot noise and somewhat simpler implementation. Overall, our results highlight the potential of cTWA and its variants, such as dcTWA, as powerful tools for studying the complex dynamics of bond-disordered quantum systems.

V. ACKNOWLEDGMENT

We thank O. Egorov for providing computational resources. We acknowledge State of Thuringia for funding of projects "2019 FGI 0017" (PhyClus) and "2022 FGI 0004" (Q-PHOC3). A.B. acknowledges support by the Deutsche Forschungsgemeinschaft (DFG, German Research Foundation) within the Collaborative Research Center SFB1225 (ISOQUANT). For the numerical work, we used the Julia programming language [59] and the following packages/tools: DrWatson.jl [60], Pluto.jl [61], DifferentialEquations.jl [62] with Verner's integration schemes [63], Makie.jl [64], DataFrames.jl [65].

-
- [1] P. W. Anderson, Absence of diffusion in certain random lattices, *Phys. Rev.* **109**, 1492 (1958).
 - [2] N. F. Mott, Impurity band conduction. experiment and theory the metal-insulator transition in an impurity band., *Le Journal de Physique Colloques* **37**, C4 (1976).
 - [3] S. Kettemann, Towards a comprehensive theory of metal-insulator transitions in doped semiconductors, *Annals of Physics* **456**, 169306 (2023).
 - [4] L. D. Cesare, K. Lukierska-Walasek, I. Rabuffo, and K. Walasek, Two-spin cluster approach to the infinite-range quantum transverse XY spin-glass model, *Physics Letters A* **145**, 291 (1990).
 - [5] L. De Cesare, K. Lukierska-Walasek, I. Rabuffo, and K. Walasek, Cavity-fields approach to quantum xy spin-glass models in a transverse field, *Phys. Rev. B* **45**, 1041 (1992).
 - [6] A. de Paz, A. Sharma, A. Chotia, E. Maréchal, J. H. Huckans, P. Pedri, L. Santos, O. Gorceix, L. Vernac, and B. Laburthe-Tolra, Nonequilibrium quantum magnetism in a dipolar lattice gas, *Phys. Rev. Lett.* **111**, 185305 (2013).
 - [7] B. Yan, S. A. Moses, B. Gadway, J. P. Covey, K. R. A. Hazzard, A. M. Rey, D. S. Jin, and J. Ye, Observation of dipolar spin-exchange interactions with lattice-confined polar molecules, *Nature* **501**, 521 (2013).

- [8] P. Fersterer, A. Safavi-Naini, B. Zhu, L. Gabardos, S. Lepoutre, L. Vernac, B. Laburthe-Tolra, P. B. Blakie, and A. M. Rey, Dynamics of an itinerant spin-3 atomic dipolar gas in an optical lattice, *Phys. Rev. A* **100**, 033609 (2019).
- [9] J. Zeiher, J.-y. Choi, A. Rubio-Abadal, T. Pohl, R. van Bijnen, I. Bloch, and C. Gross, Coherent many-body spin dynamics in a long-range interacting ising chain, *Phys. Rev. X* **7**, 041063 (2017).
- [10] H. Bernien, S. Schwartz, A. Keesling, H. Levine, A. Omran, H. Pichler, S. Choi, A. S. Zibrov, M. Endres, M. Greiner, V. Vuletić, and M. D. Lukin, Probing many-body dynamics on a 51-atom quantum simulator, *Nature* **551**, 579 (2017).
- [11] A. Keesling, A. Omran, H. Levine, H. Bernien, H. Pichler, S. Choi, R. Samajdar, S. Schwartz, P. Silvi, S. Sachdev, P. Zoller, M. Endres, M. Greiner, V. Vuletić, and M. D. Lukin, Quantum kibble–zurek mechanism and critical dynamics on a programmable rydberg simulator, *Nature* **568**, 207 (2019).
- [12] R. Islam, C. Senko, W. C. Campbell, S. Korenblit, J. Smith, A. Lee, E. E. Edwards, C.-C. J. Wang, J. K. Freericks, and C. Monroe, Emergence and frustration of magnetism with variable-range interactions in a quantum simulator, *Science* **340**, 583 (2013).
- [13] P. Jurcevic, B. P. Lanyon, P. Hauke, C. Hempel, P. Zoller, R. Blatt, and C. F. Roos, Quasiparticle engineering and entanglement propagation in a quantum many-body system, *Nature* **511**, 202 (2014).
- [14] P. Richerme, Z.-X. Gong, A. Lee, C. Senko, J. Smith, M. Foss-Feig, S. Michalakis, A. V. Gorshkov, and C. Monroe, Non-local propagation of correlations in quantum systems with long-range interactions, *Nature* **511**, 198 (2014).
- [15] M. Gärttner, J. G. Bohnet, A. Safavi-Naini, M. L. Wall, J. J. Bollinger, and A. M. Rey, Measuring out-of-time-order correlations and multiple quantum spectra in a trapped-ion quantum magnet, *Nature Physics* **13**, 781 (2017).
- [16] A. Signoles, T. Franz, R. Ferracini Alves, M. Gärttner, S. Whitlock, G. Zürn, and M. Weidemüller, Glassy dynamics in a disordered heisenberg quantum spin system, *Phys. Rev. X* **11**, 011011 (2021).
- [17] A. Nauts and R. E. Wyatt, New approach to many-state quantum dynamics: The recursive-residue-generation method, *Phys. Rev. Lett.* **51**, 2238 (1983).
- [18] T. J. Park and J. C. Light, Unitary quantum time evolution by iterative Lanczos reduction, *The Journal of Chemical Physics* **85**, 5870 (1986).
- [19] L. Colmenarez and D. J. Luitz, Lieb-robinson bounds and out-of-time order correlators in a long-range spin chain, *Phys. Rev. Res.* **2**, 043047 (2020).
- [20] J. Vahedi, Asymmetric transport in long-range interacting chiral spin chains, *SciPost Phys. Core* **5**, 021 (2022).
- [21] M. Faridfar and J. Vahedi, Thermodynamic behavior of spin-1 heisenberg chain: a comparative study, *Journal of Superconductivity and Novel Magnetism* **35**, 519 (2022).
- [22] U. Schollwoeck, The density-matrix renormalization group in the age of matrix product states, *Annals of Physics* **326**, 96 (2011).
- [23] G. Vidal, Efficient classical simulation of slightly entangled quantum computations, *Phys. Rev. Lett.* **91**, 147902 (2003).
- [24] S. R. White and A. E. Feiguin, Real-time evolution using the density matrix renormalization group, *Phys. Rev. Lett.* **93**, 076401 (2004).
- [25] M. P. Zaletel, R. S. K. Mong, C. Karrasch, J. E. Moore, and F. Pollmann, Time-evolving a matrix product state with long-ranged interactions, *Phys. Rev. B* **91**, 165112 (2015).
- [26] S. Paeckel, T. Köhler, A. Swoboda, S. R. Manmana, U. Schollwöck, and C. Hubig, Time-evolution methods for matrix-product states, *Annals of Physics* **411**, 167998 (2019).
- [27] P. Blakie†, A. Bradley†, M. Davis, R. Ballagh, and C. Gardiner, Dynamics and statistical mechanics of ultracold bose gases using c-field techniques, *Advances in Physics* **57**, 363 (2008).
- [28] A. Polkovnikov, Phase space representation of quantum dynamics, *Annals of Physics* **325**, 1790 (2010).
- [29] A. K. Tuchman, C. Orzel, A. Polkovnikov, and M. A. Kasevich, Nonequilibrium coherence dynamics of a soft boson lattice, *Phys. Rev. A* **74**, 051601 (2006).
- [30] S. M. Davidson, D. Sels, and A. Polkovnikov, Semiclassical approach to dynamics of interacting fermions, *Annals of Physics* **384**, 128 (2017).
- [31] K. Nagao, M. Kunimi, Y. Takasu, Y. Takahashi, and I. Danshita, Semiclassical quench dynamics of bose gases in optical lattices, *Phys. Rev. A* **99**, 023622 (2019).
- [32] S. R. Muleady, M. Yang, S. R. White, and A. M. Rey, Validating Phase-Space Methods with Tensor Networks in Two-Dimensional Spin Models with Power-Law Interactions, *Phys. Rev. Lett.* **131**, 150401 (2023).
- [33] C. D. Mink, D. Petrosyan, and M. Fleischhauer, Hybrid discrete-continuous truncated Wigner approximation for driven, dissipative spin systems, *Phys. Rev. Res.* **4**, 043136 (2022).
- [34] W. K. Wootters, A wigner-function formulation of finite-state quantum mechanics, *Annals of Physics* **176**, 1 (1987).
- [35] J. Schachenmayer, A. Pikovski, and A. M. Rey, Many-body quantum spin dynamics with monte carlo trajectories on a discrete phase space, *Phys. Rev. X* **5**, 011022 (2015).
- [36] J. Schachenmayer, A. Pikovski, and A. M. Rey, Dynamics of correlations in two-dimensional quantum spin models with long-range interactions: a phase-space monte-carlo study, *New Journal of Physics* **17**, 065009 (2015).
- [37] L. Pucci, A. Roy, and M. Kastner, Simulation of quantum spin dynamics by phase space sampling of bogoliubov-born-green-kirkwood-yvon trajectories, *Phys. Rev. B* **93**, 174302 (2016).
- [38] O. L. Acevedo, A. Safavi-Naini, J. Schachenmayer, M. L. Wall, R. Nandkishore, and A. M. Rey, Exploring many-body localization and thermalization using semiclassical methods, *Phys. Rev. A* **96**, 033604 (2017).
- [39] A. Piñeiro Orioli, A. Safavi-Naini, M. L. Wall, and A. M. Rey, Nonequilibrium dynamics of spin-boson models from phase-space methods, *Phys. Rev. A* **96**, 033607 (2017).
- [40] S. Czischeck, M. Gärttner, M. Oberthaler, M. Kastner, and T. Gasenzer, Quenches near criticality of the quantum ising chain—power and limitations of the discrete truncated wigner approximation, *Quantum Science and Technology* **4**, 014006 (2018).
- [41] A. Piñeiro Orioli, A. Signoles, H. Wildhagen, G. Günter, J. Berges, S. Whitlock, and M. Weidemüller, Relaxation

- of an isolated dipolar-interacting rydberg quantum spin system, *Phys. Rev. Lett.* **120**, 063601 (2018).
- [42] B. Sundar, K. C. Wang, and K. R. A. Hazzard, Analysis of continuous and discrete wigner approximations for spin dynamics, *Phys. Rev. A* **99**, 043627 (2019).
- [43] R. Khasseh, A. Russomanno, M. Schmitt, M. Heyl, and R. Fazio, Discrete truncated wigner approach to dynamical phase transitions in ising models after a quantum quench, *Phys. Rev. B* **102**, 014303 (2020).
- [44] M. Kunimi, K. Nagao, S. Goto, and I. Danshita, Performance evaluation of the discrete truncated wigner approximation for quench dynamics of quantum spin systems with long-range interactions, *Phys. Rev. Res.* **3**, 013060 (2021).
- [45] W. Morong, S. R. Muleady, I. Kimchi, W. Xu, R. M. Nandkishore, A. M. Rey, and B. DeMarco, Disorder-controlled relaxation in a three-dimensional hubbard model quantum simulator, *Phys. Rev. Res.* **3**, L012009 (2021).
- [46] S. M. Davidson and A. Polkovnikov, $su(3)$ semiclassical representation of quantum dynamics of interacting spins, *Phys. Rev. Lett.* **114**, 045701 (2015).
- [47] J. Wurtz, A. Polkovnikov, and D. Sels, Cluster truncated wigner approximation in strongly interacting systems, *Annals of Physics* **395**, 341 (2018).
- [48] B. Zhu, A. M. Rey, and J. Schachenmayer, A generalized phase space approach for solving quantum spin dynamics, *New Journal of Physics* **21**, 082001 (2019).
- [49] K. Nagao and S. Yunoki, Two-dimensional correlation propagation dynamics with a cluster discrete phase-space method (2024), arxiv:2404.18594 [cond-mat, physics:quant-ph].
- [50] Y. Mohdeb, J. Vahedi, N. Moure, A. Roshani, H.-Y. Lee, R. N. Bhatt, S. Kettemann, and S. Haas, Entanglement properties of disordered quantum spin chains with long-range antiferromagnetic interactions, *Phys. Rev. B* **102**, 214201 (2020).
- [51] Y. Mohdeb, J. Vahedi, and S. Kettemann, Excited-eigenstate entanglement properties of xx spin chains with random long-range interactions, *Phys. Rev. B* **106**, 104201 (2022).
- [52] Y. Mohdeb, J. Vahedi, R. N. Bhatt, S. Haas, and S. Kettemann, Global quench dynamics and the growth of entanglement entropy in disordered spin chains with tunable range interactions, *Phys. Rev. B* **108**, L140203 (2023).
- [53] E. Altman and R. Vosk, Universal Dynamics and Renormalization in Many-Body-Localized Systems, *Annual Review of Condensed Matter Physics* **6**, 383 (2015).
- [54] R. Vasseur, A. C. Potter, and S. A. Parameswaran, Quantum Criticality of Hot Random Spin Chains, *Physical Review Letters* **114**, 217201 (2015).
- [55] F. Iglói and C. Monthus, Strong disorder RG approach – a short review of recent developments, *The European Physical Journal B* **91**, 290 (2018).
- [56] <https://github.com/abraemer/DiscreteCTWAPaper>.
- [57] A. Braemer, T. Franz, M. Weidemüller, and M. Gärttner, Pair localization in dipolar systems with tunable positional disorder, *Phys. Rev. B* **106**, 134212 (2022).
- [58] S. Geier, N. Thaicharoen, C. Hainaut, T. Franz, A. Salzinger, A. Tebben, D. Grimshndl, G. Zürn, and M. Weidemüller, Floquet Hamiltonian engineering of an isolated many-body spin system, *Science* **374**, 1149 (2021).
- [59] J. Bezanson, A. Edelman, S. Karpinski, and V. B. Shah, Julia: A Fresh Approach to Numerical Computing, *SIAM Review* **59**, 65 (2017).
- [60] G. Datseris, J. Isensee, S. Pech, and T. Gál, DrWatson: The perfect sidekick for your scientific inquiries, *Journal of Open Source Software* **5**, 2673 (2020).
- [61] Fons van der Plas, M. Dral, P. Berg, P. Γεωργακόπουλος, R. Huijzer, M. Bocheński, A. Mengali, C. Burns, B. Lungwitz, H. Priyashan, J. Ling, G. Wu, S. Kadawaki, E. Zhang, F. S. S. Schneider, I. Weaver, Xiu-zhe (Roger) Luo, J. Gerritsen, R. Novosel, Supanat, Z. Moon, L. Müller, Timothy, V. Flore, Jeremiah, C. O'Mara, M. Hatherly, and kcin96, Fonsp/Pluto.jl: V0.19.42, Zenodo (2024).
- [62] C. Rackauckas and Q. Nie, Differentialequations.jl—a performant and feature-rich ecosystem for solving differential equations in julia, *Journal of Open Research Software* **5**, 15 (2017).
- [63] J. H. Verner, Numerically optimal Runge–Kutta pairs with interpolants, *Numerical Algorithms* **53**, 383 (2010).
- [64] S. Danisch and J. Krumbiegel, Makie.jl: Flexible high-performance data visualization for Julia, *Journal of Open Source Software* **6**, 3349 (2021).
- [65] M. Bouchet-Valat and B. Kamiński, Dataframes.jl: Flexible and fast tabular data in julia, *Journal of Statistical Software* **107**, 1 (2023).

Appendix A: Sampling from discrete Wigner functions of spin clusters

In this section, we first recapitulate how to derive the concrete sampling rules of dTWA and then extend the scheme to clusters of multiple spins. Finally, we provide a concrete example of sampling rules for clusters of 2 spins. The concepts described here are similar to [37] Appendix A.

1. Recap: Sampling a single spin

Earlier in section II B 2, we defined the phase-point operators for a single spin

$$\hat{A}_{p,q} = (\mathbb{1} + \mathbf{r}(p,q) \cdot \hat{\sigma})/2 \quad (\text{A1})$$

via a choice of phase-point vectors $\mathbf{r}(p,q)$. In principle there are many possible choices for $\mathbf{r}(p,q)$ but since there are a total of 8 discrete spin states, two sets of phase point operators are enough to cover all possible states. We define the two sets of phase-point operators (see [40] Fig. 2 for a visualization) via

$$r^1(0,0) = (1,1,1), \quad (\text{A2a})$$

$$r^1(0,1) = (-1,-1,1), \quad (\text{A2b})$$

$$r^1(1,0) = (1,-1,-1), \quad (\text{A2c})$$

$$r^1(1,1) = (-1,1,-1), \quad (\text{A2d})$$

and

$$r^2(0,0) = (1, -1, 1), \quad (\text{A3a})$$

$$r^2(0,1) = (-1, 1, 1), \quad (\text{A3b})$$

$$r^2(1,0) = (1, 1, -1), \quad (\text{A3c})$$

$$r^2(1,1) = (-1, -1, -1). \quad (\text{A3d})$$

With this choice, we can define the Wigner function of some quantum state $\hat{\rho}$ as

$$w^s(p, q; \hat{\rho}) = \frac{1}{2} \text{Tr } \hat{\rho} \hat{A}_{(p,q)}^s \quad (\text{A4})$$

where $s = 1, 2$ denotes the set of phase-point operators. These are normalized for each set, i.e. $\sum_{p,q} w^s(p, q; \hat{\rho}) = \text{Tr } \hat{\rho} = 1$ independent of s , and thus quasi-probability distributions. In case all values of a $w^s(p, q; \hat{\rho})$ are positive, we can treat it as a probability distribution and sample initial conditions for the truncated Wigner approximation from it. For a single spin, it is always possible to rotate the phase-point operators to render the Wigner functions positive, so we can always sample from either one of the two possible choices of Wigner functions. In fact it is crucial to employ both choices for sampling to prevent the introduction of spurious correlations (see example below) [33, 40]. To be explicit, the complete sampling procedure for a single trajectory first randomly selects one of the phase-space representation and then draws a phase-space vector according to its Wigner function.

We illustrate this prescription using the state $\rho = |\uparrow\rangle\langle\uparrow|$ as an example. The Wigner functions read:

$$\mathbf{w}^1(\rho) = \begin{pmatrix} w^1(0,0) & w^1(0,1) \\ w^1(1,0) & w^1(1,1) \end{pmatrix} = \begin{pmatrix} \frac{1}{2} & \frac{1}{2} \\ 0 & 0 \end{pmatrix} \quad (\text{A5a})$$

$$\mathbf{w}^2(\rho) = \begin{pmatrix} w^2(0,0) & w^2(0,1) \\ w^2(1,0) & w^2(1,1) \end{pmatrix} = \begin{pmatrix} \frac{1}{2} & \frac{1}{2} \\ 0 & 0 \end{pmatrix} \quad (\text{A5b})$$

Choosing one of these Wigner functions at random and then sampling from it is equivalent to drawing a sample from the set $\{r^1(0,0), r^1(0,1), r^2(0,0), r^2(0,1)\}$. In turn, this just means, we need to set the z -component to 1 and choose x and y independently from ± 1 . We remark that this prescription reproduces all moments of the spin operators $\langle (\hat{\sigma}_{x,y,z})^k \rangle$ in contrast to the Gaussian approximation which reproduces means and covariances only. Additionally, we remark that every possible phase-point of \mathbf{w}^1 (\mathbf{w}^2) has the x and y -components aligned (anti-aligned), which is the spurious correlation mentioned earlier. By using both Wigner functions, we avoid artifacts caused by this, making the simulation more accurate.

2. Generalization to clusters of spins

The prescription, we just outlined, readily generalizes to clusters of spins by taking tensor products of the phase-point operators. Consider a cluster of n spins:

The joint Hilbert space is now $SU(D)$, where $D = 2^n$, given from the tensor product of Hilbert spaces of the single spins. In the following, we essentially repeat the construction from before applied to the cluster's Hilbert space and exploit its product structure. We denote the operator basis of a cluster of n spins by \mathbf{X}_n , which can be constructed recursively by

$$\hat{\mathbf{X}}_1 \equiv \hat{\sigma} \quad (\text{A6a})$$

$$[\hat{\mathbf{X}}_n]_i = \begin{cases} \hat{\sigma}_i \otimes \mathbb{1} & i \in \{1, 2, 3\} \\ \mathbb{1} \otimes \hat{\sigma}_{i-3} & i \in \{4, 5, 6\} \\ [\hat{\mathbf{X}}_1 \otimes \hat{\mathbf{X}}_{n-1}]_{i-6} & \text{else} \end{cases}, \quad (\text{A6b})$$

where $[\cdot]_i$ denotes the i -th component of the vector.

In much the same way, we can construct the phase-point vectors. However, we need to consider that we have two possible choices for each spin to make, so there are a total of 2^n sets of phase-point operators. Using $\mathbf{s} \in \{1, 2\}^n$, we can construct the phase-point vectors corresponding to the operator basis defined above as:

$$\begin{aligned} \mathbf{r}_n^{\mathbf{s}}(\mathbf{p}, \mathbf{q}) = & \mathbf{r}^{s_1}(p_1, q_1) \\ & \oplus \mathbf{r}_{n-1}^{\tilde{\mathbf{s}}}(\tilde{\mathbf{p}}, \tilde{\mathbf{q}}) \\ & \oplus [\mathbf{r}^{s_1}(p_1, q_1) \otimes \mathbf{r}_{n-1}^{\tilde{\mathbf{s}}}(\tilde{\mathbf{p}}, \tilde{\mathbf{q}})] \end{aligned} \quad (\text{A7})$$

where the vectors with tilde ($\tilde{\mathbf{s}}$, $\tilde{\mathbf{p}}$ and $\tilde{\mathbf{q}}$) are the same as the bare vectors without the first element, e.g. $\tilde{\mathbf{s}} = (s_2, \dots, s_n)$. From these building blocks, we can define the Wigner functions of the cluster as

$$w^{\mathbf{s}}(\mathbf{p}, \mathbf{q}; \hat{\rho}) = \frac{1}{2^n} \text{Tr } \hat{\rho} \hat{A}_{(\mathbf{p}, \mathbf{q})}^{\mathbf{s}} \quad (\text{A8})$$

$$= \frac{1}{4^n} \text{Tr } \hat{\rho} \left(\mathbb{1} + \mathbf{r}_n^{\mathbf{s}}(\mathbf{p}, \mathbf{q}) \cdot \hat{\mathbf{X}}_n \right). \quad (\text{A9})$$

As can be checked easily via induction, this definition gives us a normalized Wigner function for every choice of \mathbf{s} .

Another short calculation shows, that if the quantum state $\hat{\rho}$ factorizes between the spins, i.e. $\rho = \bigotimes_{i \leq n} \hat{\rho}_i$, then the Wigner function factorizes as well:

$$w^{\mathbf{s}}(\mathbf{p}, \mathbf{q}; \bigotimes_{i \leq n} \hat{\rho}_i) = \prod_{i \leq n} w^{s_i}(p_i, q_i; \hat{\rho}_i) \quad (\text{A10})$$

This allows for efficient sampling.

To derive rules for sampling initial states, conceptually one needs to choose a random set of phase-point representations, i.e. draw \mathbf{s} randomly, and then choose a phase-space vector $\mathbf{r}_n^{\mathbf{s}}(\mathbf{p}, \mathbf{q})$ with a probability determined by the corresponding Wigner function $w^{\mathbf{s}}(\mathbf{p}, \mathbf{q})$. In case of a product initial state, this prescription simplifies dramatically because we choose the phase-space vector of each spin independently and compute the initial value of correlators by products (see Eq. A8).

We illustrate the prescription given above using the Neel-state $\hat{\rho} = |\uparrow\downarrow\rangle\langle\uparrow\downarrow|$. Applying the rule for product states, we can immediately state the sampling scheme:

Index i	Operator X_i	Initial value	Term in Eq. A15
1	$\langle \hat{\sigma}_x^1 \rangle$	1	
2	$\langle \hat{\sigma}_y^1 \rangle$	1	$\mathbf{r}^1(0, 0)$
3	$\langle \hat{\sigma}_z^1 \rangle$	1	
4	$\langle \hat{\sigma}_x^2 \rangle$	1	
5	$\langle \hat{\sigma}_y^2 \rangle$	1	$\mathbf{r}^1(1, 0)$
6	$\langle \hat{\sigma}_z^2 \rangle$	-1	
7	$\langle \hat{\sigma}_x^1 \hat{\sigma}_x^2 \rangle$	1	
8	$\langle \hat{\sigma}_x^1 \hat{\sigma}_y^2 \rangle$	1	
9	$\langle \hat{\sigma}_x^1 \hat{\sigma}_z^2 \rangle$	-1	
10	$\langle \hat{\sigma}_y^1 \hat{\sigma}_x^2 \rangle$	1	
11	$\langle \hat{\sigma}_y^1 \hat{\sigma}_y^2 \rangle$	1	$\mathbf{r}^1(0, 0) \otimes \mathbf{r}^1(1, 0)$
12	$\langle \hat{\sigma}_y^1 \hat{\sigma}_z^2 \rangle$	-1	
13	$\langle \hat{\sigma}_z^1 \hat{\sigma}_x^2 \rangle$	1	
14	$\langle \hat{\sigma}_z^1 \hat{\sigma}_y^2 \rangle$	1	
15	$\langle \hat{\sigma}_z^1 \hat{\sigma}_z^2 \rangle$	-1	

TABLE I. Coefficients for the phase-point vector given in Eq. A15

Set $\langle \hat{\sigma}_z^1 \rangle = -\langle \hat{\sigma}_z^2 \rangle = 1$, choose $\langle \hat{\sigma}_x^1 \rangle, \langle \hat{\sigma}_y^1 \rangle, \langle \hat{\sigma}_x^2 \rangle, \langle \hat{\sigma}_y^2 \rangle$ randomly from $\{-1, 1\}$ and then compute the initial values of the correlators by products, e.g. $\langle \hat{\sigma}_x^1 \hat{\sigma}_x^2 \rangle = \langle \hat{\sigma}_x^1 \rangle \langle \hat{\sigma}_x^2 \rangle$.

Alternatively, we can employ the tedious route and compute all the Wigner functions. We start by computing the single spin Wigner functions, which for $|\uparrow\rangle\langle\downarrow|$ are given in Eqs. A5a and A5b. Similarly for $|\downarrow\rangle\langle\uparrow|$, we find

$$\mathbf{w}^1(|\downarrow\rangle) = \mathbf{w}^2(|\downarrow\rangle) = \begin{pmatrix} 0 & 0 \\ \frac{1}{2} & \frac{1}{2} \end{pmatrix} . \quad (\text{A11})$$

From this we can compute the full two-spin Wigner functions:

$$\begin{aligned} \mathbf{w}^{(1,1)} &= \mathbf{w}^{(2,2)} = \mathbf{w}^1(|\uparrow\rangle) \otimes \mathbf{w}^1(|\downarrow\rangle) \\ &= \begin{pmatrix} w^1(|\uparrow\rangle)(0,0) \cdot \mathbf{w}^1(|\downarrow\rangle) & w^1(|\uparrow\rangle)(0,1) \cdot \mathbf{w}^1(|\downarrow\rangle) \\ w^1(|\uparrow\rangle)(1,0) \cdot \mathbf{w}^1(|\downarrow\rangle) & w^1(|\uparrow\rangle)(1,1) \cdot \mathbf{w}^1(|\downarrow\rangle) \end{pmatrix} \\ &= \begin{pmatrix} 0 & 0 & 0 & 0 \\ \frac{1}{4} & \frac{1}{4} & \frac{1}{4} & \frac{1}{4} \\ 0 & 0 & 0 & 0 \\ 0 & 0 & 0 & 0 \end{pmatrix} \end{aligned} \quad (\text{A12})$$

$$\mathbf{w}^{(1,2)} = \mathbf{w}^{(2,1)} = \begin{pmatrix} 0 & 0 & 0 & 0 \\ 0 & 0 & 0 & 0 \\ \frac{1}{4} & \frac{1}{4} & \frac{1}{4} & \frac{1}{4} \\ 0 & 0 & 0 & 0 \end{pmatrix} \quad (\text{A13})$$

To generate a single sample, we first need to select one of the 4 Wigner functions, e.g. $w^{(1,1)}$. This Wigner function gives us the probability distribution to choose the state from, which in this case means, we need to

select one of the phase-points (\mathbf{p}, \mathbf{q}) from the set

$$\left\{ \left[\begin{pmatrix} 0 \\ 1 \end{pmatrix}, \begin{pmatrix} 0 \\ 0 \end{pmatrix} \right], \left[\begin{pmatrix} 0 \\ 1 \end{pmatrix}, \begin{pmatrix} 0 \\ 1 \end{pmatrix} \right], \right. \\ \left. \left[\begin{pmatrix} 0 \\ 1 \end{pmatrix}, \begin{pmatrix} 1 \\ 0 \end{pmatrix} \right], \left[\begin{pmatrix} 0 \\ 1 \end{pmatrix}, \begin{pmatrix} 1 \\ 1 \end{pmatrix} \right] \right\} \quad (\text{A14})$$

with equal probability. Assuming we selected the first phase-point, then the corresponding phase-space vector is given by:

$$\mathbf{r}_2^{(1,1)} \left(\begin{pmatrix} 0 \\ 1 \end{pmatrix}, \begin{pmatrix} 0 \\ 0 \end{pmatrix} \right) = \mathbf{r}^1(0, 0) \oplus \mathbf{r}^1(1, 0) \oplus (\mathbf{r}^1(0, 0) \otimes \mathbf{r}^1(1, 0)) \quad (\text{A15})$$

The corresponding initial values of the trajectory are given explicitly in Tab. I.

Appendix B: Single pair dynamics

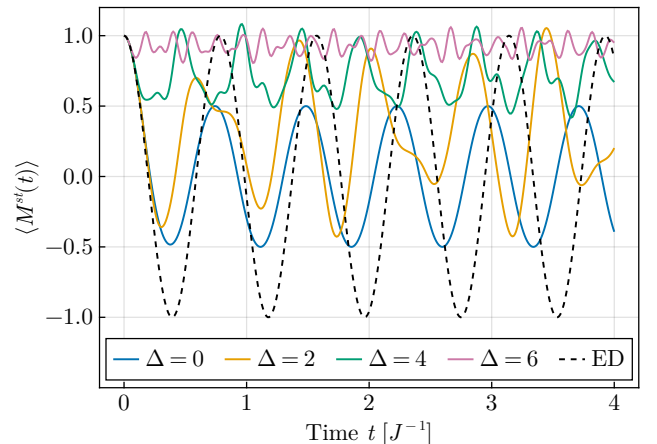


FIG. 13. Dynamics of the staggered magnetization for 2 spins with XXZ interaction for various anisotropies Δ . Shown is the exact solution (black, dashed) and solutions obtained with dTWA (colors, solid). The exact dynamics are independent of Δ , so only a single curve is shown.

To illustrate the inaccuracy of dTWA in the presence of XX interactions, we study the same system as in the main text for two spins. Repeating the definition here for convenience, we consider the Hamiltonian

$$\hat{H} = 2J (\hat{\sigma}_x^1 \hat{\sigma}_x^2 + \hat{\sigma}_y^1 \hat{\sigma}_y^2) + 2\Delta \hat{\sigma}_z^1 \hat{\sigma}_z^2 , \quad (\text{B1})$$

the initial state $|\psi_0\rangle = |\uparrow\downarrow\rangle$ and the observable $\hat{M}^{st} = \frac{1}{2}(\hat{\sigma}_z^1 + \hat{\sigma}_z^2)$. Since this Hamiltonian conserves total z -magnetization $\hat{M}_z = \hat{\sigma}_z^1 + \hat{\sigma}_z^2$, the dynamics stays confined to the zero magnetization sector, where the state oscillates back and forth between $|\uparrow\downarrow\rangle \leftrightarrow |\downarrow\uparrow\rangle$. So the exact solution reads $\langle \hat{M}^{st}(t) \rangle = \cos(8Jt)$. This is independent

of Δ , because the ZZ-term $\hat{\sigma}_z^1 \hat{\sigma}_z^2$ of course commutes with \hat{M}_z and thus cannot introduce additional couplings.

Setting $J = 1$ and using dTWA to solve the dynamics for several values of Δ , we see that the semi-classical solution is both influenced strongly by the value of Δ and yields inaccurate results even for $\Delta = 0$ (cf. Fig. 13).

6

EVIDENCE OF PAIR LOCALIZATION IN DYNAMICS OF RYDBERG SPINS

In this chapter, we apply the previously derived effective model of pairs to model and interpret experimental results from a Rydberg-based quantum simulator. While the experiment is limited to global control and readout, we make great use of its ability to implement models with different anisotropy and various density (which translates to disorder strength).

We find the pair model to yield an excellent agreement with the observed behavior explaining both the relaxation dynamics and rescaling thereof [B] as well as the dependence of the steady state magnetization on the strength of the transverse field [C].

6.1 ANISOTROPY-INDEPENDENT RELAXATION DYNAMICS

In this paper, we utilize the ability of the Rydberg quantum simulator to implement XX, XXZ and Ising models to measure the relaxation of the x -magnetization when starting from a fully magnetized state. For disordered Ising models prior work has shown the relaxation to follow a stretched exponential form well-known from spin glasses [32–35]. It has been conjectured that this type of slow, hierarchical relaxation is a common feature of strongly disordered quantum systems [36].

Indeed we find that for all three models the relaxation curves are fitted well by stretched exponentials. Moreover, we also find a scaling law for the characteristic decay time scale which hints at a common origin of the relaxation. This mechanism is explained by the pair model, which yields that for all three models the relaxation is caused essentially by oscillations of the magnetization of pairs. Since each pair has a different oscillation frequency these individual oscillations dephase and thus cause the total magnetization to decay. From the parameter dependence of these pair oscillations, we recover the characteristic timescale for the global magnetization's decay. Thus demonstrating an effect pair localization at least over experimentally relevant timescales.

Observation of universal relaxation dynamics in disordered quantum spin systems

T. Franz,^{1,2,*} S. Geier,^{1,*} C. Hainaut,^{1,3} A. Braemer,^{1,4} N. Thaicharoen,^{1,5}
M. Hornung,¹ E. Braun,¹ M. Gärttner,^{1,4,6,7} G. Zürn,¹ and M. Weidemüller^{1,†}

¹*Physikalisches Institut, Universität Heidelberg, Im Neuenheimer Feld 226, 69120 Heidelberg, Germany*

²*Max-Planck-Institut für Quantenoptik, Hans-Kopfermann-Str. 1, Garching, Germany*

³*Université de Lille, CNRS, UMR 8523-PhLAM-Laboratoire de Physique des Lasers Atomes et Molécules, F-59000 Lille, France*

⁴*Kirchhoff-Institut für Physik, Universität Heidelberg,
Im Neuenheimer Feld 227, 69120 Heidelberg, Germany*

⁵*Department of Physics and Materials Science, Faculty of Science,
Chiang Mai University, Chiang Mai 50200, Thailand*

⁶*Institut für Theoretische Physik, Ruprecht-Karls-Universität Heidelberg, Philosophenweg 16, 69120 Heidelberg, Germany*

⁷*Institute of Condensed Matter Theory and Optics,
Friedrich-Schiller-University Jena, Max-Wien-Platz 1, 07743 Jena, Germany*

(Dated: September 27, 2023)

A major goal toward understanding far-from-equilibrium dynamics of quantum many-body systems consists in finding indications of universality in the sense that the dynamics no longer depends on microscopic details of the system. We realize a large range of many-body spin systems on a Rydberg atom quantum simulator by choosing appropriate Rydberg state combinations. We use this platform to compare the magnetization relaxation dynamics of disordered Heisenberg XX-, XXZ- and Ising Hamiltonians in a scalable fashion. After appropriate rescaling of evolution time, all the dynamics collapse onto a single curve. We find that the observed behavior is approximately captured by an integrable model that only considers local pairs of spins. These pairs exhibit oscillations independent of the type of Hamiltonian which explains the universal character of relaxation dynamics of disordered Heisenberg quantum spin systems.

I. INTRODUCTION

Far-from equilibrium dynamics of isolated quantum systems after a quench displays a wide range of emergent phenomena, such as dynamical phase transitions [1, 2], quantum many-body scars [3–5] and many-body localization (MBL) [6–10]. The time evolution of these systems after a quench generally depends strongly on the type of interactions and the distribution of interaction strengths between the particles [11]. A notable exception are systems showing (metastable) prethermal phases, where relaxation dynamics can show universal behavior, i.e. the dynamics become independent of details of the microscopic model [12–17].

When considering the role of disorder for the dynamics of quantum many-body systems, a striking characteristic of the dynamics is that they can be non-ergodic [18], which is found for example in spin glasses where relaxation becomes extremely slow [19] or in MBL systems where the dynamics is completely frozen [20]. Anomalously slow relaxation was also observed in disordered quantum spin systems that feature sub-exponential dynamics [21–25]. Remarkably, in all these different classical and quantum systems, in the strong disorder regime, the sub-exponential dynamics are well described by the same functional form, the stretched exponential law. This raises the question of the origin of this common

behavior and whether it is affected by the modification of symmetry properties of the Hamiltonian.

In classical systems, the answer to these questions is provided by the seminal work of Klafter and Shlesinger who found that a scale-invariant distribution of timescales is the common underlying mathematical structure that induces stretched-exponential relaxation [26]. Indeed, the authors proposed an intuitive understanding by considering the *parallel channels* model where an ensemble of initially fully polarized spins are coupled to an external bath at a different strength sampled from a scale-invariant distribution. Due to the coupling to the bath, each spin decays exponentially on a different timescale. Thus, the global polarization of the system yields a stretched exponential form resulting from the averaging over all the spins.

For isolated quantum systems, where the dynamics are unitary, there is no notion of decay to a bath. However, in a disordered system where the spins are randomly positioned in space, the interaction strengths between the spins can be distributed scale-invariantly. For example, it was shown analytically for the dynamics of the quantum Ising model that this scale-invariant distribution of coupling strengths induces a stretched exponential relaxation [27]. The derivation of the analytic solution is only possible because the Ising model features an extensive number of conserved quantities, i.e. it is integrable. For non-integrable models, where no analytic solution exists, generic mechanisms for describing the relaxation dynamics after a quantum quench remain largely unknown. Investigating the exact time evolution numerically is challenging due to the exponential

* These authors contributed equally to this work.

† weidemueler@uni-heidelberg.de

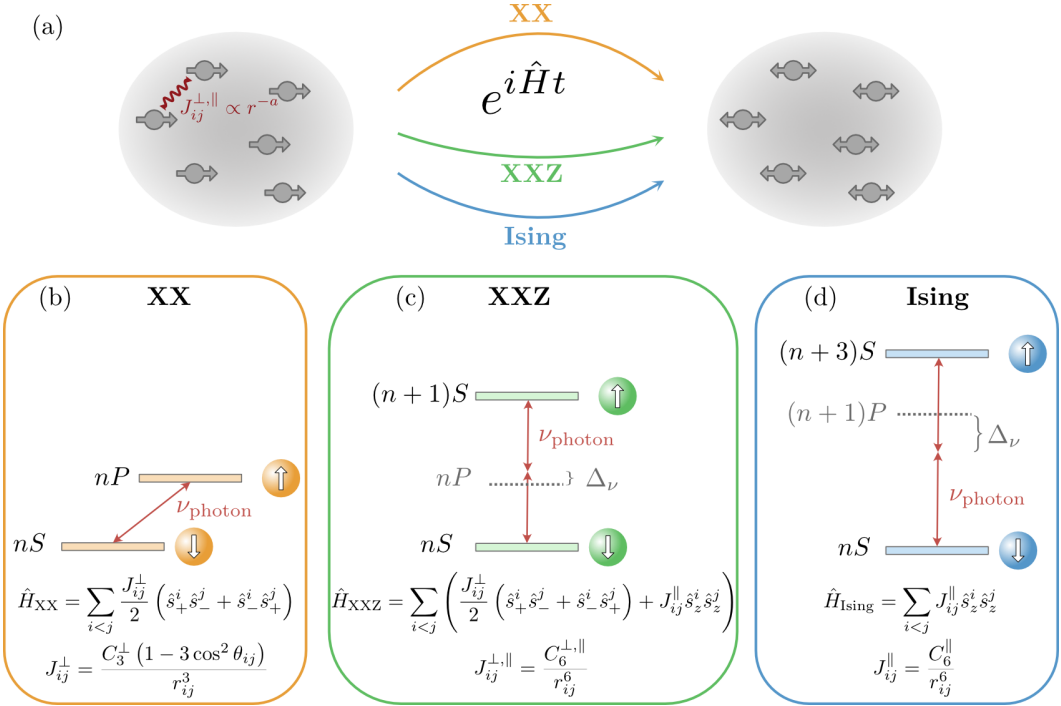


FIG. 1. Rydberg quantum simulator platform. (a) Illustration of out-of-equilibrium disordered spin systems relaxing with respect to different Hamiltonians. (b) Illustration of the experimental realization of a Heisenberg XX Hamiltonian by coupling a Rydberg $|nS\rangle$ state to a $|nP\rangle$ state, possessing opposite parity. The interaction is of dipolar nature and falls off as r_{ij}^{-3} . Coupling two Rydberg states with the same parity results in a Heisenberg XXZ Hamiltonian for state combinations $|nS\rangle$ and $|(n+1)S\rangle$ (c), while state combinations $|nS\rangle$ and $|(n+3)S\rangle$ results in a Ising Hamiltonian (d). In the two latter cases, the interactions are of van der Waals nature with a r_{ij}^{-6} dependence.

growth of the Hilbert space with system size in quantum many-body systems. Semi-classical simulations, neglecting quantum effects beyond initial quantum fluctuations, suggest that non-integrable Heisenberg XYZ Hamiltonians present out-of-equilibrium dynamics that follows a stretched exponential law like the Ising model independent of their symmetry [28]. The questions raised above can be addressed by studying the time evolution for given Hamiltonians with highly tunable quantum simulators on elaborated experimental apparatus [29–32].

In this work, we use different combinations of states of highly excited Rydberg atoms to realize different types of spin Hamiltonians thus making use of the full versatility of this platform [9, 21, 33–37]. Rydberg atoms are ideally suited to study unitary quantum dynamics because the time scales of the interacting dynamics vastly exceed those of the typical decoherence mechanisms. We observe the relaxation dynamics of three different Heisenberg Hamiltonians: the integrable Ising model and the non-integrable XX and XXZ models with power-law interactions and positional disorder (see Fig. 1 (a)). For all models, we observe the same characteristic decay of magnetization, well-described by a stretched exponential function, which causes the data to collapse onto a single universal curve after the appropriate rescaling of time. We show that this universal behavior is directly linked

to the presence of strong disorder which allows deriving an effective, integrable model consisting of pairs of spins. These results indicate that this universality is linked to the concept of prethermalization.

II. HEISENBERG SPIN SYSTEMS ON A RYDBERG-ATOM QUANTUM SIMULATOR

We consider an interacting spin-1/2 system described by the following Heisenberg Hamiltonian ($\hbar = 1$)

$$\hat{H} = \sum_{i < j} \left(J_{ij}^{\perp}/2(\hat{s}_+^i \hat{s}_-^j + \hat{s}_-^i \hat{s}_+^j) + J_{ij}^{\parallel} \hat{s}_z^i \hat{s}_z^j \right). \quad (1)$$

Here, $\hat{s}_\pm^i = \hat{s}_x^i \pm i \hat{s}_y^i$, where \hat{s}_α^i ($\alpha \in x, y, z$) are the spin-1/2 operator of spin i and $J_{ij}^{\perp,\parallel} = C_{\alpha}^{\perp,\parallel}/r^a$. These types of Heisenberg XXZ Hamiltonians with disordered couplings feature a rich phenomenology of different phases and relaxation behaviors [38]. The Ising case, where $J_{ij}^{\perp} = 0$, features additional symmetries under local spin rotations \hat{s}_z^i that commute with the Hamiltonian, which make the Ising model integrable. For $J_{ij}^{\perp} \neq 0$, \hat{s}_z^i are no longer conserved and the Hamiltonian is non-integrable. We provide a comprehensive description of how to engineer this Hamiltonian with different combinations of

Rydberg states in the appendix [39, 40]. Fig. 1 illustrates the state combinations that can be used to realize the Heisenberg XX, XXZ and Ising model. For the rest of this work, the three spin models are realized by state combinations $|61S\rangle - |61P\rangle$ (XX, $J^{\parallel}/J^{\perp} = 0$), $|61S\rangle - |62S\rangle$ (XXZ, $J^{\parallel}/J^{\perp} = -0.7$) and $|61S\rangle$ (Ising, $J^{\parallel}/J^{\perp} = -400$).

III. EXPERIMENTAL OBSERVATION OF SCALING BEHAVIOR AND GLASSY DYNAMICS

The experiment starts with trapping Rubidium-87 atoms loaded in a crossed dipole trap at a temperature of $20\text{ }\mu\text{K}$ (see appendix for experimental details). The atoms are excited from the ground $|g\rangle = |5S_{1/2}, F = 2, m_F = 2\rangle$ to the Rydberg state $|61S_{1/2}, m_j = 0.5\rrangle$ by a two-photon transition with red (780 nm) and blue (480 nm) lasers that are detuned by $2\pi \cdot 98\text{ MHz}$ from the intermediate state $|e\rangle = |5P_{3/2}, F = 3, m_F = 3\rangle$. For this state, the Rydberg lifetime of $100\text{ }\mu\text{s}$ exceeds the duration of the spin experiment of $30\text{ }\mu\text{s}$. The excitation process leads to a three-dimensional cloud of $N \approx 80 - 250$ Rydberg atoms that are distributed randomly. The Van-der-Waals interaction during the excitation process imposes a minimal distance of $r_{\text{bl}} \approx 10\text{ }\mu\text{m}$ between the spins (Rydberg blockade effect). The state $|61S_{1/2}, m_j = 0.5\rangle$ is the $|\downarrow\rangle$ state of all three different spin systems, the main difference is the second Rydberg states that is addressed by choosing proper microwave coupling using an AWG setup (see appendix for details).

After having excited the ground state atoms to the down spin state, we implement a Ramsey protocol in our Rydberg experiment. To initialize the dynamics a first $\pi/2$ -microwave pulse is performed which sets the whole system in the state $|\rightarrow\rangle^{\otimes N} = 1/\sqrt{2}(|\uparrow\rangle + |\downarrow\rangle)^{\otimes N}$ and we let the system evolve over $30\text{ }\mu\text{s}$. A second $\pi/2$ -pulse at a different readout phase followed by optical de-excitation and field ionization allows a tomographic measurement of the x magnetization $\langle \hat{S}_x \rangle = \sum_i \langle \hat{s}_x^i \rangle$ [21].

The resulting relaxation dynamics of the Ising, Heisenberg XX, and XXZ models are shown in Fig. 2 (a-c). At early times, the magnetization seems to be almost perfectly conserved at $\langle \hat{S}_x \rangle = 0.5$ before the relaxation begins. This effect is attributed to the Rydberg blockade that induces a maximal interaction strength that determines the system's fastest time scale. For each model, the system relaxes to zero magnetization which can be understood by considering symmetry arguments: Indeed, the magnetization can be rewritten using the commutator relation for Pauli matrices $\langle \hat{S}_x \rangle = -i\langle [\hat{S}_y, \hat{S}_z] \rangle$. The latter term vanishes for each eigenstate $|\phi\rangle$ of the XXZ Hamiltonian because each eigenstate is also an eigenstate of $\hat{S}_z|\phi\rangle = \sum_i \hat{s}_z^{(i)}|\phi\rangle = S_z|\phi\rangle$ due to the global U(1) symmetry leading to $\langle [\hat{S}_y, \hat{S}_z] \rangle = S_z \langle [\hat{S}_y, 1] \rangle = 0$. The timescale of the dynamics occurring within less than $10\text{ }\mu\text{s}$ is comparable with the typical interaction strengths in

the megahertz regime depending on the realized Heisenberg model (details on the distribution of interaction time scales can be found in the appendix).

To compare the relaxation curves to numerical predictions, the positions of the Rydberg spins are needed. We use a hard-sphere model where each Rydberg excitation is described by a superatom [41] with a given blockade radius and effective Rabi frequency [21]. For more details on the parameters of the models see the appendix. We simulate the exact time-evolution of the experiment using the Discrete Truncated Wigner Approximation (DTWA) [42]. Compared to the experimental data in Fig. 2 (a-c), DTWA shows good agreement. The small deviation between simulations and experiments can be mostly attributed to an inaccuracy of the atom distribution obtained from the simplified excitation model (see appendix).

Despite stemming from three different spin systems, the dynamics in Fig. 2 (a-c) look strikingly similar in a log-linear plot. Indeed, by rescaling time with the typical timescale of each system given by $|J_{\text{median}}^{\perp} - J_{\text{median}}^{\parallel}|$, all relaxation curves coincide within the experimental errors. Here,

$$J_{\text{median}}^{\perp,\parallel} = \text{median}_j \max_i |J_{ij}^{\perp,\parallel}| \quad (2)$$

is the median of the nearest neighbor interaction strengths. This choice of typical interaction time scale is motivated by the oscillation frequency of a single pair of interacting spins governed by (1), which will be further discussed in the following section. This scaling behavior shows universal relaxation dynamics which is independent of the type of Hamiltonian. The striking collapse allows us to infer the functional form of the relaxation dynamics of the non-integrable models: For the Ising model, it is known that the relaxation follows exactly the stretched exponential law $e^{-(t/\tau)^{\beta}}$ [27] with stretching exponent β and timescale τ . The logarithm of the stretched exponential law is a power-law. Plotted on a double logarithmic scale, this power-law becomes a linear function (dashed line in the inset of Fig. 2 (d)). In this representation, the rescaled experimental data also show a linear behavior. This confirms the hypothesis that the stretched exponential law is the unifying description of the relaxation for the integrable quantum Ising model and also for the non-integrable XX and XXZ Hamiltonians in the strongly disordered regime. We note that the dynamics are only universal with respect to microscopic details of the system like the value of J^{\parallel}/J^{\perp} , whereas the macroscopic geometry and also the dimension of the cloud may lead to different dynamics (see appendix). In addition, we also measure the relaxation dynamics for various initial states (for one Hamiltonian) possessing different magnetization and again find similar relaxation dynamics at late times (see appendix E).

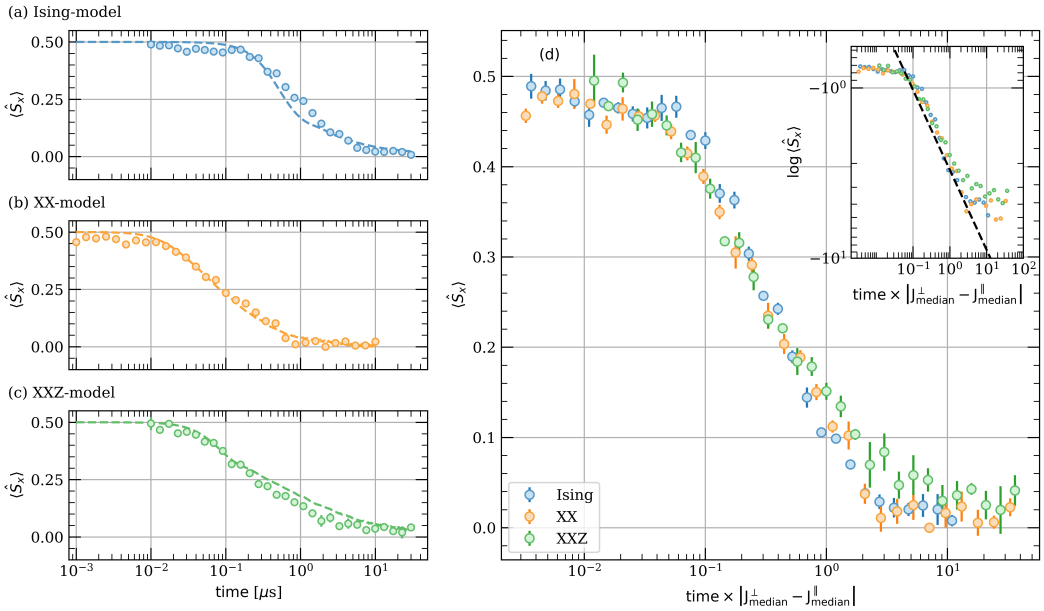


FIG. 2. Relaxation dynamics of disordered quantum spin systems. Magnetization dynamics as a function of time for the Ising-model (a), the XX-model (b), and the XXZ-model (c). The dashed lines stem from DTWA simulations. (d) Magnetization dynamics of the three models as a function of the time rescaled by the typical interaction strength $2\pi|J_{\text{median}}^{\perp} - J_{\text{median}}^{\parallel}| = 2.3 \text{ MHz}$ (Ising-model), 21 MHz (XX-model), 7.6 MHz (XXZ-model). Inset: Data points of (c) plotted on as loglog vs log. Dashed line is a guide to the eye indicating a stretched exponential relaxation with $\beta = 0.5$. The error bars denote the standard error of the mean.

IV. EFFECTIVE MODEL DESCRIPTION

In order to understand the emergence of the observed universality, we aim for a simplified model which includes only the relevant time scales of the system. To identify these, we adopt an approach in the spirit of the strong disorder renormalization group (SDRG) where the strongest coupling is integrated out iteratively [43–46].

In our model, the strongest coupled spins define a pair of spins. Then one treats the coupling between this pair and the rest of the system perturbatively. To zeroth order, this pair of spins just decouples from the system and evolves independently. This elimination step, where we remove the strongest coupling, can be repeated within the rest of the system. For our initial state, each individual pair undergoes coherent dynamics between the fully polarized state in plus and minus x-direction (see fig. 3a) [47]. The resulting oscillation of the magnetization (shown in Fig. 3 (b)) is independent of the specific XXZ Hamiltonian. Only the frequency, given by $J_{ij}^{\perp} - J_{ij}^{\parallel}$, differs depending on the Ising and exchange interaction strengths. This independence is at the origin of the observed universality of relaxation dynamics.

With this model in hand, we can compute the time evolution of the magnetization by a simple average of cosine oscillations as shown by the grey dash-dotted lines (pair,non-interacting) in fig. 3c-e. The resulting relaxation dynamics show good agreement with the experi-

mental data. However, especially for the Ising- and XXZ-model, this model underestimates the timescales of the dynamics. This is somewhat expected considering that the pair couplings found by iterative elimination are on average smaller than the nearest neighbor couplings.

Taking the perturbative treatment to next order, one finds an effective Ising-like coupling between pairs, as derived recently in the appendix of [48]. The effective Hamiltonian governing the dynamics was found to be

$$\hat{H}_{\text{eff}} \approx \sum_{\langle i,j \rangle} \left(J_{ij}^{\perp} / 2(\hat{s}_+^i \hat{s}_-^j + \hat{s}_-^i \hat{s}_+^j) + J_{ij}^{\parallel} \hat{s}_z^i \hat{s}_z^j \right) + \sum_{\langle i,j \rangle, \langle k,l \rangle} J_{ijkl}^{\text{eff}} \hat{s}_z^{(i)(j)} \hat{s}_z^{(k)(l)} \quad (3)$$

$$J_{ijkl}^{\text{eff}} = \frac{J_{ik}^{\parallel} + J_{il}^{\parallel} + J_{jk}^{\parallel} + J_{jl}^{\parallel}}{2} \quad (4)$$

where $\langle i,j \rangle$ denotes the summation over paired spins i and j and $2\hat{s}_z^{(i)(j)} = \hat{s}_z^{(i)} + \hat{s}_z^{(j)}$.

Fortunately, this model is integrable and allows for derivation of an analytical solution for the evolution of $\langle \hat{S}_x(t) \rangle$ (see Appendix F), which reads

$$\langle \hat{S}_x^{\text{pair}} \rangle(t) = \frac{1}{N} \sum_{\langle i,j \rangle} \cos\left(\frac{1}{2}(J_{ij}^{\perp} - J_{ij}^{\parallel})t\right) \prod_{\langle k,l \rangle} \cos^2\left(\frac{1}{4}J_{ijkl}^{\text{eff}}t\right). \quad (5)$$

The first factor in each term originates from the pair dynamic to zeroth order, as described previously. The

other factors are reminiscent of the Emch-Radin solution for the Ising model and stem from the effective Ising interaction among the pairs. This effective Ising model of pairs captures the overall demagnetization dynamics remarkably well for all observed times (see Fig. 3c-e) yielding very similar (and in case of XXZ even better) results compared to dTWA.

From the analytical form of the time evolution, Eq. 5, we find that many different oscillation frequencies contribute to each spin's magnetization dynamics. Most of these frequencies are very small, however, and do not contribute to the early-time dynamics. Thus, a reasonable ansatz for rescaling to make the dynamics collapse is to consider only the fastest frequency for each spin. Due to the highly disordered nature of our system, this strongest coupling will essentially always correspond to the closest neighboring spin. This explains the rescaling found from the experimental data with $\text{median}_i \max_j |J_{ij}^\perp - J_{ij}^\parallel|$.

V. RELATION TO PRETHERMALIZATION

In the previous section, we revealed that the relaxation dynamics of a single-body observable is well captured by an ensemble of pairs with Ising-like interactions. This simple description in terms of pairs provides an integrable effective Hamiltonian which is valid not only at early times but agrees surprisingly well with the data for the whole relaxation of the magnetization, which lasts for over three decades in time. This raises the question of whether this behavior could be prethermal. Prethermalization generally means, that a system does not directly relax to its 'true' thermal state, but instead reaches a prethermal state. This is still a thermal state but with respect to a different, prethermal Hamiltonian. We now want to investigate, whether our system shows prethermalization related to pairs of spins.

If the system is prethermal with respect to pairs, we expect the total z-magnetization of each pair to be conserved. This hypothesis can be tested by evaluating the pair autocorrelator given by $\langle \hat{S}_z^{\text{pair}}(t) \hat{S}_z^{\text{pair}} \rangle$, where $\hat{S}_z^{\text{pair}} = \hat{s}_z^i + \hat{s}_z^j$. If the pair picture is perfect or if the system is an Ising model, this quantity stays $\langle \hat{S}_z^{\text{pair}}(t) \hat{S}_z^{\text{pair}} \rangle = 1$. On the other hand, if the correlations in the system are fully dispersed, the autocorrelator assumes its minimal value of $\langle \hat{S}_z^{\text{pair}}(t) \hat{S}_z^{\text{pair}} \rangle = \frac{2}{N}$ for a system of size N due to symmetry constraints.

Our numerics presented in (Fig. 4) for $N = 16$ spins in $d = 1$ with interaction exponent $\alpha = 2$ reveals three important points. Firstly, at $t |J_{\text{median}}^\parallel - J_{\text{median}}^\perp| \approx 0.2$ the global magnetization $\langle \hat{S}_x \rangle$ has decayed almost by half, while the pairs' magnetization autocorrelators are still close to 1. This justifies our simplistic pair picture and highlights the regime of universal dynamics. Secondly, at intermediate times up to 10^2 , the global magnetization relaxes fully to zero while the autocorrelator still features slow dynamics. This illustrate the existence of

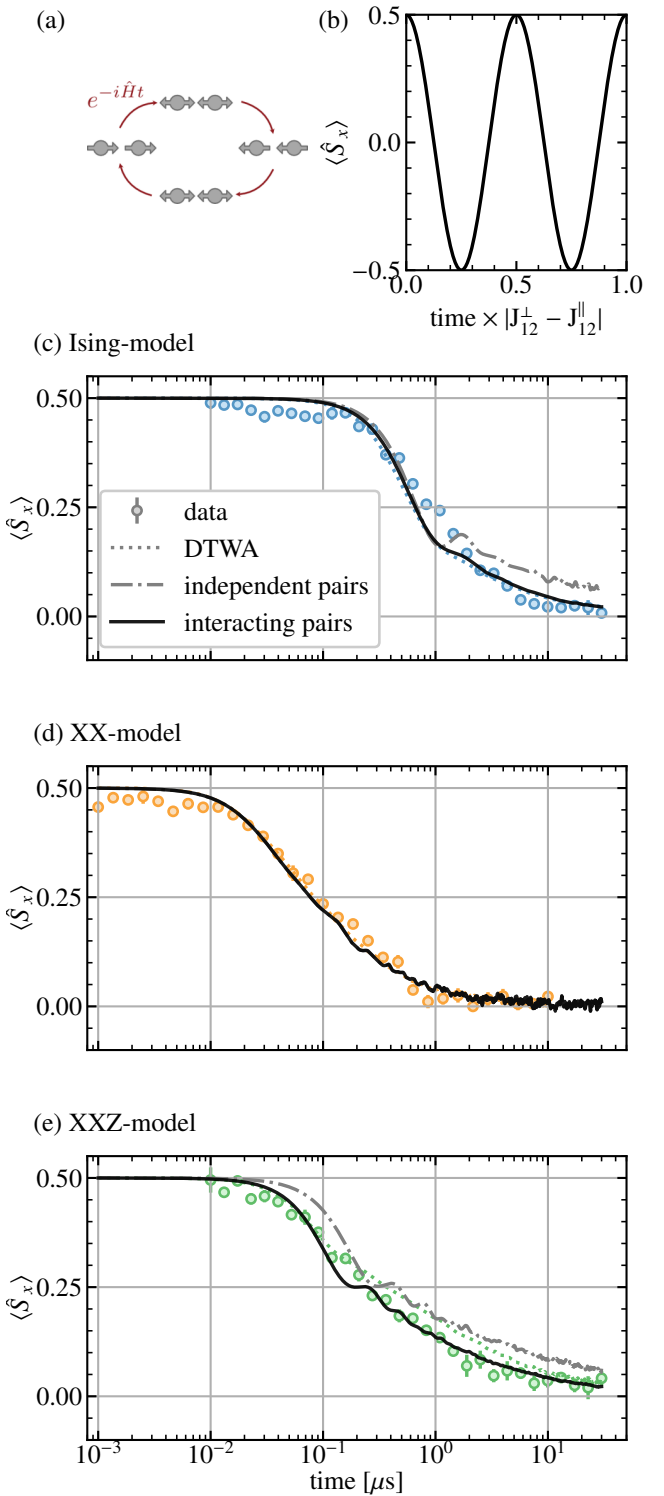


FIG. 3. Effective description by localized pairs. (a) Illustration of the oscillation of a single pair under an arbitrary XXZ Hamiltonian. A fully polarized state $| \rightarrow \rightarrow \rangle$ (left) evolves via the maximally entangled Bell state $1/\sqrt{2}(| \rightarrow \rightarrow \rangle + | \leftarrow \leftarrow \rangle)$ (top) to the state $| \leftarrow \leftarrow \rangle$ (right). Then, it returns to the origin via the other Bell state $1/\sqrt{2}(| \rightarrow \rightarrow \rangle - | \leftarrow \leftarrow \rangle)$ (bottom). (b) Oscillation of the magnetization for a single pair initialized in $| \rightarrow \rightarrow \rangle$. (c-e) Comparison of the relaxation dynamics obtained by the pair approximation with/without effective Ising terms (solid black line/grey dash-dotted line) and with DTWA (dotted line) and the experimental data of Fig. 2 for Ising (c), XX (d) and XXZ model (e).

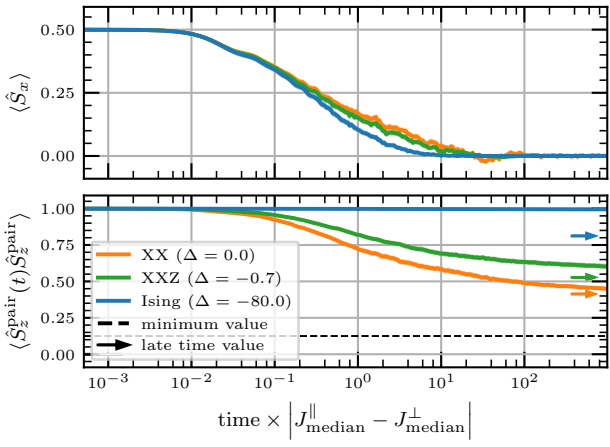


FIG. 4. Pair magnetization autocorrelator and prethermalization. Numerical simulation of $N = 16$ spins in $d = 1$ with interaction exponent $a = 2$ and a mean inter-spin distance $a_0 = 20r_b$. Line width shows statistical uncertainty from disorder averaging.

two timescales. Observing two distinct timescales shows that the system has not yet reached thermal equilibrium once the magnetization has relaxed to zero [17, 22] but rather hints at prethermal behavior [12, 14, 16, 49] with a prethermal Hamiltonian that contains mostly Ising-like interactions among pairs. Finally, even in the infinite time limit (derived by the diagonal ensemble and indicated by arrows in FIG. 4), the pair autocorrelator remains at $\approx 1/2$ which is significantly above the lower limit of $\frac{2}{N} = 1/8$. This indicates that even at late times our integrable pair model is still a good description of the system.

VI. CONCLUSION

Our work demonstrates the ability of Rydberg atom quantum simulators to synthesize a variety of many-body Hamiltonians on a single experimental platform. By choosing the appropriate state combination, we realized XX-, XXZ-, and for the first time, a quantum Ising model within the Rydberg manifold. This versatility of the platform has enabled us to directly study and compare the relaxation dynamics of three different quantum spin systems far-from-equilibrium.

We have observed universal relaxation dynamics, i.e. dynamics independent of the microscopic details of the system after appropriate rescaling and we provide an explanation by considering an effective description of the system in terms of pairs of spins which we expect to be a good approximation on intermediate timescales. This effective description is integrable and allows for an analytical derivation of the polarization dynamics. We argue, that the universal behavior can be understood based on this effective model and thus is rooted in the emergent

integrability of the system at early times.

A natural follow-up question is to ask whether this universal behavior is generically observed. It is already known that universality holds only in a strong disorder regime [21]. We added an experimental investigation of the influence of the initial states in appendix E which confirms the universality of the dynamics. Exact numerical simulations show that higher-order correlators like the pair-autocorrelator do not feature the same universal dynamics. Experiments possessing single-site resolution and control over disorder can access this quantity and investigate the deviations from the pair model and hence from the prethermal state [50]. Further investigations could also study the influence of the energy density of the initial state on the dynamics, indicative of a possible phase transition [51].

The accurate approximation of the relaxation dynamics by an integrable model of pairs signifies a paradigm shift, indicating that the time evolution of disordered quantum spin systems cannot be purely regarded as thermalization dynamics. Instead, even at later times when the magnetization has completely relaxed to zero, the system exhibits characteristics reminiscent of local pairs of spins. We interpret this behavior as prethermalization. However, it remains an open question as to how the effective integrability of the system is broken and whether the system relaxes towards thermal states in the thermodynamic limit.

ACKNOWLEDGMENTS

We thank Andre Salzinger and Annika Tebben for important contributions to maintaining the experimental apparatus. Furthermore, we thank Hengyun Zhou, Nathan Leitao, and Leigh Martin for helpful discussions. This work is part of and supported by the Deutsche Forschungsgemeinschaft (DFG, German Research Foundation) under Germany's Excellence Strategy EXC2181/1-390900948 (the Heidelberg STRUCTURES Excellence Cluster), within the Collaborative Research Centre "SFB 1225 (ISOQUANT)," the DFG Priority Program "GiRyd 1929," the European Union H2020 projects FET Proactive project RySQ (Grant No. 640378), and FET flagship project PASQuanS (Grant No. 817482), and the Heidelberg Center for Quantum Dynamics. The authors acknowledge support by the state of Baden-Württemberg through bwHPC and the German Research Foundation (DFG) through grant no INST 40/575-1 FUGG (JUSTUS 2 cluster) and used the Julia programming language for most of the numerics [52]. T. F. acknowledges funding by a graduate scholarship of the Heidelberg University (LGFG).

Appendix A: Engineering Heisenberg XXZ Hamiltonians by different combinations of Rydberg states

In the following, we provide a comprehensive description of how to engineer this Hamiltonian with different combinations of Rydberg states [40, 41]. Especially, this gives us the opportunity to explain how to engineer an Ising Hamiltonian in a spin system realized by two different Rydberg states.

For general spin systems with global $U(1)$ symmetry, the coupling terms can be obtained by calculating the matrix elements of the interaction Hamiltonian \hat{H} . The Ising term

$$J_{ij}^{\parallel} = (E_{\uparrow_i \uparrow_j} + E_{\downarrow_i \downarrow_j}) - (E_{\downarrow_i \uparrow_j} + E_{\uparrow_i \downarrow_j}) \quad (\text{A1})$$

is defined as the energy difference between spins being aligned and being anti-aligned. Here, $E_{\alpha_i \beta_j} = \langle \alpha_i \beta_j | \hat{H} | \alpha_i \beta_j \rangle$ are the interaction energy of spin i and j with $\alpha, \beta \in [\uparrow, \downarrow]$. The exchange term is determined by

$$J_{ij}^{\perp} = \langle \downarrow_i \uparrow_j | \hat{H} | \uparrow_i \downarrow_j \rangle. \quad (\text{A2})$$

For a system consisting of states with opposite parity, such as $|\downarrow\rangle = |nS\rangle$ and $|\uparrow\rangle = |nP\rangle$ (see Fig. 1 (b)), where n is the principal quantum number, the dominant coupling is a direct dipolar interaction which can be described by the Hamiltonian

$$\hat{H}_{\text{DDI}} = \frac{\hat{\mathbf{d}}_i \cdot \hat{\mathbf{d}}_j - 3(\hat{\mathbf{d}}_i \cdot \mathbf{e}_{r_{ij}})(\hat{\mathbf{d}}_j \cdot \mathbf{e}_{r_{ij}})}{r_{ij}^3}. \quad (\text{A3})$$

where $\hat{\mathbf{d}}_i$ is the dipole operator of atom i , $\mathbf{e}_{r_{ij}}$ is the unit vector connecting the two atoms and r_{ij} their distance. Mapped Eq. A3 on the spin Hamiltonian of Eq. 1, the resulting interaction coefficient is

$$J_{ij}^{\perp} = \frac{C_3^{\perp}(1 - 3\cos^2\theta_{ij})}{r_{ij}^3}. \quad (\text{A4})$$

Here, θ_{ij} is the angle between $\mathbf{e}_{r_{ij}}$ and the quantization axis and C_3^{\perp} the coupling parameter [36, 37]. The Ising term J_{ij}^{\parallel} is zero since interaction energy shifts $E_{\alpha_i \beta_j}$ are dipole forbidden. Therefore, this is a way to realize an XX model as depicted in Fig. 1 b). In this work, we have chosen $|61S\rangle$ and $|61P\rangle$ leading to $C_3^{\perp}/2\pi = 3.14 \text{ GHz } \mu\text{m}^3$.

In the case where the two chosen states possess the same parity, such as the two atoms being in the same state $|nS\rangle$, direct dipolar coupling is forbidden and the leading interaction is a second-order process through a virtually excited pair state $|m\rangle$ and can be described by

$$\hat{H}_{vdW} = -\frac{1}{\hbar} \sum_m \frac{\hat{H}_{\text{DDI}} |m\rangle \langle m| \hat{H}_{\text{DDI}}}{\Delta_{\nu}}. \quad (\text{A5})$$

Here, the Foerster defect Δ_{ν} is the energy difference between the initial state and the virtually excited state $|m\rangle$. This Hamiltonian gives rise to power-law interactions $J_{ij} = C_6/r_{ij}^6$ that scales with n^{11} . Especially, this term is large if a pair state $|m\rangle$ with a small Foerster defect exists. Many experiments exploit these interactions to realize a spin system where the ground state is coupled to a single Rydberg state. These systems feature the Rydberg blockade effect and can be mapped on an Ising model [3, 34, 35].

Similar interactions also exist for a spin system realized with two different Rydberg states $|\downarrow\rangle = |nS\rangle$ and $|\uparrow\rangle = |(n+1)S\rangle$. In this case, the Van-der-Waals Hamiltonian (A5) also induces a spin exchange term because the two Rydberg states are coupled via the intermediate pair state $|m\rangle = |nP, nP\rangle$ (see Fig. 1 (c)). In the case of $n = 61$, both the Ising and exchange interactions terms are similar with $J^{\parallel}/J^{\perp} = -0.7$. Therefore, this spin system can be mapped onto an effective Heisenberg XXZ-Hamiltonian [21].

In order to realize an Ising Hamiltonian with two different Rydberg states, a state combination is needed where the exchange term (A2) is small requiring a large Foerster defect Δ_{ν} (see Fig. 1 (d)). This can be achieved by coupling $|\downarrow\rangle = |nS\rangle$ to $|\uparrow\rangle = |(n+3)S\rangle$. In this case, the largest contribution to the exchange term comes from $|m\rangle = |(n+1)P, (n+1)P\rangle$. For example, for $n = 61$, this spin system is characterized by a ratio of $J^{\parallel}/J^{\perp} = 400$, which is a good approximation to an Ising Hamiltonian ($J^{\perp} = 0$).

Appendix B: Experimental implementation of various spin models

To realize the Heisenberg-XX model, a single-photon microwave transition at $2\pi \cdot 16 \text{ GHz}$ with a Rabi frequency of $\Omega = 2\pi \cdot 18 \text{ MHz}$ couples the state $|\downarrow\rangle$ to $|\uparrow\rangle = |61P_{3/2}, m_j = 1/2\rangle$. To implement the XXZ Hamiltonian, two microwave photons at $2\pi \cdot 16 \text{ GHz}$ couple to $|\uparrow\rangle = |62S_{1/2}, m_j = 1/2\rangle$. Here, a single photon Rabi frequency of $\Omega = 2\pi \cdot 48 \text{ MHz}$ with a detuning $\Delta_{\nu} = 2\pi \cdot 170 \text{ MHz}$ leads to a two-photon Rabi frequency of $\Omega_{2\gamma} = 2\pi \cdot 6.8 \text{ MHz}$. To realize the Ising model, the state $|61S\rangle$ has to be coupled to $|64S_{1/2}, m_j = 0.5\rangle$ but the detuning of $\Delta_{\nu} = 2\pi \cdot 1.426 \text{ GHz}$ is too large and prevents an efficient coupling of the states with two microwave photons of the same frequency $2\pi \cdot 47 \text{ GHz}$. Therefore, we combine two frequencies differing by $2\pi \cdot 1.563 \text{ GHz}$ such that the effective detuning to the intermediate state $|62P\rangle$ is $2\pi \cdot 136 \text{ MHz}$. For a single photon Rabi frequency of $\Omega = 2\pi \cdot 30 \text{ MHz}$ this results in an effective two-photon Rabi frequency of $\Omega_{2\gamma} = 2\pi \cdot 3.3 \text{ MHz}$ (see Fig. 1 (b-d) for the microwave photonic transitions).

Model	blue exc. $\sigma_{x,y}$	red exc. $\sigma_{x,y}$	GS σ_x	GS $\sigma_{y,z}$
Ising	55 μm	1.5 mm	64 μm	45 μm
XXZ	55 μm	1.5 mm	64 μm	45 μm
XX	55 μm	1.5 mm	62 μm	47 μm

TABLE I. Waists of the blue (480 nm) and red (780 nm) Rydberg excitation lasers used to realize the different models and the respective ground state cloud waists.

Appendix C: Distribution of interaction time scales in the spin system

In the main text, we have highlighted that the typical timescale of the relaxation is given by the pair oscillation frequency $|J_{\parallel} - J_{\perp}|$. For the Heisenberg XXZ Hamiltonian, both exchange and Ising interactions exist. Therefore, another possibility of rescaling would only involve J_{\perp} which would disregard the anisotropy $\delta = J_{\parallel}/J_{\perp}$. In Fig. 5, we have compared both possibilities of rescaling time. The rescaling by the oscillation frequency shows a more precise collapse of the experimental data. This demonstrates that this frequency indeed determines the relevant timescale of the system. In addition, this indicates that the Rydberg interactions can be mapped onto the Heisenberg XXZ Hamiltonian with $\delta = -0.7$.

In Fig. 6, we show the sensitivity of the DTWA simulations to different densities and blockade radii. For most simulations, these parameters have only a small, quantitative effect on the simulated dynamics. A notable exception is the Ising system. Here, the Rydberg cloud is largely saturated and the blockade radius is the relevant length scale of the system. Therefore, a variation of the blockade radius changes drastically the early time dynamics. In contrast, the density of the sample featuring XX-interaction is low, therefore the blockade effect can be neglected. For the Heisenberg XXZ Hamiltonian, the simulations show that the blockade radius of 8.3 μm fits the observed dynamics slightly better than the value of 10 μm expected from the simplified excitation model assuming no phase noise of the laser.

Appendix D: Influence of the Gaussian trap geometry on the relaxation dynamics

The functional form of the relaxation dynamics in a strongly disordered spin system has been demonstrated to be independent of both the Rydberg blockade radius and the anisotropy of the Heisenberg XXZ Hamiltonian. However, the timescale of these dynamics is contingent upon the density and coupling constant. Consequently, there arises the necessity to rescale time by the median interaction strength median_j max_i J_{ij} .

In the context of a Gaussian trap geometry, we conduct an averaging procedure over varying local densities ρ . Assuming local density approximation, we average over different local relaxation dynamics, each char-

acterized by a stretched exponential function, sharing a common stretching exponent β , while exhibiting distinct timescales $\tau(\rho)$. The collective summation of these relaxation curves again manifests as a stretched exponential decay. However, the details of the stretching exponent β depend on the shape of the Gaussian cloud.

Furthermore, finite-size effects come into play, with one-dimensional physics becoming relevant in an elongated cigar-shaped geometry and two-dimensional physics in a flat pancake geometry. Consequently, the measured stretched exponential does not align with the expected value of $\beta = d/\alpha$ (where d represents the dimension and α signifies the range of interactions) as anticipated from semiclassical simulations [28]. Instead, the observed value interpolates between various dimensions and exhibits slight variations in different experimental realizations when the trap geometry is altered.

Nevertheless, through a comparative analysis of experiments conducted in similar geometries, it remains feasible to investigate whether the dynamics are contingent upon the size of the blockade radius [21] or the anisotropy parameter Δ of the Heisenberg XXZ Hamiltonian (as explored in this study).

Appendix E: Relaxation under initial states with different magnetization

In order to test if the universal relaxation behavior, originating from a pair picture approximation is even consistent for the relaxation of more general states than the fully x-polarized state, we probe the relaxation for initial states with different magnetization. The experimental protocol is shown in Fig. 8a and is similar to the one used in [53]. It consists of the following steps. In the preparation, spins are initially polarized along the x-axis. A locking field Ω_{Lock} which is also aligned along the x-axis is applied for a time t_1 . During this time, as reported in [53], the magnetization will relax and approximately settle to a constant non-zero value that depends on the strength of the locking field. In the evolution, we then turn off the locking field and measure the resulting relaxation of the x-magnetization. The resulting relaxation over period t_2 is shown in Fig. 8b. The magnetization starts with different values depending on the field strength applied during the preparation. We note that the locking time $t_2 = 2\mu s$ is larger than the time it takes to directly relax to zero magnetization without phase one (blue points). We observed that for decreasing initial magnetization, the onset of the relaxation dynamics gets shifted to a later time (red, green, and yellow points). However, independent of this behavior, for later times, all curves overlap with the direct relaxation curve without field (blue points).

The observed dynamics can be understood within the pair approximation in the following way. During preparation, the locking field is only able to lock pairs with interactions smaller than the field strength Ω_{Lock} . These

pairs stay polarized while pairs with stronger interactions oscillate and dephase. As reported in [53], magnetization takes an almost constant value. During the evolution, when the field is turned off, the relaxation timescale is given by the remaining pairs that were locked and now start to oscillate. This timescale is longer for small fields where only weakly interacting pairs remained locked during the preparation. The overlapping at a later time is due to the fact that these pairs are also locked under larger fields. The data was take for $|48S_{1/2}, m_j = 0.5\rangle$ and $|48P_{3/2}, m_j = 0.5\rangle$.

Appendix F: Derivation of depolarization dynamics

The goal is to compute the expectation value of $\langle \hat{S}_x(t) \rangle = \frac{1}{N} \sum_i \langle \hat{s}_x^i \rangle$ starting from the x -polarized state

$|\psi_0\rangle = |\rightarrow\rangle^{\otimes N}$ governed by the effective Hamiltonian derived in [48]

$$\begin{aligned} \hat{H}_{eff} = & \sum_{\langle i,j \rangle} \left(J_{ij}^\perp (\hat{s}_x^i \hat{s}_x^j + \hat{s}_y^i \hat{s}_y^j) + J_{ij}^\parallel \hat{s}_z^i \hat{s}_z^j \right) . \\ & + \sum_{\langle i,j \rangle, \langle k,l \rangle} J_{eff}^{ijkl} \hat{s}_z^{(i)(j)} \hat{s}_z^{(k)(l)} \end{aligned} \quad (F1)$$

where $\langle i,j \rangle$ denotes the summation over paired spins i and j and $2\hat{s}_z^{(i)(j)} = \hat{s}_z^{(i)} + \hat{s}_z^{(j)}$.

Without loss of generality, we assume that spins 1 and 2 form a pair and compute $\langle \hat{s}_x^1(t) \rangle$. The evolution of $\langle \hat{S}_x(t) \rangle$ then follows simply by linearity. First we notice that all the terms in \hat{H}_{eff} commute with each other, allowing for direct computation of $\langle \hat{s}_x^1(t) \rangle$ by commuting \hat{s}_x^1 through the time evolution operators:

$$\hat{s}_x^1(t) = e^{it\hat{H}_{eff}} \hat{s}_x^1 e^{-it\hat{H}_{eff}} \quad (F2)$$

$$= e^{itJ_{12}^\perp (\hat{s}_x^1 \hat{s}_x^2 + \hat{s}_y^1 \hat{s}_y^2)} e^{it\hat{s}_z^{(1)(2)} \sum_{\langle k,l \rangle} J_{eff}^{12kl} \hat{s}_z^{(k)(l)}} \hat{s}_x^1 e^{-it\hat{s}_z^{(1)(2)} \sum_{\langle k,l \rangle} J_{eff}^{12kl} \hat{s}_z^{(k)(l)}} e^{-itJ_{12}^\perp (\hat{s}_x^1 \hat{s}_x^2 + \hat{s}_y^1 \hat{s}_y^2)} \quad (F3)$$

$$= e^{itJ_{12}^\perp (\hat{s}_x^1 \hat{s}_x^2 + \hat{s}_y^1 \hat{s}_y^2)} e^{it\hat{s}_z^1 \sum_{\langle k,l \rangle} J_{eff}^{12kl} \hat{s}_z^{(k)(l)}} e^{-itJ_{12}^\perp (\hat{s}_x^1 \hat{s}_x^2 - \hat{s}_y^1 \hat{s}_y^2)} \hat{s}_x^1 \quad (F4)$$

Now we can just expand the exponentials using the usual formula for the exponential of Pauli matrices (note that $\hat{s}_x^1 \hat{s}_x^2 + \hat{s}_y^1 \hat{s}_y^2$ is akin to \hat{s}_x in a specific subspace) and take the expectation value with respect to the initial state to get the desired result:

$$\langle \hat{s}_x^1(t) \rangle = \frac{1}{2} \cos \left(\frac{J_{12}^\perp}{2} t \right) \prod_{\langle k,l \rangle} \cos^2 \left(\frac{J_{eff}^{12kl}}{8} t \right) \quad (F5)$$

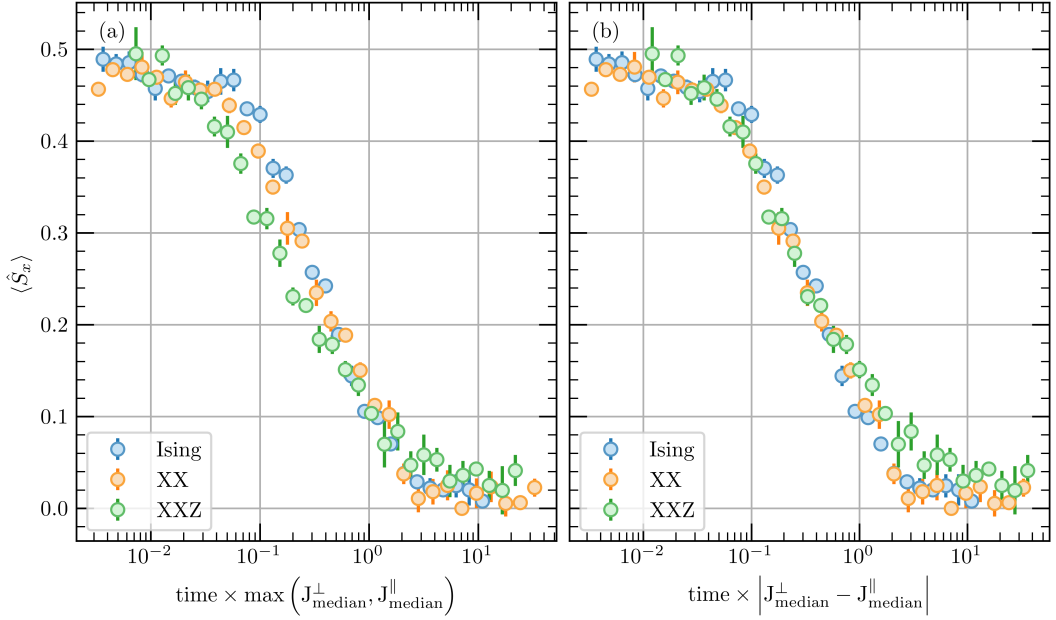


FIG. 5. Comparison of the scaling behavior for rescaling time either by the median interaction matrix (a) or by the median of the pair oscillation frequency (b). $\max(J_{\text{median}}^{\perp}, J_{\text{median}}^{\parallel})$ is defined as $J_{\text{median}}^{\perp}$ for the Heisenberg XX and XXZ model, and as $J_{\text{median}}^{\perp}$ for the Ising model.

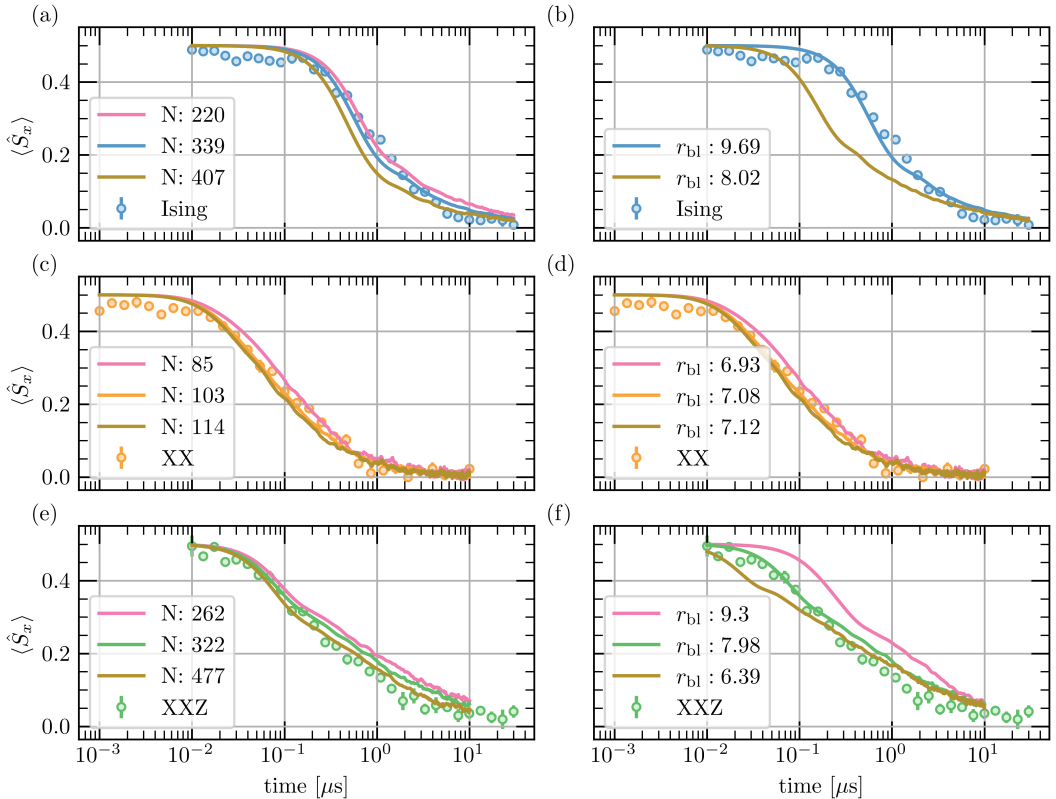


FIG. 6. Influence of the density and the blockade radius on the DTWA simulations. Left column: Simulations for the same blockade radius as in the main text for different particle numbers N . Right column: Simulations for the same particle number and various blockade radii. In all simulations the geometry of the cloud is the same.

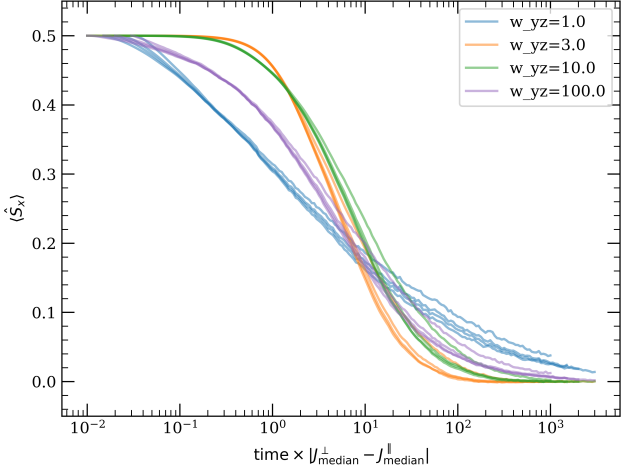


FIG. 7. MACE simulations of the relaxation of the magnetization for four different geometries of the Gaussian cloud where the aspect ratio of the waist w_x in x direction with respect to the waist w_{yz} in y and z direction is tuned. The product $w_x \times w_{yz}^2$ is fixed for all 4 geometries. For each geometry, we simulate the time evolution for different anisotropies $\frac{J^\parallel}{J^\perp} \in \{-2, -0.5, 0, 0.5, 2\}$.

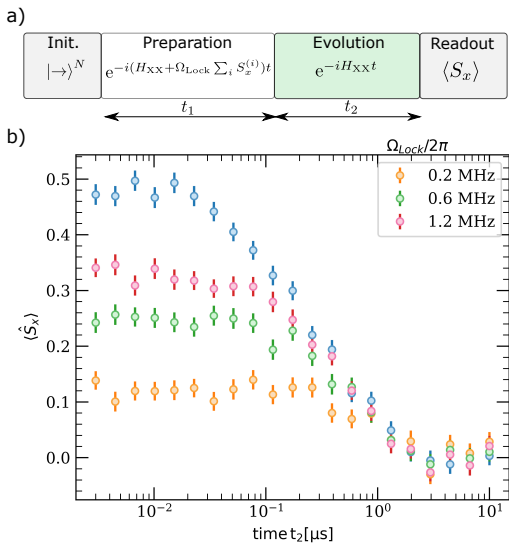


FIG. 8. Relaxation dynamics of initial states with different magnetization. a) Experimental sequence consisting of an evolution under a spin locking field (preparation), followed by a measurement of the magnetization for the resulting relaxation dynamics for t_2 (evolution). b) Magnetization dynamics after different $\Omega_{Lock}/2\pi$ applied in phase one.

-
- [1] M. Heyl, A. Polkovnikov, and S. Kehrein, Dynamical Quantum Phase Transitions in the Transverse-Field Ising Model, *Physical Review Letters* **110**, 135704 (2013).
- [2] J. Zhang, G. Pagano, P. W. Hess, A. Kyprianidis, P. Becker, H. Kaplan, A. V. Gorshkov, Z.-X. Gong, and C. Monroe, Observation of a many-body dynamical phase transition with a 53-qubit quantum simulator, *Nature* **551**, 601 (2017).
- [3] H. Bernien, S. Schwartz, A. Keesling, H. Levine, A. Omran, H. Pichler, S. Choi, A. S. Zibrov, M. Endres, M. Greiner, V. Vuletić, and M. D. Lukin, Probing many-body dynamics on a 51-atom quantum simulator, *Nature* **551**, 579 (2017).
- [4] M. Serbyn, D. A. Abanin, and Z. Papić, Quantum many-body scars and weak breaking of ergodicity, *Nature Physics* **17**, 675 (2021).
- [5] D. Bluvstein, H. Levine, G. Semeghini, T. T. Wang, S. Ebadi, M. Kalinowski, A. Keesling, N. Maskara, H. Pichler, M. Greiner, V. Vuletić, and M. D. Lukin, A quantum processor based on coherent transport of entangled atom arrays, *Nature* **604**, 451 (2022).
- [6] D. A. Abanin, E. Altman, I. Bloch, and M. Serbyn, *Colloquium* : Many-body localization, thermalization, and entanglement, *Reviews of Modern Physics* **91**, 021001 (2019).
- [7] J. Smith, A. Lee, P. Richerme, B. Neyenhuis, P. W. Hess, P. Hauke, M. Heyl, D. A. Huse, and C. Monroe, Many-body localization in a quantum simulator with programmable random disorder, *Nature Physics* **12**, 907 (2016).
- [8] M. Schreiber, S. S. Hodgman, P. Bordia, H. P. Lüschen, M. H. Fischer, R. Vosk, E. Altman, U. Schneider, and I. Bloch, Observation of many-body localization of interacting fermions in a quasirandom optical lattice, *Science* **349**, 842 (2015).
- [9] A. Lukin, M. Rispoli, R. Schittko, M. E. Tai, A. M. Kaufman, S. Choi, V. Khemani, J. Léonard, and M. Greiner, Probing entanglement in a many-body-localized system, *Science* **364**, 256 (2019).
- [10] J.-y. Choi, S. Hild, J. Zeiher, P. Schauß, A. Rubio-Abadal, T. Yefsah, V. Khemani, D. A. Huse, I. Bloch, and C. Gross, Exploring the many-body localization transition in two dimensions, *Science* **352**, 1547 (2016).
- [11] A. Polkovnikov, K. Sengupta, A. Silva, and M. Vengalattore, *Colloquium* : Nonequilibrium dynamics of closed interacting quantum systems, *Reviews of Modern Physics* **83**, 863 (2011).
- [12] M. Ueda, Quantum equilibration, thermalization and prethermalization in ultracold atoms, *Nature Reviews Physics* **2**, 669 (2020).
- [13] P. Peng, C. Yin, X. Huang, C. Ramanathan, and P. Capellaro, Floquet prethermalization in dipolar spin chains, *Nature Physics* **17**, 444 (2021).
- [14] M. Prüfer, P. Kunkel, H. Strobel, S. Lannig, D. Linemann, C.-M. Schmied, J. Berges, T. Gasenzer, and M. K. Oberthaler, Observation of universal dynamics in a spinor Bose gas far from equilibrium, *Nature* **563**, 217 (2018).
- [15] A. Rubio-Abadal, M. Ippoliti, S. Hollerith, D. Wei, J. Rui, S. Sondhi, V. Khemani, C. Gross, and I. Bloch, Floquet Prethermalization in a Bose-Hubbard System, *Physical Review X* **10**, 021044 (2020).
- [16] C. Eigen, J. A. P. Glidden, R. Lopes, E. A. Cornell, R. P. Smith, and Z. Hadzibabic, Universal prethermal dynamics of Bose gases quenched to unitarity, *Nature* **563**, 221 (2018).
- [17] L. S. Martin, H. Zhou, N. T. Leitao, N. Maskara, O. Makarova, H. Gao, Q.-Z. Zhu, M. Park, M. Tyler, H. Park, S. Choi, and M. D. Lukin, Controlling local thermalization dynamics in a Floquet-engineered dipolar ensemble (2022), arXiv:2209.09297 [cond-mat, physics:quant-ph].
- [18] G. Benettin, R. Livi, and G. Parisi, Ergodicity: How Can It Be Broken?, *Large Deviations in Physics* , 29 (2014).
- [19] M. Bernaschi, A. Billoire, A. Maiorano, G. Parisi, and F. Ricci-Tersenghi, Strong ergodicity breaking in aging of mean-field spin glasses, *Proceedings of the National Academy of Sciences* **117**, 17522 (2020).
- [20] S. A. Parameswaran, A. C. Potter, and R. Vasseur, Eigenstate phase transitions and the emergence of universal dynamics in highly excited states, *Annalen der Physik* **529**, 1600302 (2017).
- [21] A. Signoles, T. Franz, R. Ferracini Alves, M. Gärttner, S. Whitlock, G. Zürn, and M. Weidmüller, Glassy Dynamics in a Disordered Heisenberg Quantum Spin System, *Physical Review X* **11**, 011011 (2021).
- [22] J. Choi, S. Choi, G. Kucsko, P. C. Maurer, B. J. Shields, H. Sumiya, S. Onoda, J. Isoya, E. Demler, F. Jelezko, N. Y. Yao, and M. D. Lukin, Depolarization Dynamics in a Strongly Interacting Solid-State Spin Ensemble, *Physical Review Letters* **118**, 093601 (2017).
- [23] G. Kucsko, S. Choi, J. Choi, P. Maurer, H. Zhou, R. Landig, H. Sumiya, S. Onoda, J. Isoya, F. Jelezko, E. Demler, N. Yao, and M. Lukin, Critical Thermalization of a Disordered Dipolar Spin System in Diamond, *Physical Review Letters* **121**, 023601 (2018).
- [24] C. Sommer, G. Pupillo, N. Takei, S. Takeda, A. Tanaka, K. Ohmori, and C. Genes, Time-domain Ramsey interferometry with interacting Rydberg atoms, *Physical Review A* **94**, 053607 (2016).
- [25] N. Takei, C. Sommer, C. Genes, G. Pupillo, H. Goto, K. Koyasu, H. Chiba, M. Weidmüller, and K. Ohmori, Direct observation of ultrafast many-body electron dynamics in an ultracold Rydberg gas, *Nature Communications* **7**, 13449 (2016).
- [26] J. Klafter and M. F. Shlesinger, On the relationship among three theories of relaxation in disordered systems, *Proceedings of the National Academy of Sciences* **83**, 848 (1986).
- [27] P. Schultzen, T. Franz, S. Geier, A. Salzinger, A. Tebben, C. Hainaut, G. Zürn, M. Weidmüller, and M. Gärttner, Glassy quantum dynamics of disordered Ising spins, *Physical Review B* **105**, L020201 (2022).
- [28] P. Schultzen, T. Franz, C. Hainaut, S. Geier, A. Salzinger, A. Tebben, G. Zürn, M. Gärttner, and M. Weidmüller, Semiclassical simulations predict glassy dynamics for disordered Heisenberg models, *Physical Review B* **105**, L100201 (2022).
- [29] I. Bloch, J. Dalibard, and W. Zwerger, Many-body physics with ultracold gases, *Reviews of Modern Physics* **80**, 885 (2008).
- [30] R. Blatt and C. F. Roos, Quantum simulations with

- trapped ions, *Nature Physics* **8**, 277 (2012).
- [31] I. M. Georgescu, S. Ashhab, and F. Nori, Quantum simulation, *Reviews of Modern Physics* **86**, 153 (2014).
 - [32] C. Gross and I. Bloch, Quantum simulations with ultracold atoms in optical lattices, *Science* **357**, 995 (2017).
 - [33] A. Browaeys and T. Lahaye, Many-body physics with individually controlled Rydberg atoms, *Nature Physics* **16**, 132 (2020).
 - [34] D. Jaksch, J. I. Cirac, P. Zoller, S. L. Rolston, R. Côté, and M. D. Lukin, Fast Quantum Gates for Neutral Atoms, *Physical Review Letters* **85**, 2208 (2000).
 - [35] H. Weimer, M. Müller, I. Lesanovsky, P. Zoller, and H. P. Büchler, A Rydberg quantum simulator, *Nature Physics* **6**, 382 (2010).
 - [36] D. Barredo, H. Labuhn, S. Ravets, T. Lahaye, A. Browaeys, and C. S. Adams, Coherent Excitation Transfer in a Spin Chain of Three Rydberg Atoms, *Physical Review Letters* **114**, 113002 (2015).
 - [37] A. P. Orioli, A. Signoles, H. Wildhagen, G. Günter, J. Berges, S. Whitlock, and M. Weidemüller, Relaxation of an Isolated Dipolar-Interacting Rydberg Quantum Spin System, *Physical Review Letters* **120**, 063601 (2018).
 - [38] K. Slagle, Y. Z. You, and C. Xu, Disordered XYZ spin chain simulations using the spectrum bifurcation renormalization group, *Physical Review B* **94**, 014205 (2016).
 - [39] v. Bijnen, R.M.W., *Quantum Engineering with Ultracold Atoms*, Phd Thesis 1 (Research TU/e / Graduation TU/e), Technische Universiteit Eindhoven, Eindhoven (2013).
 - [40] S. Whitlock, A. W. Glaetzle, and P. Hannaford, Simulating quantum spin models using Rydberg-excited atomic ensembles in magnetic microtrap arrays, *Journal of Physics B: Atomic, Molecular and Optical Physics* **50**, 074001 (2017).
 - [41] M. D. Lukin, M. Fleischhauer, R. Cote, L. M. Duan, D. Jaksch, J. I. Cirac, and P. Zoller, Dipole Blockade and Quantum Information Processing in Mesoscopic Atomic Ensembles, *Physical Review Letters* **87**, 037901 (2001).
 - [42] J. Schachenmayer, A. Pikovski, and A. M. Rey, Many-Body Quantum Spin Dynamics with Monte Carlo Trajectories on a Discrete Phase Space, *Physical Review X* **5**, 011022 (2015).
 - [43] R. Vosk and E. Altman, Many-Body Localization in One Dimension as a Dynamical Renormalization Group Fixed Point, *Physical Review Letters* **110**, 067204 (2013).
 - [44] D. Pekker, G. Refael, E. Altman, E. Demler, and V. Oganesyan, Hilbert-Glass Transition: New Universality of Temperature-Tuned Many-Body Dynamical Quantum Criticality, *Physical Review X* **4**, 011052 (2014).
 - [45] R. Vasseur, A. C. Potter, and S. A. Parameswaran, Quantum Criticality of Hot Random Spin Chains, *Physical Review Letters* **114**, 217201 (2015).
 - [46] R. Vasseur, A. J. Friedman, S. A. Parameswaran, and A. C. Potter, Particle-hole symmetry, many-body localization, and topological edge modes, *Physical Review B* **93**, 134207 (2016).
 - [47] P. Scholl, H. J. Williams, G. Bornet, F. Wallner, D. Barredo, L. Henriet, A. Signoles, C. Hainaut, T. Franz, S. Geier, A. Tebben, A. Salzinger, G. Zürn, T. Lahaye, M. Weidemüller, and A. Browaeys, Microwave Engineering of Programmable \$XXZ\$ Hamiltonians in Arrays of Rydberg Atoms, *PRX Quantum* **3**, 020303 (2022).
 - [48] A. Braemer, T. Franz, M. Weidemüller, and M. Gärttner, Pair localization in dipolar systems with tunable positional disorder, *Physical Review B* **106**, 134212 (2022).
 - [49] T. Langen, T. Gasenzer, and J. Schmiedmayer, Prethermalization and universal dynamics in near-integrable quantum systems, *Journal of Statistical Mechanics: Theory and Experiment* **2016**, 064009 (2016).
 - [50] L. Christakis, J. S. Rosenberg, R. Raj, S. Chi, A. Morningstar, D. A. Huse, Z. Z. Yan, and W. S. Bakr, Probing site-resolved correlations in a spin system of ultracold molecules, *Nature* **614**, 64 (2023).
 - [51] L. Rademaker and D. A. Abanin, Slow Nonthermalizing Dynamics in a Quantum Spin Glass, *Physical Review Letters* **125**, 260405 (2020).
 - [52] J. Bezanson, A. Edelman, S. Karpinski, and V. B. Shah, Julia: A Fresh Approach to Numerical Computing, *SIAM Review* **59**, 65 (2017).
 - [53] T. Franz, S. Geier, C. Hainaut, A. Signoles, N. Thaicharoen, A. Tebben, A. Salzinger, A. Braemer, M. Gärttner, G. Zürn, and M. Weidemüller, Absence of thermalization in an interacting system of thousands of quantum spins 10.48550/ARXIV.2207.14216 (2022).

6.2 EMERGENT PAIR LOCALIZATION

Another way of validating the pair model is the comparison of the same system subject different disorder strength. This can be realized in a Rydberg based quantum simulator by tuning the systems density as explained in the background chapter.

In the work below, we again use the x -magnetization as observable and track its steady-state value with respect to an external magnetic field aligned in x -direction as well. We find a clear qualitative difference at weak external field where the strongly disordered system responds much stronger to the field, i.e. the steady-state magnetization grows very fast with increasing field strength. This leads to a sharp cusp-like curve, which we show to be incompatible with a thermal state. However, we find that a pair-based effective model reproduces this feature and can also match the full measurement data closely. In contrast, for weak disorder, i.e. high density, the behavior of the steady-state magnetization is much different. At weak field, the curve is very round which is reproduced nicely by assuming a thermal state.

Thus, this experiment provides direct evidence for a pair localization transition at least at experimentally relevant timescales. However, it is possible that this is a prethermal regime only and that this signature vanishes at much later times. Testing for this experimentally will of course be very hard if not impossible at all depending on the timescale this final relaxation occurs.

After the publication (cf. Section 6.2.1), we additionally present a simplified model that allows for analytical computation of both the thermal and pair localized magnetization curves. While this model is not as quantitative as the model contained in the paper, it nonetheless reproduces the curves qualitatively and highlights the physical origin of the behavior at weak field more clearly.

Emergent pair localization in a many-body quantum spin system

Titus Franz,^{1,2,*} Sebastian Geier,¹ Adrian Braemer,^{1,3} Clément Hainaut,^{1,4}
 Adrien Signoles,^{1,5} Nithiwadee Thaicharoen,^{1,6} Annika Tebben,¹ Andre Salzinger,¹
 Martin Gärttner,^{1,3,7,8,†} Gerhard Zürn,¹ and Matthias Weidemüller^{1,‡}

¹*Physikalisches Institut, Universität Heidelberg, Im Neuenheimer Feld 226, 69120 Heidelberg, Germany*

²*Max-Planck-Institut für Quantenoptik, Hans-Kopfermann-Str. 1, Garching, Germany*

³*Kirchhoff-Institut für Physik, Universität Heidelberg,
Im Neuenheimer Feld 227, 69120 Heidelberg, Germany*

⁴*Univ. de Lille, CNRS, UMR 8523-PhLAM-Physique des Lasers, Atomes et Molécules, Lille, France*

⁵*PASQAL, 7 rue Léonard de Vinci, 91300 Massy, France*

⁶*Department of Physics and Materials Science, Faculty of Science,
Chiang Mai University, 239 Huay Kaeo Road, Muang, Chiang Mai, 50200, Thailand*

⁷*Institut für Theoretische Physik, Ruprecht-Karls-Universität Heidelberg,
Philosophenweg 16, 69120 Heidelberg, Germany*

⁸*Institute of Condensed Matter Theory and Optics,
Friedrich-Schiller-University Jena, Max-Wien-Platz 1, 07743 Jena, Germany*

(Dated: February 27, 2024)

Understanding how closed quantum systems dynamically approach thermal equilibrium presents a major unresolved problem in statistical physics. Generically, non-integrable quantum systems are expected to thermalize as they comply with the Eigenstate Thermalization Hypothesis. However, in the presence of strong disorder, the dynamics can possibly slow down to a degree that systems fail to thermalize on experimentally accessible timescales, as in spin glasses or many-body localized systems. In general, particularly in long-range interacting quantum systems, the specific nature of the disorder necessary for the emergence of a prethermal, metastable state—distinctly separating the timescales of initial relaxation and subsequent slow thermalization—remains an open question. We study an ensemble of Heisenberg spins with a tunable distribution of random coupling strengths realized by a Rydberg quantum simulator. We observe a drastic change in the late-time magnetization when increasing disorder strength. The data is well described by models based on pairs of strongly interacting spins, which are treated as thermal for weak disorder and isolated for strong disorder. Our results indicate a crossover into a pair-localized prethermal regime in a closed quantum system of thousands of spins in the critical case where the exponent of the power law interaction matches the spatial dimension.

I. INTRODUCTION

What is the fate of an isolated, strongly interacting, and possibly disordered quantum system initially prepared in a far-from-equilibrium state? In general, even if a strongly interacting quantum system is isolated from its environment, it is expected to thermalize [1–4]. As a notable exception to this rule, strongly disordered systems can retain retrievable memory of their initial state for arbitrarily long times, leading to a rich phenomenology ranging from glassy dynamics to many-body localization.

A comprehensive framework for understanding systems that do not undergo direct thermalization is provided by the concept of prethermalization [5–10]: Here, the Hamiltonian can be decomposed into a reference Hamiltonian H_0 , and a weak perturbation H_1 which

breaks at least one local conservation law of H_0 . In such instances, a metastable state exists whose properties can be calculated using the generalized Gibbs ensemble (GGE) of the reference Hamiltonian H_0 [11]. As an example, we can consider many-body localization (MBL) in the framework of prethermalization: Here, the reference Hamiltonian is given by a non-interacting ensemble of spins subject to a strongly disordered external field, and H_1 describes the interactions between nearest-neighbor spins. If these interactions are sufficiently weak, these systems remain localized [12, 13], and the conserved quantities become “dressed,” commonly referred to as l-bits [14, 15]. However, a different type of disorder naturally occurs in numerous systems, including cold atoms [16–23], ions [24] or nitrogen-vacancy centers [10, 25] where the couplings themselves are disordered, not the external field. In this case, discerning the reference Hamiltonian H_0 becomes nontrivial, and in previous studies, the depolarization dynamics in these systems is interpreted as direct thermalization [10, 25]. Yet, it is known from spin glasses that disorder in the couplings leads to a hierarchy of timescales,

* franzt@physi.uni-heidelberg.de

† martin.gaerttner@uni-jena.de

‡ weidemueller@uni-heidelberg.de

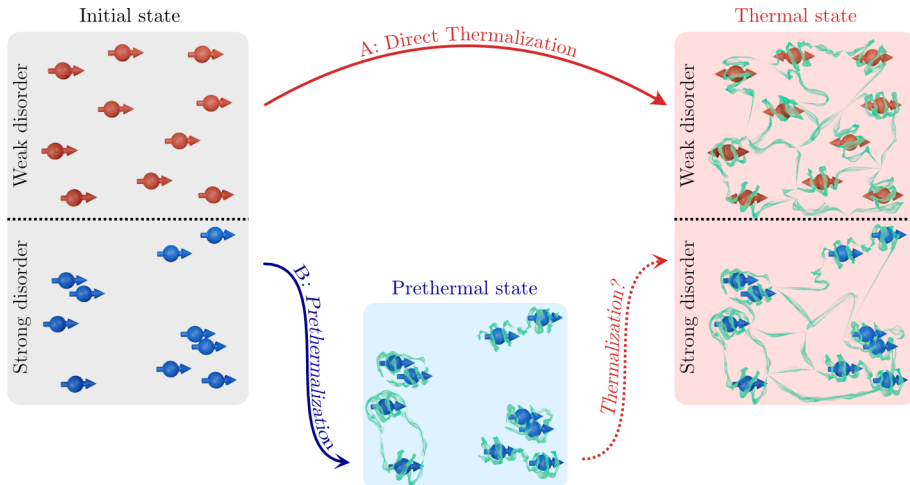


Figure 1. Thermal and non-thermal regimes. Schematic depiction of the dynamics of the system. Depending on the strength of disorder, initially, uncorrelated spins evolve either directly (via **A**) to a thermal state with correlations between all spins or (via **B**) to a prethermal state consisting of uncorrelated pairs of strongly correlated spins. Whether, in this case, thermalization occurs eventually remains an open question.

which slows down the dynamics such that on experimentally accessible timescales, these systems never reach thermal equilibrium.

Unfortunately, understanding if and how quantum systems thermalize is extremely challenging, as numerical simulations are limited to relatively small system sizes [26–28] and analytical solutions are scarce. Quantum simulation experiments with single-site resolution can investigate slightly larger systems with several tens of particles [29–33], but they can only probe finite time scales [17–19, 24].

In this study, we employ a Rydberg quantum simulator [34–36] to explore the thermalization dynamics in long-range interacting systems in 3D using a cloud of up to 6000 Rydberg spins with spatial disorder. In the weakly disordered regime, characterized by similar distances between particles (top row in Fig. 1), our experimental findings align with previous assertions of direct thermalization [25]. However, at strong disorder, we demonstrate the emergence of a localized prethermal state, verified through a non-analytical dependence of the late-time magnetization on an external field. Here, the hierarchy of interaction strengths allows us to effectively describe the Hamiltonian with a reference Hamiltonian H_0 , where strongly interacting pairs of spins remain localized for long times before interactions between pairs possibly lead to thermalization at even later times (bottom row in Fig. 1).

II. EXPERIMENTAL SETUP

We consider the quantum spin-1/2 Heisenberg XXZ-model (in units where $\hbar = 1$)

$$\hat{H}_{\text{int}} = \frac{1}{2} \sum_{i,j} J_{ij} \left(\hat{s}_x^{(i)} \hat{s}_x^{(j)} + \hat{s}_y^{(i)} \hat{s}_y^{(j)} + \delta \hat{s}_z^{(i)} \hat{s}_z^{(j)} \right), \quad (1)$$

with spin operators $\hat{s}_\alpha^{(i)} = \hat{\sigma}_\alpha^{(i)}/2$ ($\alpha \in \{x, y, z\}$) acting on spin i . The interactions between spins decay with a power law $J_{ij} = C_a r_{ij}^{-a} (1 - 3 \cos(\theta_{ij})^2)$, where r_{ij} are the distances between the spins i and j and θ_{ij} is the angle with respect to the quantization axis defined by the magnetic field. The parameters δ and a are determined by the choice of Rydberg states (cf. [35]). In our experiment, we encode the spin degree of freedom in the Rydberg states $|\downarrow\rangle = |48S\rangle$ and $|\uparrow\rangle = |48P\rangle$ leading to dipolar interactions as described by Eq. (1) with $\delta = 0$, $a = 3$ and $C_3/(2\pi) = 1.15 \text{ GHz } \mu\text{m}^3$. Additional data for a Van-der-Waals interacting system ($a = 6$, $C_6/(2\pi) = 507 \text{ GHz } \mu\text{m}^6$, $\delta \approx -0.7$ and no angular dependence on θ_{ij}) is shown in Appendix B.

The spins are distributed randomly with an imposed minimal distance r_{bl} resulting in a random but correlated distribution of couplings J_{ij} (Fig. 1). This geometry is naturally given in the experiment where the Rydberg blockade effect forbids two excitations being closer than r_{bl} . The blockade constraint allows tuning the strength of the disorder: For the weak disorder measurements, we chose the density such that the typical interparticle distance of $a_0 \sim 6.8 \mu\text{m}$ is comparable to the blockade radius of $4.6 \mu\text{m}$, whereas in the strongly disordered case, the blockade radius of $5.0 \mu\text{m}$

is much smaller compared to the typical interparticle distance $a_0 \approx 11.2 \mu\text{m}$ (see methods for more details on the Rydberg atoms' distribution). In both cases, the median interaction strengths of $J_{\text{median}}/(2\pi) = \text{median}_i(\max_j |J_{ij}|)/(2\pi) = 2.8 \text{ MHz}$ (weak disorder) or $J_{\text{median}}/(2\pi) = 1.1 \text{ MHz}$ (strong disorder) is large compared to typical decoherence rates like the decay rate of the Rydberg atoms of $\Gamma/(2\pi) = 0.018 \text{ MHz}$. The maximal duration of the experiment of $10 \mu\text{s}$ is chosen such that the Rydberg decay can still be considered small.

By coupling the spin states with a microwave field Ω , we perform a Ramsey protocol (schematically depicted in Fig. 2 **a**) where a first $\pi/2$ pulse initially prepares the system in the fully x -polarized state $|\psi_0\rangle = |\rightarrow\rangle_x^{\otimes N} = 2^{-N/2}(|\uparrow\rangle + |\downarrow\rangle)^{\otimes N}$ (see methods for details of the experimental protocol) which shows no classical dephasing or dynamics in a mean-field description where for each atom, the effective field is aligned with the polarization of the atoms (see Fig. 2 **a** center). With a second $\pi/2$ -pulse, we read out the average magnetization $\langle \hat{S}_x \rangle = \langle \sum_i \hat{s}_x^{(i)} \rangle / N$. Since this observable is an average over local (single-spin) observables, it should relax to its thermal value if the system is locally thermalizing.

III. HIERARCHY OF RELAXATION TIME SCALES

The blue dots in Fig. 2 **b** (strong disorder) and the red dots in Fig. 2 **c** (weak disorder) labeled with 0.0 MHz show the time evolution of the magnetization under \hat{H}_{int} . In both regimes, the magnetization relaxes to zero, following a stretched exponential law as discussed in previous work [37–39], and reaches a steady-state on a time scale of $\sim 2\pi/J_{\text{median}}$ in units of the inverse median nearest neighbor interaction strength. This depolarization dynamics is a direct consequence of the symmetry of the interaction Hamiltonian as all eigenstates already have vanishing x -magnetization due to the conservation of $\sum_i \hat{s}_z^{(i)}$ ¹.

This situation changes when adding a homogeneous transverse field term to the Hamiltonian

$$\hat{H}_{\text{ext}} = \Omega \sum_i \hat{s}_x^{(i)}, \quad (2)$$

which breaks the $U(1)$ symmetry and leads to a finite late-time magnetization as the data in Fig. 2 **b** and **c** shows. As a result, the dynamics still feature an initial fast relaxation on the time-scale of $2\pi/J_{\text{median}}$, fol-

lowed by a slowly relaxing regime. The stronger the applied magnetic field, the sooner the metastable regime is reached, and the higher the magnetization value becomes.

The finite late-time value of the magnetization of these curves may be understood on a qualitative level by a simple, intuitive, spin-locking model [40]. At strong field $\Omega \gg J_{\text{median}}$, the inter-spin interaction cannot overcome the magnetic forces and so the spins stay put. Lowering the external field strength weakens this lock and the spins can start dephasing due to their interactions.

As a consistency check, we compare the experimental data to semiclassical truncated Wigner approximation (dTWA) (solid lines in Fig. 2 **b** and **c**). All simulated curves agree well with the experimental data except for the strongest magnetic field strength, confirming the quality of our quantum simulation of the Heisenberg model. The deviations at strong magnetic field (see grey dots in Fig. 2 **b** are likely caused by an experimental imperfection as the strong field may lead to additional couplings to other Rydberg states. This induces population loss to states, which are not measured, thus reducing the total magnetization. Therefore, all experimental data at external field strength above 5 MHz are greyed out.

IV. PRETHERMALIZATION IN DISORDERED SPIN SYSTEMS

The striking difference between strongly and weakly disordered cases becomes apparent when examining the dependence of the plateau value on the external field measured after $10 \mu\text{s}$ (see Fig. 2 **d** and **e**). For strong disorder, there is a sharp cusp at $\Omega = 0 \text{ MHz}$, which is not present for weak disorder, where the curve is very smooth. Note that this is not an artifact of the difference in absolute scale of the x-axis caused solely by the on average weaker interactions in the strongly disordered case. Relative to their respective median interaction strength J_{median} , both plots cover a similar range. For a generic, thermalizing system, it is plausible to expect a smooth parametric dependence based on the Eigenstate Thermalization Hypothesis (ETH). We will argue that the cusp feature is a clear signature of a non-thermal state, consistent with a generalized Gibbs ensemble with extensively many conserved quantities.

To explain the curve in the strongly disordered regime, characterized by a small blockade radius r_{bl} and significant variations in the nearest neighbor inter-spin distances, we employ a model based on pairs of strongly interacting spins: For strong positional disorder, close-by spins form pairs that approximately decouple from the rest of the system as the energy splitting between their eigenstates will typically be much larger than any

¹ From the conservation of \hat{S}_z , i.e. $[\hat{S}_z, \hat{H}_{\text{int}}] = 0$, it follows that $\langle \hat{S}_x \rangle = -i\langle [\hat{S}_y, \hat{S}_z] \rangle = 0$ for every eigenstate.

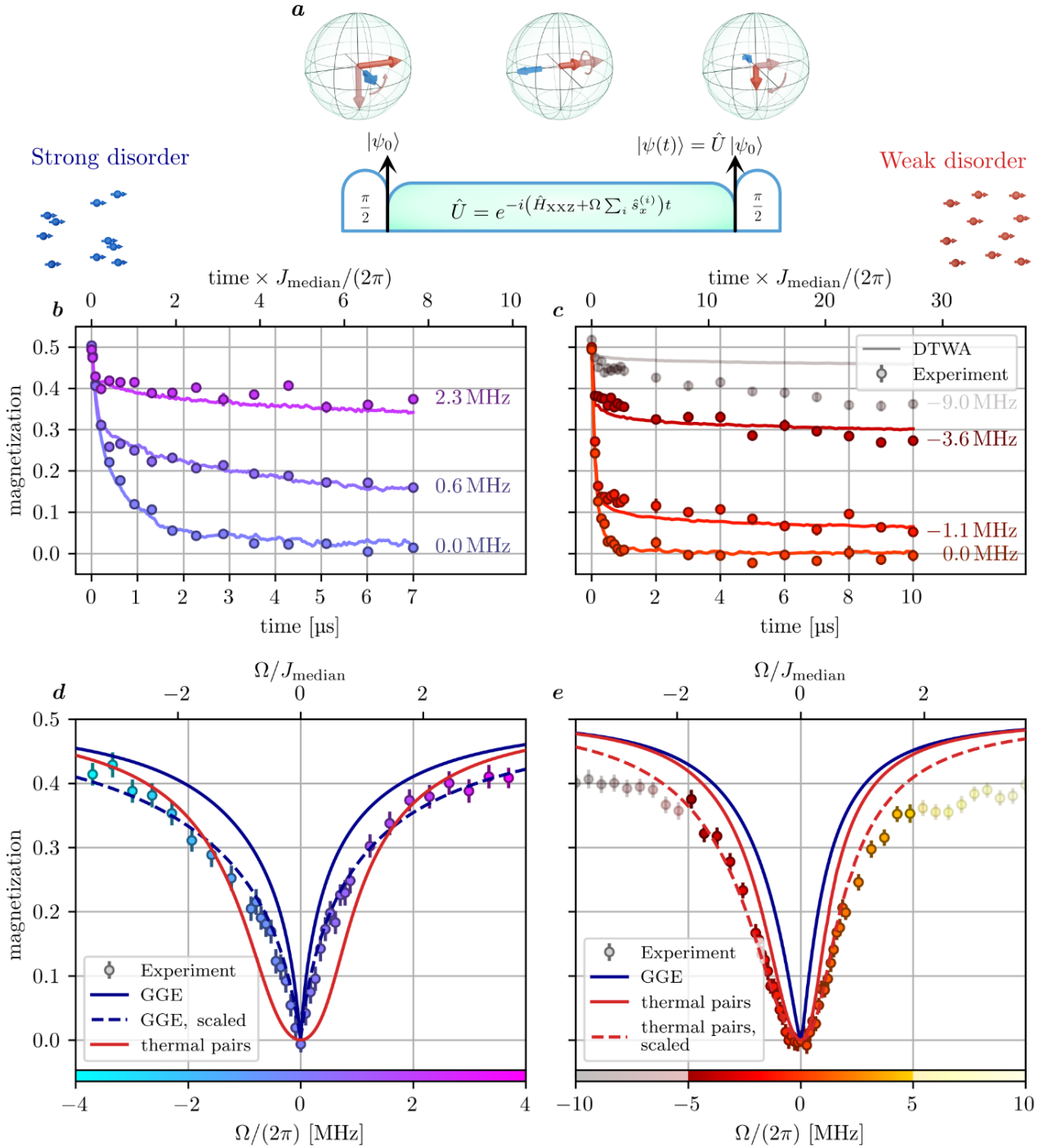


Figure 2. Late-time magnetization for different strength of disorder for a spin system interacting with dipole-dipole interactions. **a** Experimental protocol: A $\pi/2$ pulse (blue arrow in the Bloch sphere) rotates the spins from the z (light red arrow) to the x -direction (red arrow). During the subsequent time evolution, the system interacts via the Heisenberg Hamiltonian (1) while a spin locking field at Rabi frequency Ω is applied. The final magnetization is read out after a second $\pi/2$ -pulse. **b** (strong disorder) and **c** (weak disorder): Measured spin relaxation dynamics for varying transverse field strengths. The solid lines show semiclassical DTWA simulations. **d** (strong disorder) and **e** (weak disorder): Magnetization after 10 μs as a function of field strength Ω . The solid blue (red) lines show the magnetization expected from a GGE (4) (canonical ensemble (5)). The dashed lines show the same simulations rescaled by a global factor to best fit the experimental data.

other terms in the Hamiltonian affecting the pair [41–45]. In the presence of an external field, such a pair, initially in a fully polarized state, will undergo coherent oscillations and depolarize only very slowly as it does not become entangled with the rest of the system until very late times [38]. Thus, the depolarization dynamics arises due to dephasing among pairs oscillating at different frequencies due to different interaction strengths.

Thus, returning to the notion of prethermalization introduced above, H_0 is given by the part of the full Hamiltonian that acts on single pairs, while interactions between the pairs form the weak part H_1 . Since H_0 factorizes into contributions of the individual pairs, we can make a prediction for the prethermal steady state magnetization. On average, each pair contributes

$$\overline{\langle \hat{S}_x \rangle_{\text{pair}}} = \frac{\Omega^2}{2(\Omega^2 + j^2)} \quad (3)$$

to the total magnetization, where $j = J(\delta - 1)$ and J the pair's coupling (see Appendix C for a detailed derivation). The distribution of pair couplings can be found numerically by sampling blockaded positions. To calculate the steady-state value, we use a self-consistent mean-field approach to assign each pair an effective field strength Ω_i taking into account the interaction with its surroundings. This leads to the asymmetry around $\Omega = 0$, as for $\Omega > 0$, the mean-field contribution adds to the static part and thus results in a larger effective field, while for $\Omega < 0$ the converse is true. This effect is much more prominent in the case of $\alpha = 6$ as shown in the appendix in Fig. 4.

In essence, this mean-field pair model describes the system as a generalized Gibbs ensemble

$$\rho_{\text{GGE}} \propto \exp \left(- \sum_i \beta_i H_{\text{pair},i}^{(\text{mf})} \right) \quad (4)$$

of pairs governed by $H_{\text{pair},i}^{(\text{mf})}$, where the Lagrange multipliers β_i are fixed by energy conservation. Using this model, we find qualitative agreement with the experimental data in the case of strong disorder (blue, solid line in Fig. 2d). If the interaction strength of the pair simulation is artificially increased by a factor of 1.75 (dashed blue line), we find even perfect agreement with the experiment. We conjecture that this factor is needed to take into account interactions beyond the nearest neighbor.

Thus, we have shown that the system is consistent with a prethermal description in the sense, that we found a quasi-stationary state inconsistent with a thermal ensemble description yet matching a generalized Gibbs ensemble. Furthermore, this prethermal state is localized as the pairs' eigenspaces constitute local integrals of motion.

In the less disordered regime, this model of isolated pairs also predicts a sharp, narrow shape (see blue, solid line in Fig. 2 e) which does not match the experimental data even on a qualitative level. In this regime, the approximation of isolated pairs of spins is no longer valid, and we need to consider the build-up of entanglement between different pairs of spins, which leads to fast thermalization. While the full treatment of the highly correlated many-body system of 6000 spins is not feasible on a classical computer, we can make the first order approximation that the system itself acts as a thermal bath for each pair and imposes that all pairs thermalize to the same global temperature (see also Appendix C):

$$\rho_{\text{can}} \propto \exp \left(-\beta \sum_i H_{\text{pair},i}^{(\text{mf})} \right) \quad (5)$$

Here, β is defined implicitly by energy conservation $\text{Tr } \rho_{\text{can}} \hat{H} = \langle \psi_0 | \hat{H} | \psi_0 \rangle$. We find qualitative agreement between this model (red, solid line) and experimental data. The agreement can be improved by increasing the interactions by a factor of 1.4 (red, dashed line) that effectively takes into account the correlations between distant spins that are neglected in the pair description of eq. 5. The deviation at strong field is likely caused by coupling to different Rydberg states as remarked earlier.

As a consistency check, we also try to explain the data in the strong-disorder regime with the canonical ensemble description (see Fig. 2 d) which clearly fails to reproduce the observed sharp cusp around $\Omega = 0$ MHz.

V. CONCLUSION AND DISCUSSION

We studied the relaxation dynamics of power-law interacting spins by observing the change in the parametric dependence of the late-time magnetization on an external field. By finding simple models based on pairs of strongly interacting spins, we explained the measured data both in the weak and strong disorder regime revealing a fundamental change in the dynamical properties of the system on experimentally accessible timescales. Our results indicate the presence of a crossover from a thermalizing regime to a prethermal pair-localized regime caused by positional disorder.

The method for observing prethermal localization used in this work is inherently versatile and may also be applied to study thermalization in other systems. The signature that distinguishes thermalized from localized systems is the smooth dependence of the steady-state magnetization(, which is absent in the latter). This consideration becomes particularly crucial when the system's components, such as the pairs of spins in this study, experience rapid dephasing. This dephasing generally occurs on a much faster timescale compared

to the build-up of entanglement between these components, resulting in thermalization. This insight calls for the reevaluation of claims made in [10, 25], given that the relaxation of the magnetization in spatially disordered spin systems reflects only the dephasing but not the thermalization process.

Notably, our system implements a critical case where the power law dependence of the interaction strength with distance a equals the spatial dimension $d = 3$. In this regime, theoretical results for large systems are scarce due to competing scales. In Appendix B, we show a similar experiment for a Van-der-Waals interacting system where $a = 2d = 6$. In this case, the magnetization behaves qualitatively as in the strongly disordered case of $\alpha = 3$ and also shows a sharp cusp. This indicates that prethermalization caused by localized pairs of spins is a robust effect independent of the spatial dimension as long as disorder is sufficiently strong.

This study paves the way toward exploring the late-time dynamics of far-from-equilibrium systems with power-law interactions and disordered couplings, which are ubiquitous in nature. For these systems, it is yet an open question if they show (prethermal) many-body localization similar to the standard model of MBL where the on-site potential is disordered. Recent theoretical and numerical results indicate that localization and the consequent absence of thermalization are excluded in dimensions $d > 1$ and for power law interactions [23, 46]. However, the type of spatial disorder investigated in this study differs significantly from that in traditional MBL systems, rendering most conventional arguments about instability and eventual thermalization not directly applicable. Intriguingly, first numerical studies [45] suggest that for the type of disorder studied here, localization effects are surprisingly robust to finite size drifts, a significant issue for the numerical investigation of the standard model of MBL. To draw parallels between our findings of prethermalization and prethermal MBL, it will be decisive to investigate the scaling of the relaxation timescale with the strength of disorder which is expected to be exponential in the case of prethermal MBL [47]. However, a proper definition of the strength of disorder in case the disordered couplings, opposed to disordered on-site detuning, remains an open question. Finally, an exciting avenue for future research is to explore the relation between the slow relaxation dynamics observed in this work and quantum spin glasses. In quantum spin glasses, the combination of frustration, low energies and disorder leads to exceptionally slow relaxation dynamics, a phenomenon being highly relevant to the approach of quantum computation via quantum annealing [48, 49].

METHODS

Here we provide further details on the numeric simulations, the experimental protocol and the spatial configuration of the Rydberg cloud.

Details on experimental implementation. We start the experiment by trapping 10^6 Rubidium-87 in a cigar shaped dipole trap with a diameter of $300\text{ }\mu\text{m}$ (long axis) and $70\text{ }\mu\text{m}$ (short axis) at a temperature of $10\text{ }\mu\text{K}$. We consider this gas to be frozen since the atoms move only a distance of $d_{\text{kin}} = t_{\text{exp}} \sqrt{\frac{3kT}{m}} = 0.5\text{ }\mu\text{m}$ during an experimental cycle of $t_{\text{exp}} = 10\text{ }\mu\text{s}$ which is small compared to the Rydberg blockade radius of $r_{\text{bl}} \approx 5\text{ }\mu\text{m}$. After optically pumping the atoms into the state $|5S(F=2, m_F=2)\rangle$, we optically excite the atoms to the spin state $|\downarrow\rangle$ via a two-photon off-resonant excitation process (single-photon detuning of 98 MHz and two-photon Rabi frequency of 1 MHz). A global microwave $\pi/2$ -pulse prepares the fully polarized initial state $|\psi_0\rangle = |\rightarrow_x\rangle^{\otimes N}$. For the dipolar interacting spin system, we couple the states $|48S\rangle$ and $|48P\rangle$ resonantly with a single-photon transition at 35 GHz . This frequency is generated by mixing a 5 GHz signal of the Keysight M8190A AWG with an Anritsu MG3697C signal generator. In the case of Van-der-Waals interactions, the state $|61S\rangle$ is coupled resonantly to $|62S\rangle$ via a two-photon transition at a microwave frequency of 16.546 GHz which can be directly generated with a Keysight M8190A arbitrary waveform generator (AWG).

The same microwave setup is used to realize the spin locking field where a phase shift of 90 degrees needs to be added such that the field aligns with the spins. This allows us to implement the transverse field term, Eq. (2), with field strengths up to $\Omega/(2\pi) = 10\text{ MHz}$. After a time evolution t , the x -magnetization is rotated tomographically onto the z -axis by applying a second $\pi/2$ -pulse with various phases. Finally, the magnetization is obtained from a measurement of the population of one of the two spin states via field ionization, and the other spin state is optically deexcited to the ground state. A visual representation of the measurement protocol can be found in Fig. 2 **a**, and a more detailed explanation of the determination of the magnetization was reported in a previous publication [37].

Details on the Rydberg distribution. In this work, we can tune the disorder with the Rydberg blockade effect, which imposes a minimal distance r_{bl} between the spins. At small blockade radius, the spins are distributed randomly in the cloud, while a large radius introduces strong correlation between the atom positions and, hence, the coupling strength. To quantify the disorder strength, we compare the blockade radius to typical interparticle distance, which can be estimated from the Wigner-Seitz radius $a_0 = [3/(4\pi\rho)]^{1/3}$. We ad-

just this parameter in our experiment by controlling the Rydberg fraction, which is dependent on the excitation time t_{exc} . In addition, we tune the Rydberg density ρ by varying the volume of the ground state atoms with a short time-of-flight period after turning off the dipole trap and before exciting to the Rydberg states. We measure the resulting Rydberg density through depletion imaging [50] where we deduce the Rydberg distribution from the missing ground state atoms after Rydberg excitation. The measured parameters of the Rydberg distribution are presented in detail in Table I in the appendix.

To estimate the Rydberg blockade radius, we model the excitation dynamics by the simplified description introduced in [37] which assumes a hard-sphere model for the Rydberg blockade effect. This model sets an upper limit on the blockade radius $r_{\text{bl}} = \sqrt[6]{\frac{C_6}{\Gamma_{\text{eff}}}}$ by estimating the effective linewidth of the laser, based on the duration of the excitation pulse and power broadening. The latter is calculated self-consistently, taking into account the enhancement factor induced by collective Rabi oscillations within a superatom [51, 52].

This established model of the Rydberg cloud can be benchmarked using the experimentally measured time evolution, which is known to be well described by semiclassical Discrete Truncated Wigner Approximation (DTWA) in case no locking field is applied [37] (see Fig. 3 in appendix A). This simulation is highly sensitive with respect to the blockade radius and the density, and can therefore be used to determine these experimental parameters in case of weak and strong disorder. From the excitation model, we can also compute the median of the nearest neighbor interaction strength J_{median} which ranges from 1.1 MHz to 2.8 MHz depending on the experimental setting (see table I). The resulting time evolution can be considered unitary for up to $10\text{ }\mu\text{s}$, which is an order of magnitude larger than the timescale of the experiment $2\pi/J_{\text{median}}$.

Appendix A: Semiclassical DTWA simulations

In previous work [37, 53], we could show that the semiclassical Discrete Truncated Wigner Approximation (DTWA) is well suited to describe the relaxation of the magnetization under the interaction Hamiltonian (1) defined in the main text. The main principle of DTWA is to sample classical time evolutions over different initial states such that the quantum uncertainty of the initial state is respected [54]. In Fig. 3, we compare the time evolution obtained from DTWA simulations to the experimental data (red dots) in the case of weak (left panels) and strong disorder (right panels). It turns out that the resulting dynamics depend sensitively on the blockade radius and on density. However, the same fitted parameters describes the time evolution for different locking fields (top panels) and the dependence of the late-time magnetization on the field strength. As mentioned in the main text, the observed discrepancy of DTWA simulations and experimental data observed for large fields in the weakly disordered regime (Fig. 3 c) can be most likely attributed to experimental imperfections such as coupling to other Rydberg states due to power broadening of the microwave transition.

Appendix B: Data for Van der Waals interactions

By encoding the spin degree of freedom in different Rydberg states, it is possible to realize different Hamiltonians with different range of interactions. In addition to a dipolar interacting Hamiltonian with $a = d = 3$ as shown in the main text, we can also create a spin system with less long-range Van der Waals interactions. For this purpose, we couple the Rydberg state $|\downarrow\rangle = |61S\rangle$ to $|\uparrow\rangle = |62S\rangle$ which results in a Heisenberg XXZ Hamiltonian as described by Eq. (1) with $\delta = -0.7$, $a = 6$ and $C_6/(2\pi) = 507 \text{ GHz } \mu\text{m}^6$ (see also Table I for an overview over the experimental parameters).

Similar to the experimental results presented in the main article, also the Van der Waals interacting system shows a slow relaxation dynamics on a timescale of $\approx 2\pi/J_{\text{median}}$ (see Fig. 4 a). Applying an external field Ω also slows down the relaxation dynamics considerably. It should be noted, that the external field has to be realized by a two-photon microwave transition as the transition between the two spin states is dipole forbidden. Therefore, the single photon Rabi frequencies are required to be much larger compared to the dipolar interacting spin system, which might potentially lead to a stronger coupling to different Rydberg states inducing addition decay of the magnetization, especially at late times.

The dependence of the late-time magnetization (taken after 10 μs) on the spin locking field Ω of the

Van der Waals interacting system is shown in Fig. 4 b. Compared to the dipolar interacting case presented in the main text, the curve is even more asymmetric. This effect can be explained by the isotropic repulsive interactions in the Van der Waals case, whereas dipolar couplings vary as $1 - 3 \cos(\theta)^2$ depending on the angle θ between the inter-spin axis and the quantization axis. Most importantly, also the Van der Waals interacting system features a sharp cusp around $\Omega = 0 \text{ MHz}$. In this regard, the curve strongly resembles the case of strong disorder in dipolar interacting systems presented in the main text. At first sight, this result might be surprising as the spin system is even more blockaded with a ratio of blockade radius to typical interaction range of $r_{\text{bl}}/a_0 = 5.7/7.8 = 0.73$ than the weakly disordered dipolar system where $r_{\text{bl}}/a_0 = 4.6/6.8 = 0.68^2$. However, the shorter-range interaction increases the effective disorder in the system as the nearest-neighbor interaction becomes much stronger compared to the next-nearest neighbor coupling. This proves that, especially for short-range interactions decaying faster than $a = d$, the existence of a prethermal state is a ubiquitous phenomenon in spatially disordered quantum spin systems.

Appendix C: Derivation of the effective model

In this appendix, we derive how to describe the system in terms of localized pairs, which constitute the approximate local integrals of motion for the GGE description of the system. Starting from the physics of a single, isolated pair, we will derive the GGE, the description in terms of thermal pairs, and the self-consistent mean-field equations, which partly take into account interactions beyond the nearest neighbor. This approximation provides an intuitive picture that allows us to explain all the observed features of the long-time magnetization (positivity, cusp, asymmetry).

For a single interacting pair, in the basis

² Due to the Van der Waals interactions being a second order process, the typical interaction strength are much weaker compared to the dipolar interacting case. To compensate for this effect, we increase the density which increases the interaction strength.

	Dipolar interactions (weak disorder)	Dipolar interactions (strong disorder)	Van-der-Waals interactions
Rydberg states	$ 48S_{1/2}\rangle \leftrightarrow 48P_{3/2}\rangle$	$ 48S_{1/2}\rangle \leftrightarrow 48P_{3/2}\rangle$	$ 61S_{1/2}\rangle \leftrightarrow 62S_{1/2}\rangle$
decay rate $\Gamma/(2\pi)$	0.018 MHz	0.018 MHz	0.0096 MHz
t_{exc}	10 μs	1 μs	5 μs
Excitation volume	$59 \mu\text{m} \times 44 \mu\text{m} \times 36 \mu\text{m}$	$59 \mu\text{m} \times 34 \mu\text{m} \times 30 \mu\text{m}$	$69 \mu\text{m} \times 43 \mu\text{m} \times 37 \mu\text{m}$
N_{Ryd}	6895	775	2907
r_{bl}	4.6 μm	5.0 μm	5.7 μm
a^0	6.8 μm	11.2 μm	7.8 μm
$J_{\text{median}}/(2\pi)$	2.8 MHz	1.1 MHz	0.5 MHz

Table I. Experimental parameters. t_{exc} specifies the duration of the optical excitation to the Rydberg state, the Rydberg volume is specified by the radii ($1/e^2$) of the Rydberg cloud, N_{Ryd} denotes the derived Rydberg number, r_{bl} the blockade radius and J_{median} the obtained median nearest-neighbor interaction.

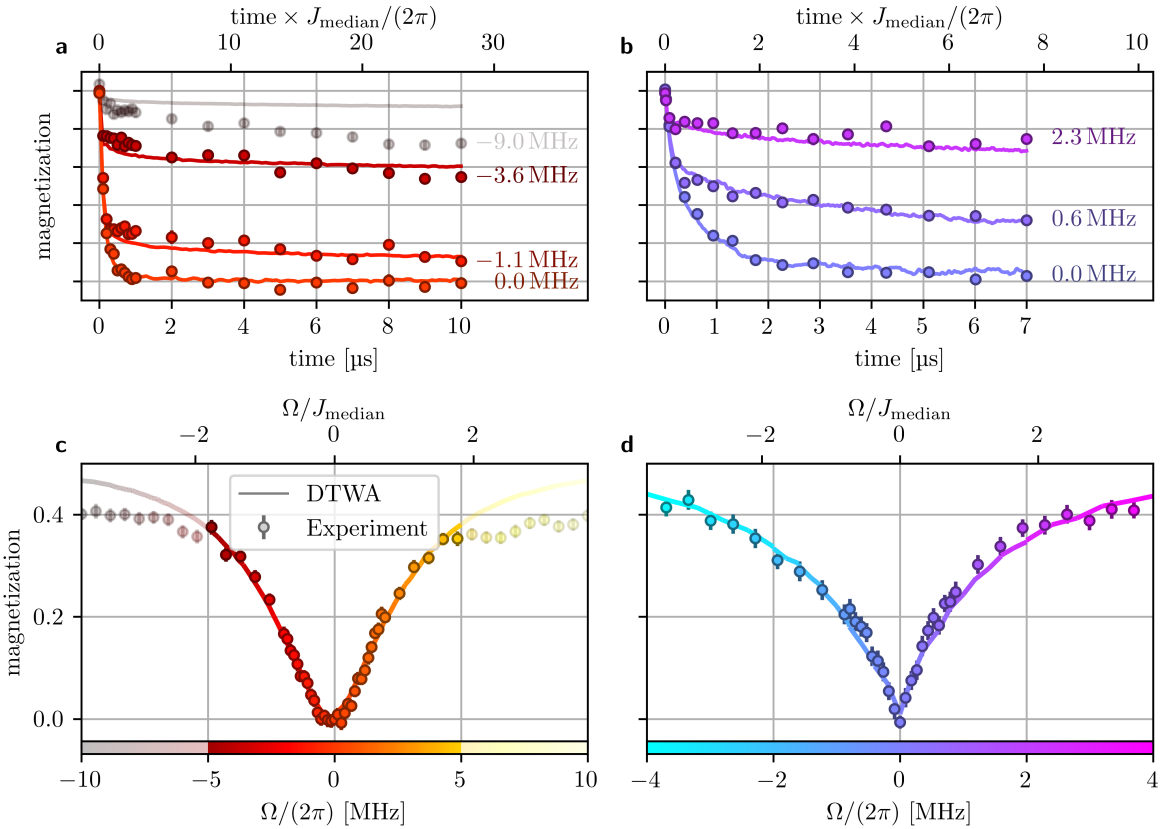


Figure 3. **Simulation of the experimental data shown in the main text with DTWA simulations** Time evolution of the magnetization in case of weak (a) and strong (b) disorder. The dependence of the late-time magnetization are shown in c (weak disorder) and a (strong disorder). The experimental parameters are shown in Table I.

$\{| \rightarrow \rightarrow \rangle, | \rightarrow \leftarrow \rangle, | \leftarrow \rightarrow \rangle, | \leftarrow \leftarrow \rangle\}$, Hamiltonian (1) reads

$$\hat{H}_{\text{pair}} = 4J \left(\Delta \hat{s}_x^{(1)} \hat{s}_x^{(2)} + \hat{s}_y^{(1)} \hat{s}_y^{(2)} + \hat{s}_z^{(1)} \hat{s}_z^{(2)} \right) + \Omega \sum_{i=1}^2 \hat{s}_z^{(i)} \quad (\text{C1})$$

$$= \begin{pmatrix} J + \Omega & 0 & 0 & J(\Delta - 1) \\ 0 & -J & J(\Delta + 1) & 0 \\ 0 & J(\Delta + 1) & -J & 0 \\ J(\Delta - 1) & 0 & 0 & J - \Omega \end{pmatrix} \quad (\text{C2})$$

where we defined $J = J_{12}/4$. Out of the four eigenstates of this Hamiltonian, only two have non-zero overlap with the initial state $|\rightarrow \rightarrow \rangle$ (see table II). Therefore, each interacting pair can be seen as an effective two-level system on its own, with a modified interaction between these "renormalized" spins. This ansatz of diagonalizing the strongest interacting pairs first can be seen as a first step in a real-space strong-disorder renormal-

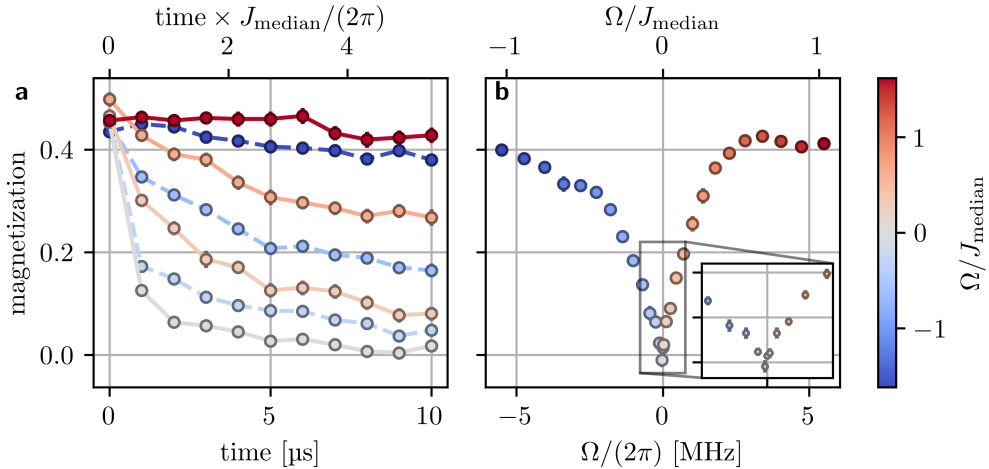


Figure 4. Experimental data for a quantum spin system with Van der Waals interactions. **a**, Measured spin relaxation dynamics for varying transverse field strengths ranging from $\Omega/(2\pi) = -5.5$ MHz (dark blue) to 5.5 MHz (dark red). **b**, Magnetization after 10 μ s as a function of field strength Ω (see Table I for a summary of the experimental parameters). The inset shows a zoom into the data for small values of Ω .

ization group treatment [55–58]. Here, we do not aim to proceed further in this renormalization scheme, but instead, we use the basis of eigenstates of strongly interacting pairs to derive an intuitive understanding of the physics within mean-field theory.

Diagonal ensemble: In contrast to a single spin which does not show any dynamics, a strongly interacting pair features oscillatory dynamics. Using the definition given in the main text, we can calculate the diagonal ensemble expectation value for single pair:

$$\overline{\langle \hat{S}_x \rangle_{\text{pair}}} = \frac{\Omega^2}{2(\Omega^2 + j^2)} \quad (\text{C3})$$

where we introduced $j = J(\Delta - 1)$. It should be noted that this diagonal ensemble does not describe the steady-state but rather the time average over the oscillations. The magnetization expectation value predicted by the diagonal ensemble of a single interacting pair represents an inverted Lorentz profile with width $j/2$, which features a quadratic dependence on Ω around zero (see Figure 5 **a**). However, if we average over multiple pairs with different interaction strengths j , the diagonal ensemble value becomes more meaningful since we can assume that the different oscillation frequencies dephase. Also, the behavior of the magnetization changes: For example, assuming a uniform distribution

of $j \in [0, \Delta_j]^3$, we obtain

$$\frac{1}{\Delta_j} \int_0^{\Delta_j} \overline{\langle \hat{S}_x \rangle_{\text{pair}}} dj = \frac{\Omega}{2\Delta_j} \arctan\left(\frac{\Delta_j}{\Omega}\right) \quad (\text{C4})$$

which shows the non-analytic cusp feature at $\Omega = 0$ (see Figure 5 **b**). Close to the non-analytic point, the magnetization increases linearly with a slope $\frac{\pi}{4\Delta_j}$ inversely proportional to the width of the distribution of interaction strengths. Therefore, we can conclude that the non-analyticity is a direct consequence of disorder and the resulting broad distribution of nearest neighbor interaction strengths.

Canonical and generalized Gibbs ensemble: To calculate the properties of a system in thermal equilibrium, we evaluate the density matrix $\hat{\rho}_{\text{canonical}}$ of the canonical ensemble

$$\hat{\rho}_{\text{canonical}} = \frac{\sum_i e^{-\beta E_i} |\psi_i\rangle \langle \psi_i|}{\sum_i e^{-\beta E_i}} \quad (\text{C5})$$

where β is the inverse temperature of the system. For a single pair of spins, this ensemble can be used to calculate the expectation value of the magnetization:

$$\langle \hat{s}_x^p \rangle_{\text{canonical}}(\beta) = -\frac{h}{2\sqrt{h^2 + j^2}} \tanh\left(\sqrt{h^2 + j^2}\beta\right) \quad (\text{C6})$$

³ For distributions like $j \in [j_{\min}, \Delta_j]$ that do not feature arbitrary small interaction strengths, a small region of approximate size $\Omega < |\frac{j_{\min}}{\Delta_j}|$ exists where magnetization is a smooth function of external field.

Eigenvalue E_i	Eigenvector $ \psi_i\rangle$	Occupation $ \langle\psi_0 \psi_i\rangle ^2$	Magnetization $\langle \hat{S}_x \rangle_{\psi_i}$
$J\Delta$	$\frac{1}{\sqrt{2}}(\rightarrow\leftarrow\rangle + \leftarrow\rightarrow\rangle)$	0	0
$-J(2 + \Delta)$	$\frac{1}{\sqrt{2}}(\rightarrow\leftarrow\rangle - \leftarrow\rightarrow\rangle)$	0	0
$J - \sqrt{\Omega^2 + J^2(\Delta - 1)^2}$	$\sqrt{\frac{1}{2} - \frac{\Omega}{2\sqrt{\Omega^2 + j^2}}} \rightarrow\rightarrow\rangle + \sqrt{\frac{1}{2} + \frac{\Omega}{2\sqrt{\Omega^2 + j^2}}} \leftarrow\leftarrow\rangle$	$\frac{1}{2} - \frac{\Omega}{2\sqrt{\Omega^2 + j^2}}$	$-\frac{\Omega}{2\sqrt{\Omega^2 + j^2}}$
$J + \sqrt{\Omega^2 + J^2(\Delta - 1)^2}$	$\sqrt{\frac{1}{2} + \frac{\Omega}{2\sqrt{\Omega^2 + j^2}}} \rightarrow\rightarrow\rangle + \sqrt{\frac{1}{2} - \frac{\Omega}{2\sqrt{\Omega^2 + j^2}}} \leftarrow\leftarrow\rangle$	$\frac{1}{2} + \frac{\Omega}{2\sqrt{\Omega^2 + j^2}}$	$\frac{\Omega}{2\sqrt{\Omega^2 + j^2}}$

Table II. Properties of the four eigenstates of a single interacting spin pair. To simplify notation, we introduced $j = J(\Delta - 1)$.

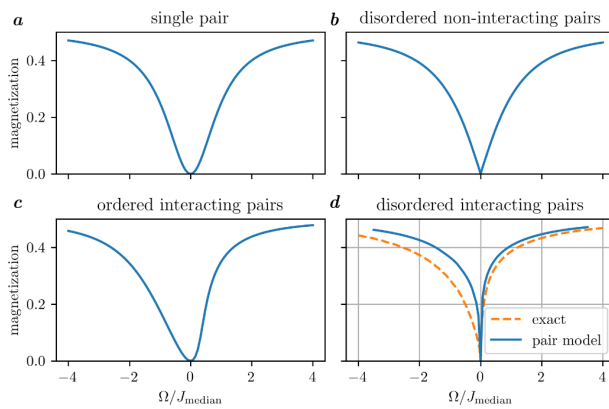


Figure 5. The diagonal ensemble expectation value of the magnetization as a function of applied external field Ω for a single pair (a), a disorder average of single pairs with interaction chosen randomly in the interval $J \in [0, 1]$ (b), a system of identical pairs that interact with mean field interaction $J_{\text{inter}} = 1.5 * J$ (c), and a realistic random distribution with power-law interactions, as described in the text (d). For the latter, the dashed orange line shows the full quantum mechanical solution obtained by exact diagonalization for the same system.

In a system coupled to a thermal bath, the inverse temperature β would be determined by the temperature of the bath. However, in a closed the system, the energy is conserved, which fixes the inverse temperature such that the energy of the canonical ensemble equals the energy of the initial state. In a generalized Gibbs ensemble, where the energy of each pair of spins is conserved, this leads to the equation

$$\langle \hat{H}_{\text{pair}} \rangle_{\text{canonical}}(\beta) \stackrel{!}{=} \langle \hat{H}_{\text{pair}} \rangle_{|\psi_0\rangle} \quad (\text{C7})$$

$$\Leftrightarrow -\sqrt{h^2 + j^2} \tanh\left(\sqrt{h^2 + j^2}\beta\right) + J \stackrel{!}{=} h + J \quad (\text{C8})$$

This equation can be solved analytically and results in exactly the diagonal ensemble from Eq. C3. This result

is not surprising considering the following argument: Only two out of four eigenstates of the pair of spins can be occupied due to symmetry arguments. Thus, any mixture of these states is completely determined by only two variables. Out of those, one is fixed by normalization and the other by energy, and all ensembles are strictly equivalent.

In the generalized Gibbs ensemble, we have considered an ensemble of perfectly isolated pairs, where each pair i has equilibrated to a different inverse temperature β_i . A first approximation to estimate the magnetization of a thermalized ensemble of disordered spins can be obtained by assuming weak interactions between each pair of spins that do not affect the eigenstates but lead to thermalization such that every spin relaxes to a canonical ensemble with one global $\beta = \beta_i$ for all pairs i . In this case, eq. (C7) has to be solved for β for the sum of all pairs:

$$\sum_i \langle \hat{H}_{\text{pair},i} \rangle_{\text{canonical}}(\beta) \stackrel{!}{=} \sum_i \langle \hat{H}_{\text{pair},i} \rangle_{|\psi_0\rangle}. \quad (\text{C9})$$

For this value of β , the canonical ensemble expectation value for the average magnetization can be calculated using equation (C5).

Self-consistent mean-field equations: To obtain an even more realistic model and to understand additional features like the asymmetry of the cusp, we add a mean-field interaction between pairs. For this purpose, we replace the external field with an effective mean-field acting on spin i :

$$\Omega \rightarrow \Omega_i = \Omega + \sum_j J_{ij}^{\text{inter}} \langle \hat{s}_x^{(j)} \rangle \quad (\text{C10})$$

As a first example, we may consider a periodic chain of equally spaced pairs where all pairs are identical and the mean-field shift arising from interactions between the pairs is J^{inter} . In this case, the diagonal ensemble expectation value can be calculated by solving the self-

consistent equation

$$\overline{\langle \hat{S}_x \rangle} = \frac{1}{2} \frac{\left(\Omega + J^{\text{inter}} \overline{\langle \hat{S}_x \rangle} \right)^2}{\left(\Omega + J^{\text{inter}} \overline{\langle \hat{S}_x \rangle} \right)^2 + j^2}. \quad (\text{C11})$$

Since the right-hand side of the equation only contains squares, the magnetization is still positive or zero. Therefore, for positive external fields Ω , the effective field is larger than the external field ($\Omega_i \geq \Omega$), leading to an enhanced spin locking effect. Consequently, mean-field leads to an increased magnetization compared to the case of independent pairs. For negative Ω , the external field is anti-aligned with the mean-field, and the resulting magnetization is decreased. Thus, the dependence of the magnetization as a function of field strength is asymmetric (see Figure 5 c). In conclusion, we can attribute the asymmetry to mean-field interaction between different pairs.

In order to model the disordered spin system realized experimentally, we apply the pair model to an ensemble of spins with randomly chosen positions. We cluster the spins i into pairs p in such a way that the sum over all pair distances is minimized. Naturally, the interaction

j_p of a pair p consisting of spins i and j is given by the interaction strength between the spins. The interaction strength J_{pq}^{inter} between pair p and q can be obtained from the strongest interaction J_{ij} where spin i is in pair p and j in q respectively. Now, we solve the system of self-consistent equations

$$\overline{\langle \hat{s}_x^p \rangle} = \frac{1}{2} \frac{\left(\Omega + \sum_q (J_{pq}^{\text{inter}} \overline{\langle \hat{s}_x^q \rangle}) \right)^2}{\left(\Omega + \sum_q (J_{pq}^{\text{inter}} \overline{\langle \hat{s}_x^q \rangle}) \right)^2 + j_p^2}. \quad (\text{C12})$$

The resulting magnetization curve obtained after disorder averaging (see blue line in Figure 5 d) closely resembles the exact diagonal ensemble prediction (orange line). Importantly, all qualitative features are captured, including a positive magnetization which is asymmetric with respect to the external field and shows a sharp cusp at zero field. The remaining discrepancy between the pair model and the exact solution, in particular the stronger asymmetry of the exact solution, can be attributed to clusters of spins containing more than two atoms where quantum fluctuations decrease the magnetization even further than predicted by the pair mean-field model.

-
- [1] P. Reimann, Physical Review Letters **101**, 190403 (2008).
- [2] J. M. Deutsch, Physical Review A **43**, 2046 (1991).
- [3] M. Srednicki, Journal of Physics A , 14 (1999).
- [4] M. Srednicki, Physical Review E **50**, 888 (1994).
- [5] M. Ueda, Nature Reviews Physics **2**, 669 (2020).
- [6] P. Peng, C. Yin, X. Huang, C. Ramanathan, and P. Cappellaro, Nature Physics **17**, 444 (2021).
- [7] M. Prüfer, P. Kunkel, H. Strobel, S. Lannig, D. Linemann, C.-M. Schmied, J. Berges, T. Gasenzer, and M. K. Oberthaler, Nature **563**, 217 (2018).
- [8] A. Rubio-Abadal, M. Ippoliti, S. Hollerith, D. Wei, J. Rui, S. Sondhi, V. Khemani, C. Gross, and I. Bloch, Physical Review X **10**, 021044 (2020).
- [9] C. Eigen, J. A. P. Glidden, R. Lopes, E. A. Cornell, R. P. Smith, and Z. Hadzibabic, Nature **563**, 221 (2018).
- [10] L. S. Martin, H. Zhou, N. T. Leitao, N. Maskara, O. Makarova, H. Gao, Q.-Z. Zhu, M. Park, M. Tyler, H. Park, S. Choi, and M. D. Lukin, Physical Review Letters **130**, 210403 (2023).
- [11] T. Langen, T. Gasenzer, and J. Schmiedmayer, Journal of Statistical Mechanics: Theory and Experiment **2016**, 064009 (2016).
- [12] D. M. Basko, I. L. Aleiner, and B. L. Altshuler, Annals of Physics **321**, 1126 (2006).
- [13] J. Z. Imbrie, Journal of Statistical Physics **163**, 998 (2016).
- [14] M. Serbyn, Z. Papić, and D. A. Abanin, Physical Review Letters **111**, 127201 (2013).
- [15] D. A. Huse, R. Nandkishore, and V. Oganesyan, Physical Review B **90**, 174202 (2014).
- [16] S. S. Kondov, W. R. McGehee, W. Xu, and B. DeMarco, Physical Review Letters **114**, 083002 (2015).
- [17] M. Schreiber, S. S. Hodgman, P. Bordia, H. P. Lüschen, M. H. Fischer, R. Vosk, E. Altman, U. Schneider, and I. Bloch, Science **349**, 842 (2015).
- [18] P. Bordia, H. P. Lüschen, S. S. Hodgman, M. Schreiber, I. Bloch, and U. Schneider, Physical Review Letters **116**, 140401 (2016).
- [19] J.-y. Choi, S. Hild, J. Zeiher, P. Schauß, A. Rubio-Abadal, T. Yefsah, V. Khemani, D. A. Huse, I. Bloch, and C. Gross, Science **352**, 1547 (2016).
- [20] A. M. Kaufman, M. E. Tai, A. Lukin, M. Rispoli, R. Schittko, P. M. Preiss, and M. Greiner, Science **353**, 794 (2016).
- [21] A. Lukin, M. Rispoli, R. Schittko, M. E. Tai, A. M. Kaufman, S. Choi, V. Khemani, J. Léonard, and M. Greiner, Science **364**, 256 (2019).
- [22] L. Wadleigh, N. Kowalski, and B. DeMarco, “Interacting Stark localization dynamics in a three-dimensional lattice Bose gas,” (2022), arXiv:2211.12336 [cond-mat].
- [23] J. Léonard, S. Kim, M. Rispoli, A. Lukin, R. Schittko, J. Kwan, E. Demler, D. Sels, and M. Greiner, “Signatures of bath-induced quantum avalanches in a many-body-localized system,” (2022), arXiv:2012.15270 [cond-mat, physics:quant-ph].
- [24] J. Smith, A. Lee, P. Richerme, B. Neyenhuis, P. W. Hess, P. Hauke, M. Heyl, D. A. Huse, and C. Monroe, Nature Physics **12**, 907 (2016).

- [25] G. Kucsko, S. Choi, J. Choi, P. C. Maurer, H. Zhou, R. Landig, H. Sumiya, S. Onoda, J. Isoya, F. Jelezko, E. Demler, N. Y. Yao, and M. D. Lukin, Physical Review Letters **121**, 023601 (2018).
- [26] J. Šuntajs, J. Bonča, T. Prosen, and L. Vidmar, Physical Review B **102**, 064207 (2020).
- [27] J. Šuntajs, J. Bonča, T. Prosen, and L. Vidmar, Physical Review E **102**, 062144 (2020).
- [28] P. Sierant and J. Zakrzewski, Physical Review B **105**, 224203 (2022).
- [29] I. Bloch, J. Dalibard, and W. Zwerger, Reviews of Modern Physics **80**, 885 (2008).
- [30] T. Esslinger, Annual Review of Condensed Matter Physics **1**, 129 (2010).
- [31] I. Bloch, J. Dalibard, and S. Nascimbène, Nature Physics **8**, 267 (2012).
- [32] C. Gross and I. Bloch, Science **357**, 995 (2017).
- [33] A. Browaeys and T. Lahaye, Nature Physics **16**, 132 (2020).
- [34] A. Browaeys and T. Lahaye, Nature Physics **16**, 132 (2020).
- [35] A. Signoles, T. Franz, R. F. Alves, M. Gärttner, S. Whitlock, G. Zürn, and M. Weidemüller, Physical Review X **11**, 011011 (2021).
- [36] S. Geier, N. Thaicharoen, C. Hainaut, T. Franz, A. Salzinger, A. Tebben, D. Grimshndl, G. Zürn, and M. Weidemüller, Science **374**, 1149 (2021).
- [37] A. Signoles, T. Franz, R. Ferracini Alves, M. Gärttner, S. Whitlock, G. Zürn, and M. Weidemüller, Physical Review X **11**, 011011 (2021).
- [38] P. Schultzen, T. Franz, S. Geier, A. Salzinger, A. Tebben, C. Hainaut, G. Zürn, M. Weidemüller, and M. Gärttner, Physical Review B **105**, L020201 (2022).
- [39] P. Schultzen, T. Franz, C. Hainaut, S. Geier, A. Salzinger, A. Tebben, G. Zürn, M. Gärttner, and M. Weidemüller, Physical Review B **105**, L100201 (2022).
- [40] H. Günther, *NMR Spectroscopy: Basic Principles, Concepts and Applications in Chemistry*, third, completely revised and updated edition ed. (Wiley-VCH, Weinheim, 2013).
- [41] R. Vosk and E. Altman, Physical Review Letters **110**, 067204 (2013).
- [42] D. Pekker, G. Refael, E. Altman, E. Demler, and V. Oganesyan, Physical Review X **4**, 011052 (2014).
- [43] R. Vasseur, A. C. Potter, and S. A. Parameswaran, Physical Review Letters **114**, 217201 (2015).
- [44] R. Vasseur, A. J. Friedman, S. A. Parameswaran, and A. C. Potter, Physical Review B **93**, 134207 (2016).
- [45] A. Braemer, T. Franz, M. Weidemüller, and M. Gärttner, Physical Review B **106**, 134212 (2022).
- [46] A. Morningstar, L. Colmenarez, V. Khemani, D. J. Luitz, and D. A. Huse, Physical Review B **105**, 174205 (2022).
- [47] D. M. Long, P. J. D. Crowley, V. Khemani, and A. Chandran, Physical Review Letters **131**, 106301 (2023).
- [48] A. Rajak, S. Suzuki, A. Dutta, and B. K. Chakrabarti, Philosophical Transactions of the Royal Society A: Mathematical, Physical and Engineering Sciences **381**, 20210417 (2022).
- [49] M. Bernaschi, I. G.-A. Pemartín, V. Martín-Mayor, and G. Parisi, “The Quantum Transition of the Two-Dimensional Ising Spin Glass: A Tale of Two Gaps,” (2023).
- [50] M. Ferreira-Cao, V. Gavryusev, T. Franz, R. F. Alves, A. Signoles, G. Zürn, and M. Weidemüller, Journal of Physics B: Atomic, Molecular and Optical Physics **53**, 084004 (2020).
- [51] H. Weimer, R. Löw, T. Pfau, and H. P. Büchler, Physical Review Letters **101**, 250601 (2008).
- [52] M. Gärttner, K. P. Heeg, T. Gasenzer, and J. Evers, Physical Review A **86**, 033422 (2012).
- [53] A. P. Orioli, A. Signoles, H. Wildhagen, G. Günter, J. Berges, S. Whitlock, and M. Weidemüller, Physical Review Letters **120**, 063601 (2018).
- [54] J. Schachenmayer, A. Pikovski, and A. M. Rey, Physical Review X **5**, 011022 (2015).
- [55] D. Pekker, G. Refael, E. Altman, E. Demler, and V. Oganesyan, Physical Review X **4**, 011052 (2014).
- [56] R. Vasseur, A. J. Friedman, S. A. Parameswaran, and A. C. Potter, Physical Review B **93**, 134207 (2016).
- [57] R. Vasseur, A. C. Potter, and S. A. Parameswaran, Physical Review Letters **114**, 217201 (2015).
- [58] R. Vosk and E. Altman, Physical Review Letters **110**, 067204 (2013).

6.2.1 Simple physical picture

To derive the qualitative behavior of the steady-state magnetization $\langle M(\Omega) \rangle$ with respect to external field Ω , we use a simple two-component model where each spin is either fully polarized or fully demagnetized. We assume that a spin's final state depends solely on the ratio of the strongest coupling J towards another spin and the strength of the external field Ω . If the field dominates, i.e. $|\Omega| > J$, the spin stays polarized as it is locked by the field. Conversely, if the coupling dominates, i.e. $|\Omega| < J$, then the interactions lead to depolarization and the spin loses its magnetization. Thus in this simplified model, the only quantity determining the steady-state magnetization is the distribution of relevant couplings $P(J)$:

$$\langle M(\Omega) \rangle = \frac{1}{2} \int_0^{|\Omega|} dJ P(J) \quad (6.1)$$

In the regime of weak disorder, it only natural to assume that the strongest relevant coupling for a spin is given by the coupling to its nearest neighbor. In contrast for strong disorder where we assume the pair model to describe the dynamics, the nearest neighbor coupling usually is not the relevant coupling! Instead, we need to consider the distribution of pair couplings $P_{pair}(J)$, i.e. the distribution of couplings that are shared by spins of the same pair.

To compute these coupling distributions analytically, we go to the limit of vanishing blockade radius, i.e. $r_b \rightarrow 0$, and assume that spins are distributed randomly with uniform density ρ in d dimensional space. Fixing some spin, this gives us for the number of spins in spherical shell of size r and width dr

$$w_u(r) dr = d\rho \Omega_d r^{d-1} dr = d\lambda (\lambda r)^{d-1} dr \quad (6.2)$$

where $\Omega_d = \frac{\pi^{d/2}}{\Gamma(n/2+1)}$ is the volume of a d -dimensional unit sphere and $\lambda^d = \rho \Omega_d$ is akin to the inverse mean distance between spins. We use this setup to compute both the distribution of nearest neighbor coupling $P_{NN}(J)$ and the distribution of pair couplings $P_{pair}(J)$ in the following sections.

6.2.1.1 Nearest-neighbor coupling distribution $P_{NN}(J)$

The distribution of the nearest neighbor couplings can be found using a simple ansatz [37]. Consider some fixed spin and the density of spin $w(r)$ at distance r . Then the probability $P_{NN}(r)$ of finding the nearest neighbor of that fixed spin at distance r should be proportional to both the probability of having a spin in that distance and the probability of having no closer neighbor. This gives us the following integral-equation

$$P_{NN}(r) = w(r) * \left(1 - \int_0^r dr' P_{NN}(r') \right) \quad (6.3)$$

which can be solved straight-forwardly by noting that it has the form $f' = -wf$ and using separation of variables. The solution reads:

$$P_{NN}(r) = w(r) \exp\left(-\int_0^r dr' w(r')\right) . \quad (6.4)$$

Plugging in the distance distribution for uniform spin density $w_u(r)$ (cf. Eq. 6.2) gives us a so-called Weibull distribution:

$$P_{NN}(r) = d\lambda^d r^{d-1} \exp(-\lambda^d r^d) \quad (6.5)$$

The change of variables also needs to transform the measure, i.e. we transform $P(r)dr \rightarrow P(J)dJ$

Changing variables from distance r to coupling $J = r^{-\alpha}$ yields

$$P_{NN}(J) = \beta \lambda^d J^{-\beta-1} \exp(-\lambda^d J^{-\beta}) \quad (6.6)$$

where $\beta = \frac{d}{\alpha}$.

6.2.1.2 Distribution of pair couplings $P_{pair}(J)$

We can derive the distribution of pair lengths in a similar fashion to Eq. 6.3. The key insight about the difference between a nearest neighbor and the partner of a pair in the RSRG sense is that the two partners of the pair are in some sense each other's partner. In contrast the "nearest neighbor" property does not need to be reflexive. Denoting the pair coupling distribution as $P_{pair}(J)$, we write down the respective integral equation, which is very similar to Eq. 6.3, except that the second factor gets squared because *both spins* may not be part of a smaller pair:

$$P_{pair}(r) = w(r) * \left(1 - \int_0^r dr' P_{pair}(r')\right)^2 \quad (6.7)$$

Eq. 6.8 was derived by a different method for $d = 3$ by former Master student Péter Kaposvári in his Master thesis [38].

Eq. 6.9 is called a log-logistic distribution.

This equation can be solved in the same way as Eq. 6.3 and yields:

$$P_{pair}(r) = \frac{w(r)}{\left(1 + \int_0^r dr' w(r')\right)^2} \quad (6.8)$$

Employing the distance distribution for uniform spin density $w_u(r)$ (cf. Eq. 6.2) again gives us the distribution of pair lengths for uniformly distributed spins:

$$P_{pair}(r) = \frac{d\lambda^d r^{d-1}}{(1 + \lambda^d r^d)^2} \quad (6.9)$$

Changing to distance r to coupling $J = r^{-\alpha}$ yields:

$$P_{pair}(J) = \frac{\beta \lambda^d J^{-\beta-1}}{\left(1 + \lambda^d J^{-\beta}\right)^2} \quad (6.10)$$

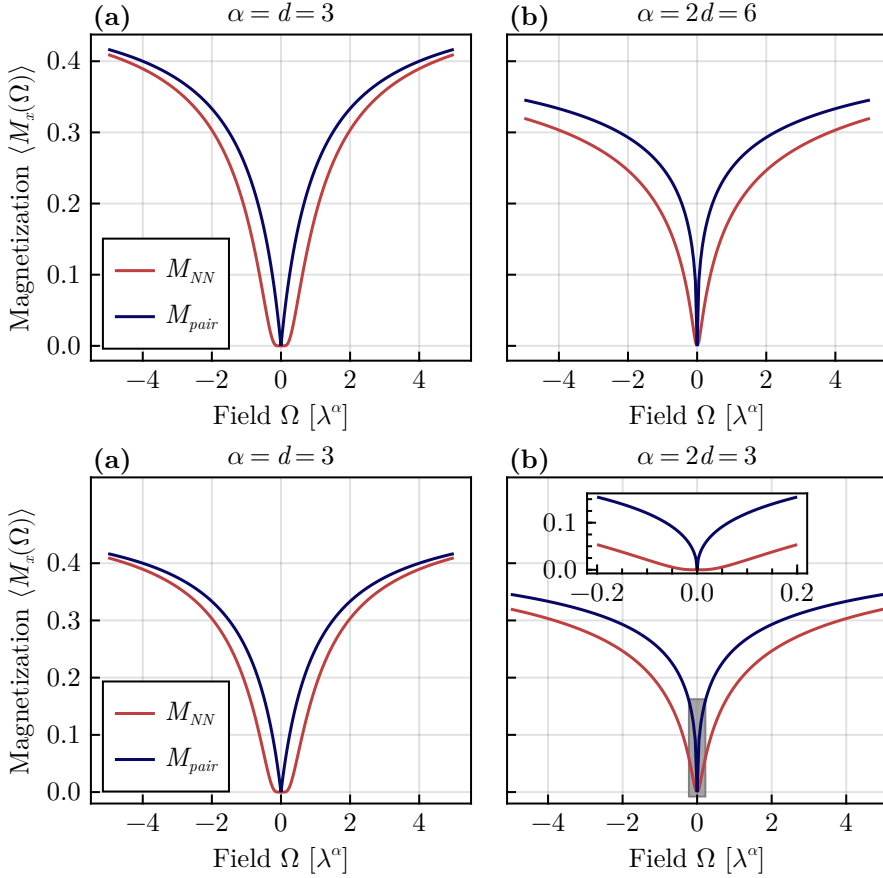


Figure 6.1: Steady-state magnetization curves of the simple two-component model using the same color scheme as Fig. 2 (d) and (e) of [C]. Parameters, α and d correspond to (a) Fig. 2 (b) Fig. 4. The inset show a zoom around $\Omega = 0$ to highlight the qualitative difference between the curves.

6.2.1.3 Analytical steady-state magnetization

With both the distribution of nearest-neighbor coupling $P_{NN}(J)$ (Eq. 6.6) and pair coupling distribution $P_{pair}(J)$ (Eq. 6.10), we can compute the steady-state magnetization of our simple model by using Eq. 6.1:

$$M_{NN}(\Omega) = \frac{1}{2} \int_0^{|\Omega|} dJ P_{NN}(J) = \frac{1}{2} \exp(-\lambda^d |\Omega|^{-\beta}) \quad (6.11)$$

$$M_{pair}(\Omega) = \frac{1}{2} \int_0^{|\Omega|} dJ P_{pair}(J) = \frac{1}{2 + 2\lambda^d |\Omega|^{-\beta}} \quad (6.12)$$

The resulting curves (cf. Fig. 6.1) show the same qualitative features as their counterparts in [C]. Thus, this simple model gives us insight in the key mechanism behind the qualitative change of the steady-state magnetization behavior: At weak field $|\Omega| \ll 1$, the magnetization is determined by the weakest interactions $J < |\Omega| \ll 1$ which stem from long distances $r \gg 1$. For nearest neighbors, the distribution of distances is suppressed exponentially $\propto \exp(-r^d)$ (cf. Eq. 6.5), which

creates the very smooth, round shape at weak field. Conversely, if the relevant lengths are given by the pairing procedure, the exponential suppression is weakened to an algebraic decay $\propto r^{-d-1}$. Intuitively, this is because while with increasing distance r the number of potential partners increases, it also becomes less likely that they are still available. This competition then leads to a much slower decay of the relevant lengths.

A few remarks: For $J \rightarrow 0$ this gives the limits:

$$\lim_{J \rightarrow 0} w_P(J) = \lim_{J \rightarrow 0} \beta \lambda^{-d} J^{\beta-1} = \begin{cases} 0 & d > \alpha \\ \beta \lambda^{-d} & d = \alpha \\ \infty & d < \alpha \end{cases} \quad (6.13)$$

The Cusp thus acquires the form:

$$\int_0^h dJ w_P(J) = \frac{1}{1 + \lambda^d J^{-\beta}} \Big|_0^h = \frac{1}{1 + \lambda^d h^{-\beta}} \quad (6.14)$$

Note: For $\alpha > d$ this predicted cusp gets ultra sharp as the first derivative diverges at 0!

7

OUTLOOK

7.1 OTOCS

define, some examples

A key prerequisite for measuring OTOCs is the ability to reverse the flow of time within the experiment. This was demonstrated for the specific Rydberg platform in Heidelberg in a very recent publication [F].

[G]

7.2 DISORDER-AVERAGED, EFFECTIVE TIME EVOLUTION

7.3 ?LIMITATIONS OF RSRG?

8

DISCUSSION

Part II

PERIODICALLY DRIVEN QUANTUM SYSTEMS WITH SPATIAL INHOMOGENEITY

9

CONCEPTS: TIME CRYSTALS IN FLOQUET SYSTEMS

9.1 FLOQUET SYSTEMS

9.2 THERMALIZATION IN FLOQUET SYSTEMS

9.3 TIME CRYSTALS

10

SPATIALLY-VARYING DRIVE

Metronome spin stabilizes time-crystalline dynamics

Niklas Euler^{1,2,*}, Adrian Braemer^{1,*}, Luca Benn,¹ and Martin Gärttner^{1,2,†}

¹Physikalisches Institut, Ruprecht-Karls-Universität Heidelberg, Im Neuenheimer Feld 226, 69120 Heidelberg, Germany

²Institut für Festkörpertheorie und Optik, Friedrich-Schiller-Universität Jena, Max-Wien-Platz 1, 07743 Jena, Germany



(Received 7 February 2024; revised 13 May 2024; accepted 14 May 2024; published 3 June 2024)

We investigate a disorder-free quantum Ising chain subject to a time-periodic drive that rotates each spin by an angle $\pi(1 - \epsilon_i)$. In case all spins experience the same deviation ϵ and the system is initialized in a fully polarized state, the dynamics is known to be time crystalline: the magnetization of the system exhibits period-doubled oscillations for timescales that grow exponentially with the length of the chain. In this work, we study the effect of a deviation ϵ that differs between spins. We find that reducing ϵ for a single spin drastically enhances the lifetime of spatiotemporal order, suggesting the name metronome spin. Employing perturbative arguments in an average Hamiltonian picture, we explain this observation for initial states with macroscopic bulk magnetization. Furthermore, in the case of random bit-string initial states, we report the enhancement of the lifetime of a topological edge mode, which can also be understood in the same picture. Finally, we discuss an altered geometry in which the metronome spin is not directly part of the chain, affecting the dynamics in different ways in the two scenarios considered. Our findings unveil the intricate dynamics that emerge in Floquet systems under the influence of a spatially varying drive, thereby uncovering new avenues for Floquet engineering.

DOI: [10.1103/PhysRevB.109.224301](https://doi.org/10.1103/PhysRevB.109.224301)

I. INTRODUCTION

For the longest time, stable physical phases of matter were thought to be a concept exclusive to equilibrium physics. However, with the pioneering work of Wilczek and Shapere [1,2], Watanabe and Oshikawa [3,4], and others, it became clear that out-of-equilibrium phases of matter are not only possible but also offer features beyond equilibrium phases [5,6]. One of the most prevalent categories of systems in which such phases have been demonstrated is Floquet setups, that is, periodically driven systems. Instead of heating up, they can display long-lived period-doubled spatiotemporal order with remarkable stability with respect to perturbations of the drive. Due to their discrete time-translation symmetry breaking, they have been dubbed Floquet time crystals or discrete time crystals (DTC) and have gained significant attention among the theoretical and experimental communities over the last decade [7,8].

Initially, many-body localization (MBL) was considered to be the main mechanism for stabilizing the long-lived dynamics [9–12]. However, over the years, a multitude of other processes have been shown to lead to time-crystalline behavior in different systems, including weakly broken symmetries [13], prethermalization [14–16], domain-wall confinement [17], among others [18–21]. Experimentally, time-crystalline dynamics has been observed on a variety of platforms, such as nitrogen vacancy centers [22–24], NMR systems [25–27], ultracold atoms [28,29], trapped ions [30], Rydberg atoms [31,32], and also superconducting qubits [33,34], to name a few. Most of the above time-crystal realizations demonstrate

long-lasting but finite spatiotemporal order, whereas some, e.g., the MBL DTC, lay claim to stability up to infinite times, even though this is controversially discussed by the community [16,35–38]. Numerical simulations have shown crystal lifetimes that exceed typical experimental timescales [5,33], thus it remains difficult to convincingly disprove infinitely long-lived order. Remarkably, two different realizations of absolutely stable [39] DTCs were recently reported [40,41]. These systems promise stability towards arbitrary perturbations, even if they break the discrete time-translation symmetry of the drive.

In most Floquet setups, drives are typically realized by periodically rotating all constituents by a fixed angle. One of the most striking features of time-crystalline order is the stability with respect to such a drive. The spatiotemporal structure is present not only at isolated points in parameter space (dictated by intrinsic symmetry of the interactions) but has also been observed for drives that systematically over- or undershoot the targeted rotation angles for the entire system by up to $\epsilon \lesssim 15\%$ in every drive period [30,33]. Contrary to the naive expectation, these errors do not accumulate and lead to rapid dephasing but are instead compensated for through the different stabilization mechanisms mentioned above. This defining characteristic of a DTC motivates the classification as an out-of-equilibrium phase of matter, as extended areas of stability can be identified with respect to the parameters of the system and drive, e.g., the interaction strength and the deviation of the driving angle [10,11]. Until recently [42], drives and perturbations have typically been considered to be spatially uniform, i.e., equal for all constituents of the system. The question of whether and how the stability of spatiotemporal order extends to regimes where parts of the system are driven at different values of ϵ remains largely unanswered. It is especially unclear whether this structure

*These authors contributed equally to this work.

†martin.gaerttner@uni-jena.de

is destabilized by a small subsystem driven at much higher values of ϵ , or whether a modest amount of particles driven at small ϵ can stabilize an otherwise unstable system.

To investigate the impact of the spatial dependence of the drive, we consider a disorder-free spin-1/2 chain with nearest-neighbor Ising interactions and periodic driving through numerical simulations. When initialized in a fully magnetized state, such a system's magnetization is known to exhibit period-doubled oscillations for a time growing exponentially with system size, which we will call lifetime [14,43–45]. Interestingly, by reducing the rotation angle deviation ϵ for a single spin of the chain, we find a drastic enhancement of the magnetization lifetime of the entire chain, as if the single spin was acting like a metronome that keeps the other spins on beat. We employ a time-averaged effective description, which allows us to explain the observed behavior with the help of symmetry arguments for the bulk of the chain.

Building on these results, we study how generic initial states behave in the presence of a metronome spin. Again, we find analogous lifetime enhancements in magnetization auto-correlators, however, only for the outermost spins stemming from the existence of a topological edge mode. Finally, we present a system geometry in which these two mechanisms can be clearly discerned. Our results offer new insights into how local perturbations in the chain can have a strong impact on the overall lifetime of large systems. This opens up new possibilities in the design and implementation of extended, (meta)stable phases of matter out of equilibrium, even in systems without disorder.

Following this introduction, we first give a more detailed description of the investigated system and the numerical methods used in Sec. II. The results for bulk and edge stabilization are presented in Sec. III and subsequently discussed in Sec. IV.

II. MODEL AND METHODS

We study the effects of spatially nonuniform Floquet driving through numerical simulation of a spin-1/2 chain. The Floquet sequence investigated in this work consists of two parts: in a first step, the spins interact through nearest-neighbor Ising couplings with open boundary conditions, as shown in Fig. 1(a). Second, the spins are subjected to unitary rotations by $\pi(1 - \epsilon_i)$, with i indicating the site index. We consider the case where the first spin is driven with $\epsilon_{i=1} = \epsilon'$ and all other spins with $\epsilon_{i>1} = \epsilon$ [Fig. 1(b)]. Thus, this configuration represents a uniformly driven chain with a local perturbation at one boundary site, obeying a spin-flip symmetry in the absence of z fields. One cycle of this time-periodic evolution is captured by the Hamiltonian

$$H = \begin{cases} H_{\text{int}} = \sum_{i=1}^{L-1} J_{i,i+1} s_z^i s_z^{i+1} + \sum_{i=1}^L h_i s_z^i, & 0 \leq t \leq t_1 \\ H_x = \sum_{i=1}^L (1 - \epsilon_i) s_x^i, & t_1 < t < t_1 + \pi =: T \end{cases}, \quad (1)$$

with $s_{\{x,y,z\}}^i = \sigma_{\{x,y,z\}}^i / 2$ being the single-spin operators. The evolution governed by this Hamiltonian induces (imperfect)

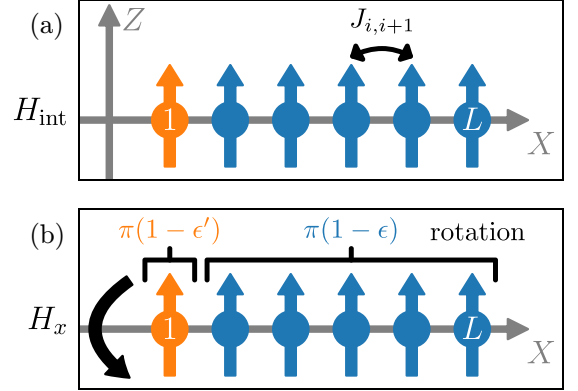


FIG. 1. An illustration of the two-step Floquet cycle of the one-dimensional (1D) system considered in this work. (a) The interaction phase of the cycle given by an Ising Hamiltonian with nearest-neighbor couplings. (b) The driving phase of the Floquet cycle, realized through single-spin s_x rotations. While the majority of the spins in the chain (here drawn in blue) is subjected to imperfect flips around the x axis given by $\pi(1 - \epsilon)$, one spin at site index $i = 1$ has a differing drive-angle deviation $\epsilon_{i=1} = \epsilon'$, resulting in $\pi(1 - \epsilon')$ rotations.

periodic flipping of the magnetization of the spin chain with period $2T$, which is twice the original period of the Hamiltonian. Here, we are especially interested in how decreasing the deviation of the rotation angle, ϵ' , for a single spin, which we call the metronome spin, affects the dynamics of spatially distant spins at late times. While we set $h_i = 0$ in the main text, we also study chains with random fields and disordered couplings in Appendix A and disorder-free chains with the metronome in the center, $\epsilon_{i=\frac{L+1}{2}} = \epsilon'$, in Appendix B.

The stroboscopic evolution of the system, that is, evaluated only once at the beginning of every cycle, is given by the Floquet evolution operator U_F , which propagates the system through one cycle of the Floquet sequence. To gain a better understanding of the stroboscopic dynamics, one would like to find a time-independent Floquet Hamiltonian H_F that generates the Floquet time evolution operator, such that

$$U_F = e^{-iH_x\pi} e^{-iH_{\text{int}}t_1} =: e^{-iH_F T}. \quad (2)$$

In most cases, there is no straightforward way to obtain H_F analytically, but one can expand H_F in the so-called Magnus series [46,47]. By construction, H_F is guaranteed to be Hermitian at all orders. We give the first two terms of the expansion,

$$H_F = H_F^{(0)} + H_F^{(1)} + \dots, \quad (3a)$$

$$H_F^{(0)} = \frac{1}{T} \int_0^T dt H(t), \quad (3b)$$

$$H_F^{(1)} = \frac{1}{2Ti} \int_0^T dt \int_0^t dt' [H(t), H(t')], \quad (3c)$$

with the first term $H_F^{(0)}$ often being referred to as the average Hamiltonian.

By computing the average over one period, one has to include the large $\pi(1 - \epsilon_i)s_x^i$ rotations in $H_F^{(0)}$,

$$H_{F,1P}^{(0)} = \frac{1}{t_1 + \pi} \left[t_1 \left(\sum_{i=1}^{L-1} J_{i,i+1} s_z^i s_z^{i+1} + \sum_{i=1}^L h_i s_z^i \right) + \pi \sum_{i=1}^L (1 - \epsilon_i) s_x^i \right], \quad (4)$$

which is detrimental to the convergence of the Magnus series [47]. As stated earlier, the magnetization-flipping dynamics is period doubled with respect to the time-dependent Hamiltonian. Therefore, if averaged over two periods, one not only mostly cancels the spin rotations but also averages out any random y/z fields. The newly obtained two-period averaged effective Hamiltonian has the form of a transverse-field Ising model (TFIM),

$$H_{F,2P}^{(0)} = \frac{1}{t_1 + \pi} \left(t_1 \sum_{i=1}^{L-1} J_{i,i+1} s_z^i s_z^{i+1} - \pi \sum_{i=1}^L \epsilon_i s_x^i \right), \quad (5)$$

hereafter only referred to as $H_F^{(0)}$. Alternatively, this Hamiltonian can also be derived by applying a toggling-frame transformation and subsequently taking the average over one cycle [8]. This effective description retains the spin-flip symmetry present in the original time-dependent model.

III. RESULTS

In this section, we investigate numerically the lifetimes of various multispin and single-spin observables at stroboscopic times. We employ exact evolution according to the full Floquet unitary given in Eq. (2) in addition to the effective evolution with an TFIM as derived in Eq. (5) for comparison. Here, we study systems with $L = 14$ spins and set $J_{ij} := J = 1$, $h_i = 0$, $\epsilon = 0.1$, $t_1 = 1$, and $\epsilon' = 10^{-5}$, if not otherwise specified.

A. Bulk lifetime enhancement for polarized initial states

We start by considering the dynamics of the global magnetization $\langle \sum_i \sigma_z^i \rangle / L$ for a polarized initial state $|\Psi_{\text{init}}\rangle = |\uparrow \dots \uparrow\rangle$, as shown on a logarithmic time axis in Fig. 2. Only even period numbers are probed, so that the underlying spin-flipping dynamics is hidden in the shown simulation. The magnetization shows an initial decline that lasts $\approx 10^2$ periods of the drive, largely independent of the presence of a metronome spin. Subsequently, for both with and without metronome spin we observe slow oscillations of the magnetization, which manifest themselves as extended plateaus of nonvanishing magnetization due to the log-linear axes choice in Fig. 2. The macroscopic magnetization indicates that large parts of the chain retain some of its initial polarization. The duration of this plateau is strongly dependent on the angle deviation of the metronome spin drive ϵ' and, in the case of an active metronome spin, lasts $\approx 10^7$ periods instead of $\approx 10^3$ periods without the metronome. The single-spin magnetization of the metronome spin, $\langle \sigma_z^1 \rangle$, as shown on the right axis of Fig. 2, qualitatively demonstrates the same behavior and has a lifetime similar to that of $\langle \sum_i \sigma_z^i \rangle / L$. For all data taken,

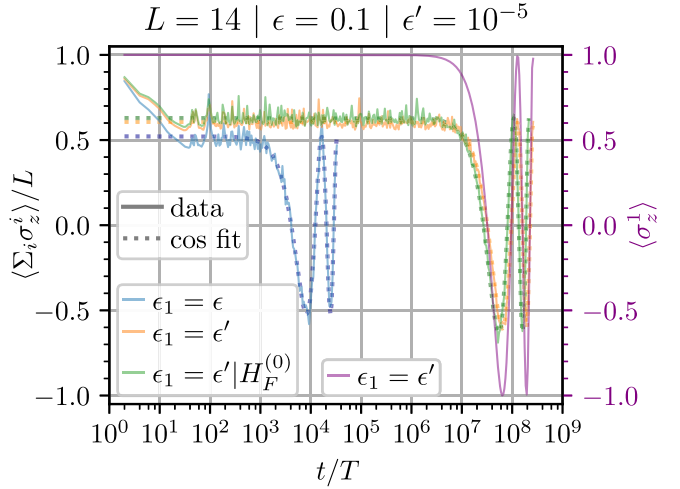


FIG. 2. The global z magnetization of the spin chain of length $L = 14$ starting in a fully polarized state subjected to different driving schemes. We show the exact stroboscopic dynamics of the chain at even period numbers with and without a metronome spin at one boundary site and the average Hamiltonian given in Eq. (5). Configurations that include a metronome spin display a lifetime enhancement of several orders of magnitude. All data are well described through numerical cosine fits. On the second axis (in purple font) the single-spin magnetization of the metronome spin itself is displayed. The lifetime of the magnetization of the metronome coincides with the lifetime of the total magnetization. For better visibility, only the first two oscillation cycles are plotted for each curve.

the evolution under the two-period average of the Floquet Hamiltonian $H_F^{(0)}$ is in satisfactory agreement with the full Floquet evolution (the green line shows this for the case with metronome spin), indicating that it is a sufficiently good description of the full stroboscopic evolution. Therefore, we can safely focus on the simpler time-independent $H_F^{(0)}$ to better understand the observed behavior.

Our chosen polarized initial state is the superposition of the two lowest-energy eigenstates of $H_F^{(0)}$ which, for $\epsilon \ll J$, are well approximated by the two parity states, $|\pm\rangle_L = (|\uparrow \dots \uparrow\rangle \pm |\downarrow \dots \downarrow\rangle)/\sqrt{2}$. At finite ϵ , states with domain-wall excitations are admixed (domain-wall dressing), leading to the observed initial fast decay. The energy gap between the two lowest-lying states is $\propto \epsilon^L$ in the uniform case by a perturbative argument, considering that all L spins are being flipped through off-resonant coupling to excited states. Thus, the gap vanishes in the limit $L \rightarrow \infty$, making the two states degenerate. In the case of $L = 14$ presented here, the gap is still finite and leads to slow Rabi oscillations of period T_R between the two polarized states, which explains the observed behavior. The data show good agreement with the numerical cosine fits $\propto \cos(2\pi t/T_R)$, as also plotted in Fig. 2, with $T_R(\epsilon_1 = \epsilon) = (1.641 \pm 0.006)10^4 T$ and $T_R(\epsilon_1 = \epsilon') = (1.281 \pm 0.004)10^8 T$. This difference in the length of the period of four orders of magnitude is expected in the average Hamiltonian picture, as the energy gap given above is inversely proportional to the Rabi-oscillation period $T_R \propto \epsilon^{-L}$. By endowment of one spin with reduced ϵ' , one obtains

$$T_R \propto \epsilon^{-L+1} (\epsilon')^{-1}, \quad (6)$$

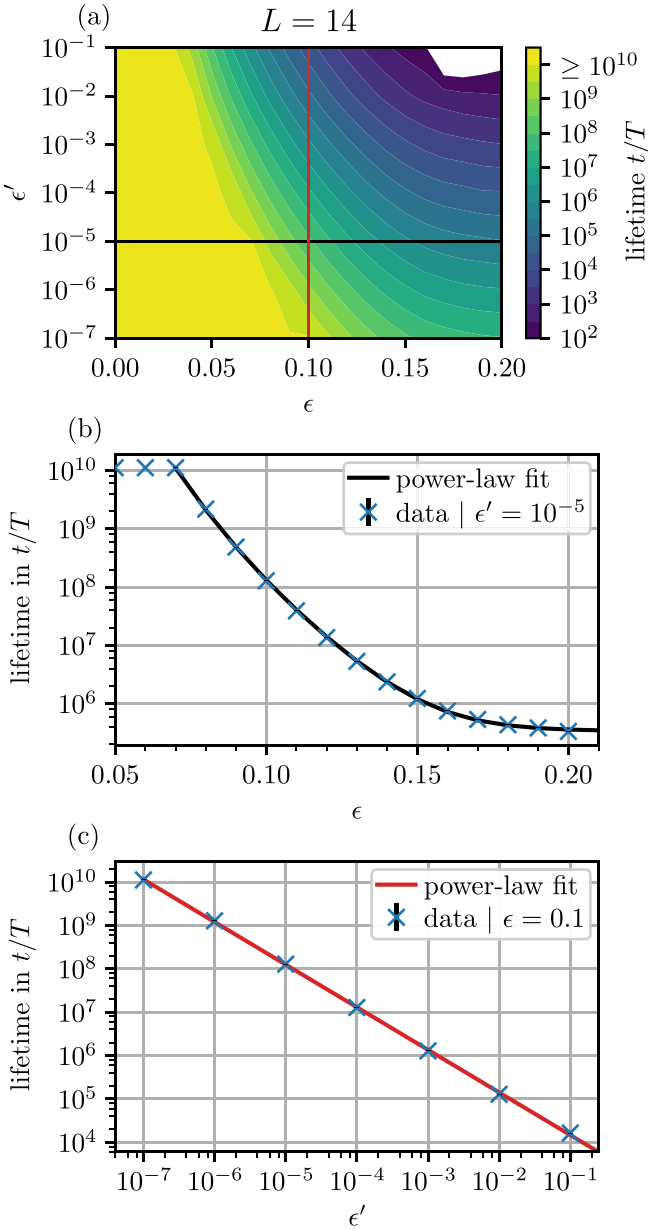


FIG. 3. The lifetime of the global z magnetization $\langle \sum_i \sigma_z^i \rangle / L$ for a range of drive deviation parameters ϵ and ϵ' including a metronome spin on one boundary site is shown in (a). (b) A horizontal cut through this plane at fixed $\epsilon' = 10^{-5}$. (c) A vertical cut at fixed $\epsilon = 0.1$, as indicated by the black and red lines in (a), respectively. All data points have been obtained through cosine fits, as shown in Fig. 2. Lifetimes above $t = 10^{10}T$ and below $t = 10^2T$ cannot be adequately resolved and are therefore exempt from the fit.

which yields the observed difference for the values used of $\epsilon = 0.1$ and $\epsilon' = 10^{-5}$.

Next, we systematically investigate the dependence of the global magnetization lifetime T_R on the deviations of the drive angle. For this, we repeat the procedure explained above for a number of combinations of the values of ϵ and ϵ' . The results are shown in Fig. 3(a), where we have probed a wide regime of drive parameters. At small ϵ , we observe lifetimes that exceed the resolved duration of 10^{10} Floquet cycles (yellow region). For fixed $\epsilon = 0.1$, we find that T_R is approximately inversely

proportional to ϵ' , $T_R \propto (\epsilon')^\alpha$ with $\alpha = -0.982 \pm 0.007$, as shown in Fig. 3(b), which is consistent with the reasoning presented in Eq. (6). For fixed $\epsilon' = 10^{-5}$, the recorded lifetimes follow a power law with offset, $T_R/T \approx a\epsilon^\beta + (3.35 \pm 0.09)10^5$, with $\beta = -12.29 \pm 0.03$. This value of β roughly agrees with the expectation $\beta = -13$ implied by Eq. (6). However, the observed convergence to a nonzero lifetime in the limit of large ϵ is not predicted by this perturbative picture [cf. Eq. (6)].

This behavior can be understood by taking $\epsilon' \rightarrow 0$. In this limit, the dynamics of the metronome spin effectively decouple from the bulk of the chain, since the metronome cannot leave the manifold of $\{|\uparrow\rangle, |\downarrow\rangle\}$, alternating between the two states in every Floquet cycle. One can now write down a Hamiltonian restricted to the bulk of the chain, where the coupling between the metronome and its neighboring spin, $s_z^1 s_z^2$, can be replaced by an effective field on the second spin of the chain,

$$H_{F,\text{bulk}}^{(0)} = \frac{1}{T} \left(\tilde{h} s_z^2 + t_1 \sum_{i=2}^{L-1} J_{i,i+1} s_z^i s_z^{i+1} - \pi \sum_{i=2}^L \epsilon_i s_x^i \right). \quad (7)$$

The new field term effectively breaks the spin-flip symmetry of the original Hamiltonian $H_F^{(0)}$ in the bulk and thus introduces an energy gap between the two polarized states. Therefore, the prepared polarized state is no longer the superposition of the two lowest-energy eigenstates but, rather, very close to the lowest eigenstate of $H_{F,\text{bulk}}^{(0)}$, resulting in a stable magnetization plateau. For cases where $\epsilon' \ll 1$ the metronome spin stays close to the $\{|\uparrow\rangle, |\downarrow\rangle\}$ manifold for extended periods of time before it and, subsequently, the rest of the chain dephases. However, in the large ϵ limit, large parts of the chain farther away from the metronome lose their magnetization much earlier due to domain-wall excitations. Still, since the metronome is largely decoupled in its dynamic from the rest of the chain, it retains nonvanishing magnetization even at late times, keeping the magnetization plateau alive, albeit at a lower value $\langle \sum_i \sigma_z^i \rangle / L \sim \mathcal{O}(1/L)$. This explains the observed saturation behavior in the lifetime dependence at large ϵ in Fig. 3(b).

B. Edge-mode enhancement for random bit-string initial states

Next, we investigate how the introduction of a metronome affects the dynamics of different initial states beyond the fully polarized case. To this end, we subject an ensemble of random bit-string states, i.e., states where every spin is either $|\uparrow\rangle$ or $|\downarrow\rangle$ chosen randomly, to the Floquet sequence given in Eq. (1). As the magnetization of these states vanishes on average, we instead consider local magnetization autocorrelators in the rotating frame, $\langle \sigma_z^i(0) \sigma_z^i(t/T) \rangle (-1)^{\lfloor t/T \rfloor} =: Z_i$. Three autocorrelators of selected spin sites, averaged over a set of 500 bit-string initial states, are shown in Fig. 4. The three panels show the autocorrelators of the metronome spin on the site $i = 1$ in Fig. 4(a), of a spin in the bulk of the chain on site $i = 8$ in Fig. 4(b), and at the other chain boundary on site $i = 14$ in Fig. 4(c).

First, the results for the autocorrelator of the metronome spin itself are in line with the results for the metronome single-spin magnetization in Fig. 2 (right axis). The

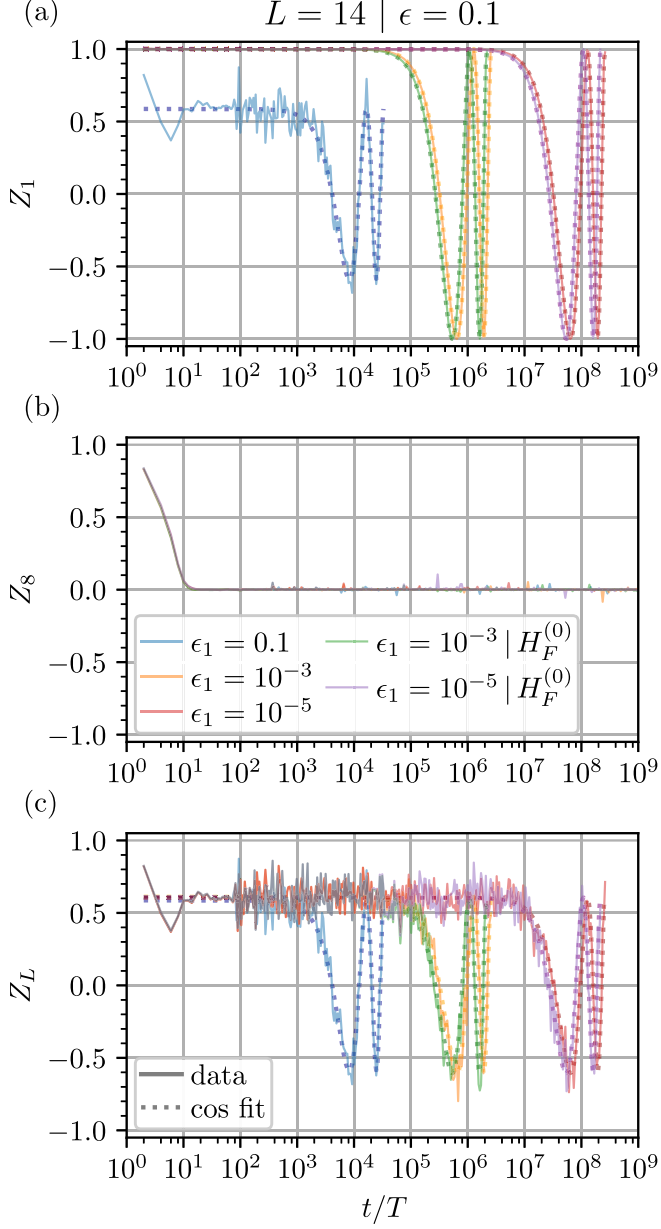


FIG. 4. The z -magnetization autocorrelators Z_i averaged over 500 random initial bit-string states for three different sites in a chain of $L = 14$ spins with open boundary conditions. (a) The autocorrelator for the metronome spin at the left boundary of the chain at site index $i = 1$. (b) The autocorrelator for a spin in the middle of the chain at site index $i = 8$. (c) The autocorrelator for the right boundary site with $i = 14$. We observe a long-lived edge mode with clear lifetime enhancement through the introduction of a metronome spin.

autocorrelator oscillates with full amplitude, $-1 \leq Z_1 \leq 1$, even at late times. Second, for sites in the bulk, we observe a rapid decline in the autocorrelator to zero, regardless of the value of ϵ' . Third, we see a plateau of the autocorrelator of the opposite boundary site analogous to the dynamics of the metronome site itself, as presented in Fig. 4(c). These characteristics are consistent with those of a strong π mode (SPM) [48]. This phase encompasses rapid bulk heating, but also robust period-doubled edge modes, and is closely related

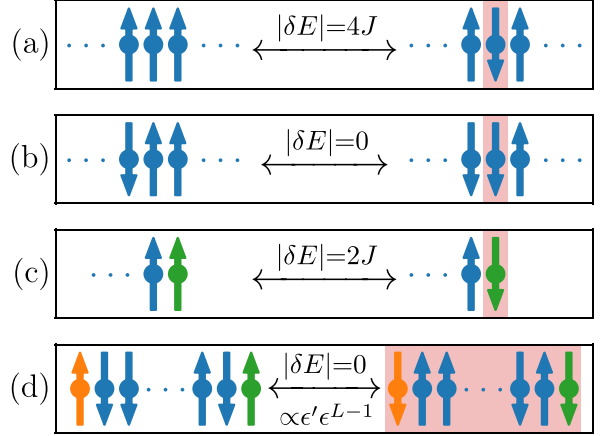


FIG. 5. A visual summary of the different spin-flipping processes and their associated energy differences. The spins in the bulk are colored blue, whereas the metronome is colored orange, and the right edge spin is colored green. Flipped spins are highlighted with a red background. (a) The creation or annihilation of two domain walls in the bulk of the chain. If the two adjacent spins are aligned, flipping the central spin results in an energy difference of $|\delta E| = 4J$. (b) The free propagation of a domain wall. If the two adjacent spins of a central spin are antialigned, flipping the central spin is energetically degenerate, i.e., $|\delta E| = 0$. Therefore, domain walls can propagate freely along the chain, utilizing this mechanism to iteratively flip the next spin at the domain wall. (c) The flipping of the edge spin. Flipping an edge spin always results in an energy difference of $|\delta E| = 2J$, half of the bulk value, since it is coupled to only one neighboring spin. Consequently, the edge spins cannot participate in the domain-wall dynamics shown in (b). The resulting coupling for the first three processes is $\propto \epsilon$. (d) The flipping of the entire chain. Flipping all spins together preserves the domain-wall structure of the chain and thus does not have an associated energy difference. This resonant process flips the edge spins at an effective rate $\propto \epsilon' \epsilon^{L-1}$.

to a symmetry-protected topological (SPT) phase [48–51]. This phase has recently been observed in the system under investigation [52]. Our data show a clear enhancement of the lifetime of the autocorrelator at the boundary sites, Z_L , through the introduction of the metronome spin, even though the two boundaries are separated by $L - 2 = 12$ spins coupled only through nearest-neighbor interactions. In particular, it is not necessary to apply the stabilized drive directly to one of the two edge modes. Additional simulations of a chain with a central metronome spin reveal a similar behavior with edge-mode lifetime enhancement. More details on this additional investigation can be found in the Appendix B.

This behavior can be understood by considering the spectral structure of the average Hamiltonian $H_F^{(0)}$, which we motivate in the following by a dynamical perspective. In the regime of small transverse field, the spectrum of the TFIM approximately decomposes into blocks of states with equal number of domain walls, i.e., adjacent spins pointing in opposite direction. The interaction term yields an energy difference of $2J$ per domain wall between these blocks. The action of the field term is twofold in this view: it causes spin flips, which, in the bulk of the chain, can either create or annihilate two adjacent domain walls [see Fig. 5(a)] or move an existing

domain wall by one site [see Fig. 5(b)]. The former changes the number of domain walls by ± 2 and is thus off resonant, i.e., comes at an energy cost. However, the latter leaves the total number of domain walls invariant and thus is resonant, i.e., domain walls can propagate freely within the bulk. At the edges of the chain, any spin flip always creates or annihilates a single domain wall. This observation is at the heart of the topological protection of the edge spins: Flipping an edge spin is the only process that changes the number of domain walls by an odd amount, and thus is always off resonant, unless both edge spins are flipped. This picture is analogous to previous work [53], in which the authors describe how Majorana fermions are protected on the boundary sites due to an approximate conservation law. One process that is always resonant and simultaneously flips both edge spins is flipping all spins [see Fig. 5(d)] as it corresponds to the global symmetry of the system. All other processes that alter the edge spins are strongly suppressed, because after diagonalizing the resonant domain-wall dynamics in the bulk, the resulting eigenstates do not feature any other resonant transitions. This leads to the observed oscillations with frequency $\propto \epsilon' \epsilon^{L-1}$ as in the case of the fully polarized initial state.

To better illustrate that last point, we translate the dynamical perspective above onto the static eigenstates of the average Hamiltonian $H_F^{(0)}$. Starting with the global parity symmetry, all eigenstates $|\phi_{\pm}\rangle \propto |\phi\rangle \pm |\bar{\phi}\rangle$ are also eigenstates of the parity operator and thus are an equal superposition of a state $|\phi\rangle$ and its spin-flipped counterpart $|\bar{\phi}\rangle$. For weak field $\epsilon \ll J$, the domain-wall number is approximately conserved, which means that each eigenstate predominantly consists of states from the same domain-wall-number sector with only minor admixtures from adjacent sectors. The observation from the dynamical viewpoint in the previous paragraph, namely that domain walls can propagate freely, here means that within the same domain-wall-number sector, the location of domain walls is ill-defined and the eigenstates are a superposition of all possible placements (see Fig. 6).

With this characterization of the eigenstates, the explanation of the observations made above is straightforward (see sketch Fig. 6). Taking a bit-string initial state and expanding it in the eigenstate basis, we find it to overlap with many different eigenstates from the same sector of the domain-wall-number operator. These eigenstates dephase rapidly $\propto \mathcal{O}(\epsilon)$ and lead to the decay of autocorrelators in the bulk, as seen in Fig. 4(b). By contrast, the edge spins can only change due to the dephasing between the parity sectors, which happens $\propto \mathcal{O}(\epsilon' \epsilon^{L-1})$. Since the splitting is identical for all components, this leads to the long coherent oscillations seen at late times in Fig. 4(a) and 4(c). The initial decay of the edge spin opposite to the metronome [see Fig. 4(c)] is caused by the admixture of wave-function components with a different number of domain walls. The observation that a nonzero number of domain walls will lead to rapid bulk dephasing and thus only a polarized initial state can show long-range order is in line with an earlier study [54]. There, the authors describe a prethermal phase, which they claim can generally only be realized in long-range interacting systems in one dimension. In short-range interacting systems, only the polarized (zero-temperature) initial state displays long-lived spatiotemporal order, as it is the only state with vanishing domain-wall number.

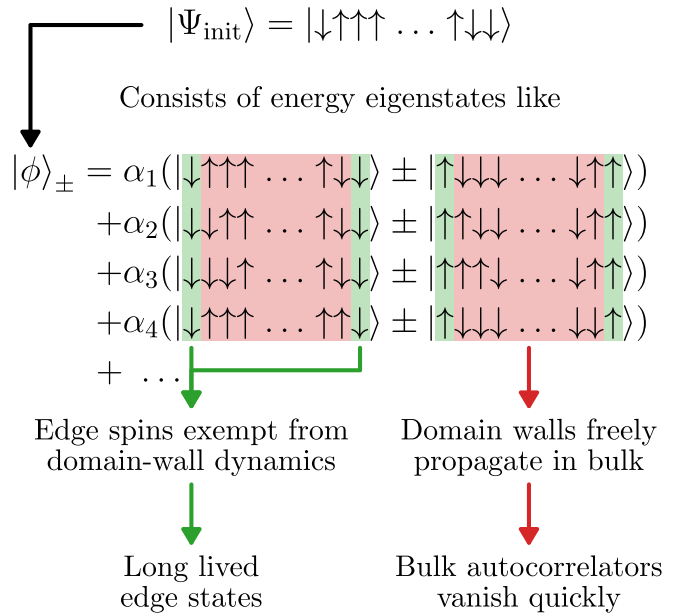


FIG. 6. An illustration of the topological edge-mode protection mechanism. The system is initially prepared in a random bit-string state $|\Psi_{\text{init}}\rangle$. Expanded in the energy eigenbasis of the average Hamiltonian $H_F^{(0)}$, the initial state has overlap with many eigenstate pairs $|\phi\rangle_{\pm}$ with the same number of domain walls. These eigenstate pairs each comprise a superposition of all possible domain wall placements since domain walls can move freely (highlighted in red). The dephasing between eigenstate pairs leads to the vanishing autocorrelators in the bulk. However, since domain walls cannot propagate through the edges, edge spins (marked in green) are protected from the domain-wall dynamics. Instead, they show long coherent oscillations due to the exponentially small energy gap between the parity sectors.

C. Adapted model with external metronome spin

To clearly separate the two described stabilization mechanisms introduced in Secs. III A and III B, we modify the geometry of the model as shown in Fig. 7(a). Instead of attaching the metronome spin to one end of the chain, as previously shown in Fig. 1, the metronome is coupled to the central spin, which itself is still coupled to its two neighbors in the chain. Thus, the two boundary spins are driven in the same way, and they are connected by a direct line of not actively stabilized spins in the bulk. By the reasoning outlined in Sec. III A, one expects similar results for polarized initial states compared to the standard layout of Fig. 1, as the argument relating to the effective symmetry breaking in the bulk still holds. However, the new configuration includes three edges and one central spin coupled to three neighbors, one of which being the metronome spin. One important conceptual difference to the linear configuration is that here the number of domain walls in the main part of the chain is less strictly conserved. This results in a much weaker edge protection, as the coupling between adjacent domain wall sectors is no longer strongly suppressed.

To test these hypotheses, we compute the z -magnetization autocorrelators of a boundary site, Z_L , and of the new metronome site, Z_m , with the results given in Figs. 7(b), 7(c). The observed lifetime behavior is in full agreement with

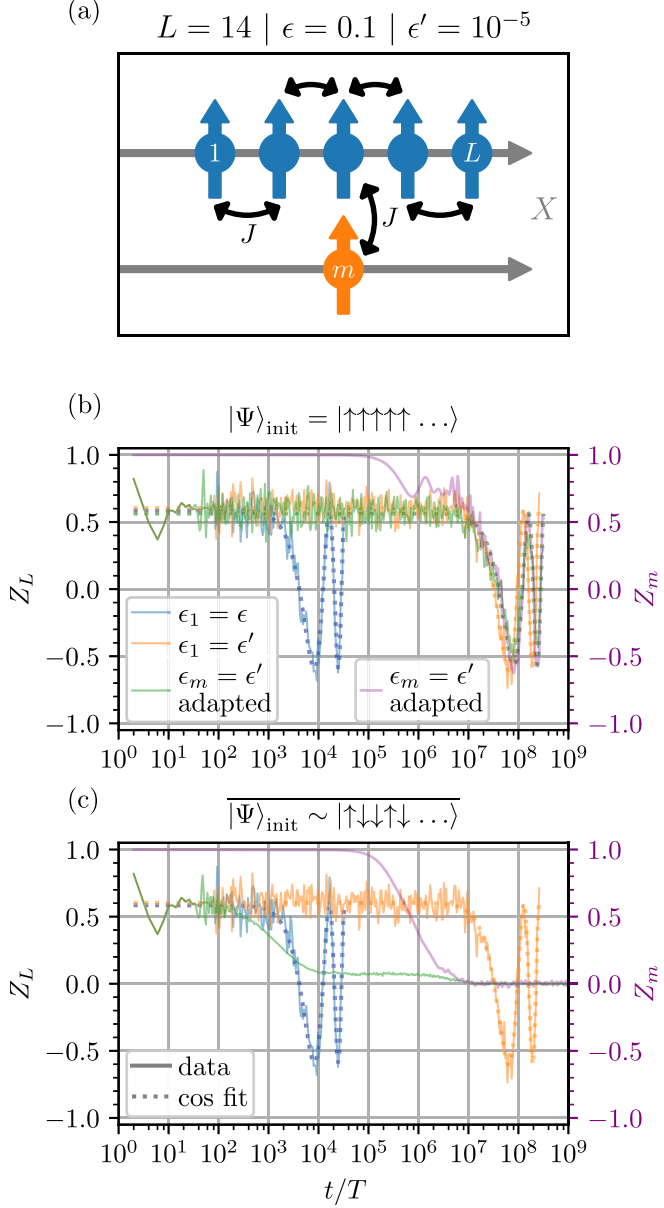


FIG. 7. The setup of the adapted system with $L - 1$ spins in a chain with an additional externally coupled metronome spin attached to the center. (a) A schematic visualization of the adapted geometry. The lifetimes of the boundary-site z -magnetization autocorrelators Z_L are shown in the next two panels for different initial states. (b) The autocorrelator of the polarized initial state. The blue and orange lines show the results for the case without metronome spin and with a metronome spin in the chain, respectively, for reference. Both configurations with a metronome display similar lifetime enhancements of the autocorrelator. (c) The autocorrelator averaged over 500 random initial bit-string states. The adapted system shows a much earlier decay of the autocorrelators compared to the configuration with the metronome spin in the chain and retains only a remnant of the original magnetization for the duration of the metronome lifetime. On the second axis in (b) and (c) (in purple font) the magnetization autocorrelator Z_m of the metronome spin itself in the adapted setup is displayed.

the previous predictions. In the fully polarized case, we see analogous results, whereas for random bit-string states, the

averaged autocorrelator of the edge spin (green curve) decreases rapidly to an intermediate plateau before vanishing completely. The timescale of the larger first decay is comparable to the lifetime of the nonstabilized chain ($t/T \approx 10^3$), and the second late-time decay coincides with the dephasing of the metronome spin. The initial decay stems from the multitude of different couplings between domain-wall sectors and the small remaining autocorrelations are protected by the spin-flip parity that is broken on timescales $\ll \epsilon'$ where the metronome is still fully polarized.

IV. CONCLUSION

In this work, we have shown that near-resonant driving of a single spin can significantly increase the lifetime of long-range order in periodically driven systems. In particular, the stabilization is not based on disorder-induced MBL; instead, we have identified two distinct mechanisms that lead to long-lived bulk and edge spins, respectively. For polarized states, an argument concerning the breaking of spin-flip symmetry was found to explain the increased bulk magnetization lifetimes. Subsequent studies revealed a lifetime enhancement of stable oscillations on the boundary spins in arbitrary bit-string initial states. We argued that the reason for the slowed edge-mode decay is that the metronome spin leads to a suppression of resonant higher-order processes. Finally, we discussed another setup with external stabilization to the chain and thus no edge-mode enhancement to clearly highlight the two different mechanisms identified before.

Thus, our work introduces novel stabilization mechanisms suitable for ordered and, in particular, finite-size systems. The bulk-stabilization argument relies on the effective symmetry breaking introduced through one metronome spin, which is not affected by the length of the chain. Similarly, the energy offset of flipping edge spins compared to the bulk is linked to open boundary conditions, leading to enhancement of stable oscillation even for short chains. Therefore, both processes enable arbitrarily long-lived oscillations without taking the thermodynamic limit.

We point out that the stabilization mechanism of the model is not based on the Hamiltonian being integrable. The core concept is linked to the underlying approximate conservation of the domain-wall number and the spin-flip symmetry, the latter of which is broken by the metronome in the bulk of the chain. We expect to find similar results in other spin systems as long as these conditions are met. To corroborate this statement, we have studied the same model as in Eq. (1), but added next-nearest-neighbor interactions, $\sim J_{i,i+2} s_z^i s_z^{i+2}$, which break the integrability of the Hamiltonian (cf. Appendix C). As expected, we find that decreasing ϵ for one of the spins yields lifetime enhancements analogous to the regular TFIM model, which encourages further study of applications in other models.

One potential future extension of this work is the study of two- and three-dimensional setups. The existence of MBL and thus disorder-stabilized DTC in these systems has been the subject of ongoing debate in recent years, which makes the study of alternative stabilization mechanisms an interesting direction. Moreover, the search for analogous stabilization mechanisms in other paradigmatic spin models, such as the

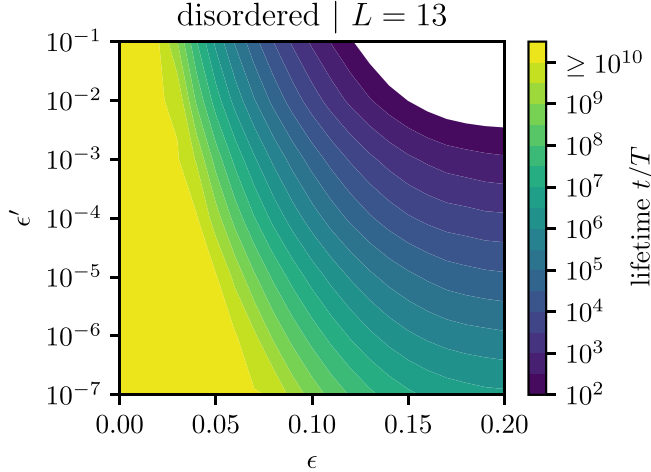


FIG. 8. The disorder-averaged lifetimes of the global chain z magnetization with $N = 13$ spins, starting in the fully polarized initial state. The data were obtained by numerical sigmoid fits. Lifetimes above $\geq 10^{10}T$ and below $\leq 10^2T$ cannot be adequately resolved.

Heisenberg XX and XXZ models, could lead to new insights into out-of-equilibrium dynamics in quantum many-body systems.

ACKNOWLEDGMENTS

We thank Matthias Weidmüller, Roderich Mössner, Sebastian Geier, and Razvan Gurau for fruitful discussions. This work is supported by the Deutsche Forschungsgemeinschaft (DFG, German Research Foundation) under Germany's Excellence Strategy EXC2181/1-390900948 (the Heidelberg STRUCTURES Excellence Cluster) and within the Collaborative Research Center SFB1225 (ISOQUANT). The authors acknowledge support by the state of Baden-Württemberg through bwHPC and the DFG through Grant No. INST 40/575-1 FUGG (Helix and JUSTUS2 clusters). For the numerical work, we used the JULIA programming language [55].

APPENDIX A: DISORDERED COUPLINGS AND FIELDS

The stabilization mechanism proposed in Sec. IIIA is not based on the presence of disorder in the system. To study the interplay of disorder with the metronome, we repeat the drive-parameter scan of Fig. 3 for a disordered system. Specifically, we subject a polarized initial state to realizations of the Hamiltonian of Eq. (1), where the parameters $J_{i,i+1}$ and h_i are uniform iid random variables according to $J_{i,i+1} \sim \mathcal{U}(0.5, 1.5)$ and $h_i \sim \mathcal{U}(-1, 1)$, in analogy to simulations shown in Ref. [5]. The resulting average over 250 disorder realizations of the Floquet unitary is shown in Fig. 8. Since the increase in complexity due to the disorder average required a reduction in the size of the system to $L = 13$, we also give the analogous data set for a disorder-free chain of the same length in Fig. 9. The averaged time traces approximately follow a sigmoid shape $\propto 1/(1 + \exp(\alpha t))$, as different disorder realizations have different Rabi oscillation frequencies and cancel

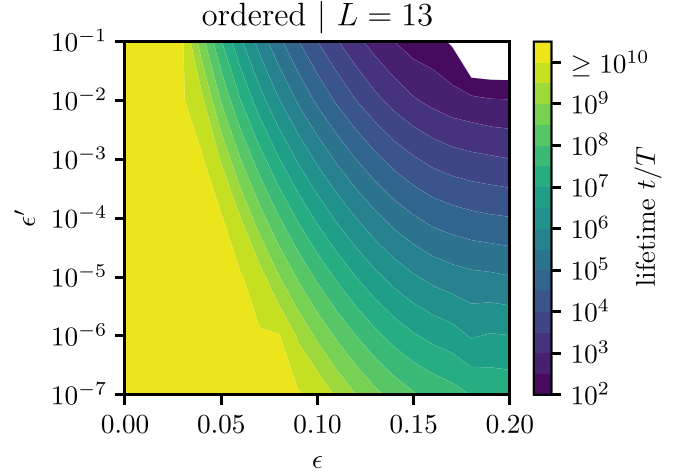


FIG. 9. The lifetimes of the global ordered-chain z magnetization with $N = 13$ spins, starting in the fully polarized initial state. The data were obtained through numerical cosine fits. Lifetimes above $\geq 10^{10}T$ and below $\leq 10^2T$ cannot be adequately resolved.

out at late times. The times plotted in Fig. 8 correspond to $t = 1/\alpha$, so the magnetization has decreased to $\sim 1/(1 + e) \approx 26.9\%$ of the plateau value. Comparing the two figures reveals that the behavior is qualitatively the same. However, making direct quantitative comparisons between the two data sets is not directly possible due to the differences discussed in the determination of the lifetime.

APPENDIX B: METRONOME SPIN AT THE CENTER OF THE CHAIN

Up until now, we have studied systems with the metronome attached to the end of a linear chain or to the side of it, coupled to the central spin of the chain. Now, we replace a central spin on the index $i = \lfloor (L+1)/2 \rfloor =: m$, i.e., $\epsilon_m = \epsilon'$. For odd chain lengths (here $L = 13$), the spin is exactly in the middle of the chain, and the system has a spatial inversion symmetry, reducing the numerical complexity. The global z magnetization of a polarized initial state is depicted in Fig. 10. The global magnetization of the centrally stabilized system has many similarities with that of the original setup with stabilization at the boundary, as shown in Fig. 2. The system demonstrates Rabi oscillations with a similar frequency and initial magnetization amplitude. However, after $\approx 10^5$ Floquet drive cycles, the metronome-spin magnetization temporarily decays to the chain average (right axis) in Fig. 10, before the subsequent Rabi oscillations set in.

The metronome is coupled to two neighboring spins subjected to the standard drive angle deviation, ϵ , instead of the previous single spin. Therefore, the observed reduced time of the initial decay compared to the boundary metronome is consistent with this difference in chain configuration. Before that decay, the dynamics of the metronome can, in good approximation, again be considered to be largely independent of the rest of the chain. Thus, the metronome effectively decouples the two half-chains, acting as a rotating field on its two neighbors. After the decay, the two chains are coupled

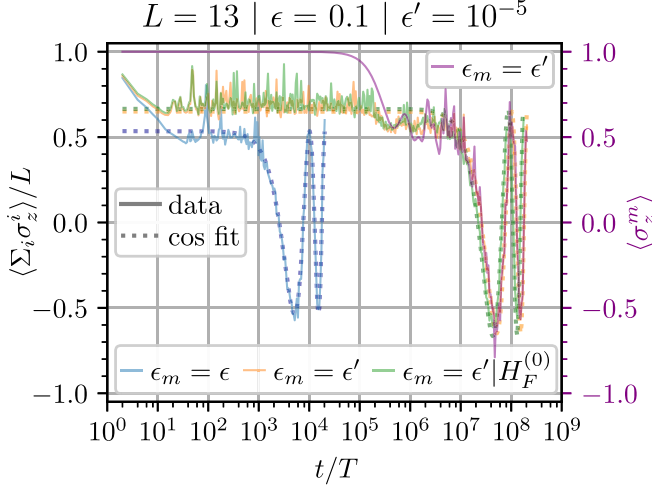


FIG. 10. The global z magnetization of the spin chain of length $L = 13$ starting in a fully polarized state subjected to different driving schemes. We show the exact stroboscopic dynamics of the chain at even period numbers with and without a metronome spin at the central site as well as the average Hamiltonian given in Eq. (5). The configurations that include a metronome spin display lifetime enhancements by several orders of magnitude. All data are well described through numerical cosine fits. On the second axis (in purple font) we display the single-spin magnetization of the metronome spin itself. The dephasing of the magnetization of the metronome coincides with the dephasing of the plateau.

again, leading to the intermediate plateau before the late-time Rabi oscillations.

APPENDIX C: NNN INTERACTIONS

Here we want to study a modified version of the original interaction Hamiltonian H_{int} given in Eq. (1). We include additional next-to-nearest-neighbor (NNN) interactions to the model,

$$H_{\text{int}}^{\text{NNN}} = H_{\text{int}} + \sum_{i=1}^{L-2} J_{i,i+2} s_z^i s_z^{i+2}, \quad (\text{C1})$$

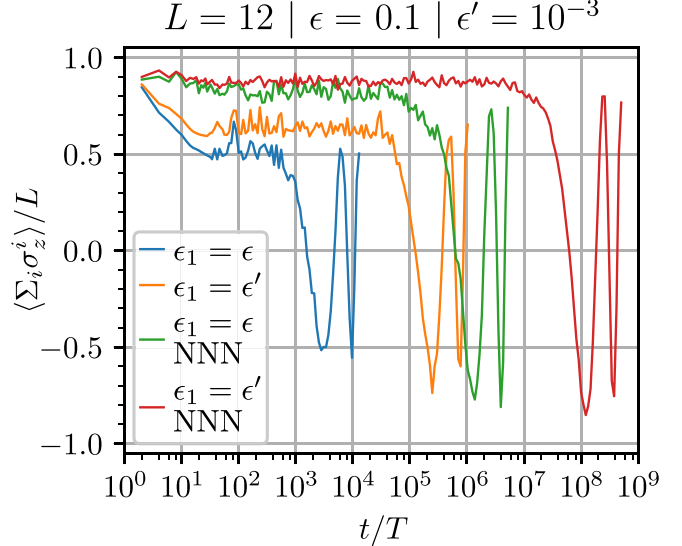


FIG. 11. The global z magnetization of the spin chain of length $L = 12$ starting in a fully polarized state subjected to different interaction Hamiltonians. We show the exact stroboscopic dynamics of the chain at even period numbers with and without a metronome spin at one boundary site, for both the standard and the integrability-breaking model (denoted NNN). Configurations that include a metronome spin display a lifetime enhancement of several orders of magnitude. For better visibility, only the first two oscillation cycles are plotted for each curve.

which break the integrability of the new effective Floquet Hamiltonian. We study the global magnetization of a polarized initial state of $L = 12$ spins subjected to the modified Floquet sequence with $H_{\text{int}}^{\text{NNN}}$ replacing the original interaction Hamiltonian H_{int} . We give the results for $J_{i,i+2} = 0.6$ and $\epsilon' = 10^{-3}$ in Fig. 11.

Both the standard model evolved through H_{int} (blue and orange curves) and the modified model evolved through $H_{\text{int}}^{\text{NNN}}$ (green and red curves) experience qualitatively comparable lifetime enhancements $\sim 1/\epsilon'$ through the addition of a metronome spin.

-
- [1] F. Wilczek, Quantum time crystals, *Phys. Rev. Lett.* **109**, 160401 (2012).
 - [2] A. Shapere and F. Wilczek, Classical time crystals, *Phys. Rev. Lett.* **109**, 160402 (2012).
 - [3] H. Watanabe and M. Oshikawa, Absence of quantum time crystals, *Phys. Rev. Lett.* **114**, 251603 (2015).
 - [4] While Ref. [3] proved the impossibility of time crystals in equilibrium states of short-range interacting systems, a recent work observed stable time-periodic oscillations in the ground state of a system at equilibrium with long-range multispin interactions [56].
 - [5] D. V. Else, B. Bauer, and C. Nayak, Floquet time crystals, *Phys. Rev. Lett.* **117**, 090402 (2016).
 - [6] D. V. Else, C. Monroe, C. Nayak, and N. Y. Yao, Discrete time crystals, *Annu. Rev. Condens. Matter Phys.* **11**, 467 (2020).
 - [7] K. Sacha, Modeling spontaneous breaking of time-translation symmetry, *Phys. Rev. A* **91**, 033617 (2015).
 - [8] V. Khemani, R. Moessner, and S. L. Sondhi, A brief history of time crystals, [arXiv:1910.10745](https://arxiv.org/abs/1910.10745).
 - [9] D. A. Abanin, W. D. Roeck, and F. Huveneers, Theory of many-body localization in periodically driven systems, *Ann. Phys. (NY)* **372**, 1 (2016).
 - [10] V. Khemani, A. Lazarides, R. Moessner, and S. L. Sondhi, Phase structure of driven quantum systems, *Phys. Rev. Lett.* **116**, 250401 (2016).
 - [11] N. Y. Yao, A. C. Potter, I.-D. Potirniche, and A. Vishwanath, Discrete time crystals: Rigidity, criticality, and realizations, *Phys. Rev. Lett.* **118**, 030401 (2017).
 - [12] H. Burau, M. Heyl, and G. De Tomasi, Fate of algebraic many-body localization under driving, *Phys. Rev. B* **104**, 224201 (2021).

- [13] D. J. Luitz, R. Moessner, S. L. Sondhi, and V. Khemani, Prethermalization without temperature, *Phys. Rev. X* **10**, 021046 (2020).
- [14] D. V. Else, B. Bauer, and C. Nayak, Prethermal phases of matter protected by time-translation symmetry, *Phys. Rev. X* **7**, 011026 (2017).
- [15] S. A. Weidinger and M. Knap, Floquet prethermalization and regimes of heating in a periodically driven, interacting quantum system, *Sci. Rep.* **7**, 45382 (2017).
- [16] D. M. Long, P. J. D. Crowley, V. Khemani, and A. Chandran, Phenomenology of the prethermal many-body localized regime, *Phys. Rev. Lett.* **131**, 106301 (2023).
- [17] M. Collura, A. De Luca, D. Rossini, and A. Lerose, Discrete time-crystalline response stabilized by domain-wall confinement, *Phys. Rev. X* **12**, 031037 (2022).
- [18] W. W. Ho, S. Choi, M. D. Lukin, and D. A. Abanin, Critical time crystals in dipolar systems, *Phys. Rev. Lett.* **119**, 010602 (2017).
- [19] A. Russomanno, F. Iemini, M. Dalmonte, and R. Fazio, Floquet time crystal in the Lipkin-Meshkov-Glick model, *Phys. Rev. B* **95**, 214307 (2017).
- [20] Z. Gong, R. Hamazaki, and M. Ueda, Discrete time-crystalline order in cavity and circuit QED systems, *Phys. Rev. Lett.* **120**, 040404 (2018).
- [21] B. Huang, Y.-H. Wu, and W. V. Liu, Clean floquet time crystals: Models and realizations in cold atoms, *Phys. Rev. Lett.* **120**, 110603 (2018).
- [22] S. Choi, J. Choi, R. Landig, G. Kucska, H. Zhou, J. Isoya, F. Jelezko, S. Onoda, H. Sumiya, V. Khemani, C. von Keyserlingk, N. Y. Yao, E. Demler, and M. D. Lukin, Observation of discrete time-crystalline order in a disordered dipolar many-body system, *Nature (London)* **543**, 221 (2017).
- [23] J. Choi, H. Zhou, S. Choi, R. Landig, W. W. Ho, J. Isoya, F. Jelezko, S. Onoda, H. Sumiya, D. A. Abanin, and M. D. Lukin, Probing quantum thermalization of a disordered dipolar spin ensemble with discrete time-crystalline order, *Phys. Rev. Lett.* **122**, 043603 (2019).
- [24] G. He, B. Ye, R. Gong, Z. Liu, K. W. Murch, N. Y. Yao, and C. Zu, Quasi-floquet prethermalization in a disordered dipolar spin ensemble in diamond, *Phys. Rev. Lett.* **131**, 130401 (2023).
- [25] J. Rovny, R. L. Blum, and S. E. Barrett, ^{31}P NMR study of discrete time-crystalline signatures in an ordered crystal of ammonium dihydrogen phosphate, *Phys. Rev. B* **97**, 184301 (2018).
- [26] J. Rovny, R. L. Blum, and S. E. Barrett, Observation of discrete-time-crystal signatures in an ordered dipolar many-body system, *Phys. Rev. Lett.* **120**, 180603 (2018).
- [27] S. Autti, V. B. Eltsov, and G. E. Volovik, Observation of a time quasicrystal and its transition to a superfluid time crystal, *Phys. Rev. Lett.* **120**, 215301 (2018).
- [28] J. Smits, L. Liao, H. T. C. Stoof, and P. van der Straten, Observation of a space-time crystal in a superfluid quantum gas, *Phys. Rev. Lett.* **121**, 185301 (2018).
- [29] S. Pal, N. Nishad, T. S. Mahesh, and G. J. Sreejith, Temporal order in periodically driven spins in star-shaped clusters, *Phys. Rev. Lett.* **120**, 180602 (2018).
- [30] J. Zhang, P. W. Hess, A. Kyriyanidis, P. Becker, A. Lee, J. Smith, G. Pagano, I.-D. Potirniche, A. C. Potter, A. Vishwanath, N. Y. Yao, and C. Monroe, Observation of a discrete time crystal, *Nature (London)* **543**, 217 (2017).
- [31] K. Wadenpfuhl and C. S. Adams, Emergence of synchronization in a driven-dissipative hot rydberg vapor, *Phys. Rev. Lett.* **131**, 143002 (2023).
- [32] X. Wu, Z. Wang, F. Yang, R. Gao, C. Liang, M. K. Tey, X. Li, T. Pohl, and L. You, Observation of a dissipative time crystal in a strongly interacting Rydberg gas, [arXiv:2305.20070](https://arxiv.org/abs/2305.20070).
- [33] X. Mi, M. Ippoliti, C. Quintana, A. Greene, Z. Chen, J. Gross, F. Arute, K. Arya, J. Atalaya, R. Babbush *et al.*, Time-crystalline eigenstate order on a quantum processor, *Nature (London)* **601**, 531 (2022).
- [34] P. Frey and S. Rachel, Realization of a discrete time crystal on 57 qubits of a quantum computer, *Sci. Adv.* **8**, eabm7652 (2022).
- [35] J. Šuntajs, J. Bonca, T. Prosen, and L. Vidmar, Quantum chaos challenges many-body localization, *Phys. Rev. E* **102**, 062144 (2020).
- [36] D. Sels and A. Polkovnikov, Dynamical obstruction to localization in a disordered spin chain, *Phys. Rev. E* **104**, 054105 (2021).
- [37] P. Sierant and J. Zakrzewski, Challenges to observation of many-body localization, *Phys. Rev. B* **105**, 224203 (2022).
- [38] A. Morningstar, L. Colmenarez, V. Khemani, D. J. Luitz, and D. A. Huse, Avalanches and many-body resonances in many-body localized systems, *Phys. Rev. B* **105**, 174205 (2022).
- [39] C. W. von Keyserlingk, V. Khemani, and S. L. Sondhi, Absolute stability and spatiotemporal long-range order in Floquet systems, *Phys. Rev. B* **94**, 085112 (2016).
- [40] F. Machado, Q. Zhuang, N. Y. Yao, and M. P. Zaletel, Absolutely stable time crystals at finite temperature, *Phys. Rev. Lett.* **131**, 180402 (2023).
- [41] K. Giergiel, J. Wang, B. J. Dalton, P. Hannaford, and K. Sacha, Discrete time crystals with absolute stability, *Phys. Rev. B* **108**, L180201 (2023).
- [42] S. T. Schindler and H. H. Sheinfux, Floquet engineering with spatially non-uniform driving fields, [arXiv:2311.00845](https://arxiv.org/abs/2311.00845).
- [43] T. Mori, T. Kuwahara, and K. Saito, Rigorous bound on energy absorption and generic relaxation in periodically driven quantum systems, *Phys. Rev. Lett.* **116**, 120401 (2016).
- [44] D. A. Abanin, W. De Roeck, W. W. Ho, and F. Huveneers, Effective Hamiltonians, prethermalization, and slow energy absorption in periodically driven many-body systems, *Phys. Rev. B* **95**, 014112 (2017).
- [45] W. C. Yu, J. Tangpanitanon, A. W. Glaetzle, D. Jaksch, and D. G. Angelakis, Discrete time crystal in globally driven interacting quantum systems without disorder, *Phys. Rev. A* **99**, 033618 (2019).
- [46] W. Magnus, On the exponential solution of differential equations for a linear operator, *Commun. Pure Appl. Math.* **7**, 649 (1954).
- [47] S. Blanes, F. Casas, J. A. Oteo, and J. Ros, The Magnus expansion and some of its applications, *Phys. Rep.* **470**, 151 (2009).
- [48] D. J. Yates, F. H. L. Essler, and A. Mitra, Almost strong $(0, \pi)$ edge modes in clean interacting one-dimensional Floquet systems, *Phys. Rev. B* **99**, 205419 (2019).
- [49] A. Y. Kitaev, Unpaired Majorana fermions in quantum wires, *Phys.-Usp.* **44**, 131 (2001).

- [50] T. Senthil, Symmetry-protected topological phases of quantum matter, *Annu. Rev. Condens. Matter Phys.* **6**, 299 (2015).
- [51] J. Kemp, N. Y. Yao, C. R. Laumann, and P. Fendley, Long coherence times for edge spins, *J. Stat. Mech.* (2017) 063105.
- [52] D. J. Yates, A. G. Abanov, and A. Mitra, Long-lived period-doubled edge modes of interacting and disorder-free Floquet spin chains, *Commun. Phys.* **5**, 43 (2022).
- [53] D. V. Else, P. Fendley, J. Kemp, and C. Nayak, Prethermal strong zero modes and topological qubits, *Phys. Rev. X* **7**, 041062 (2017).
- [54] F. Machado, D. V. Else, G. D. Kahanamoku-Meyer, C. Nayak, and N. Y. Yao, Long-range prethermal phases of nonequilibrium matter, *Phys. Rev. X* **10**, 011043 (2020).
- [55] J. Bezanson, A. Edelman, S. Karpinski, and V. B. Shah, Julia: A fresh approach to numerical computing, *SIAM Rev.* **59**, 65 (2017).
- [56] V. K. Kozin and O. Kyriienko, Quantum time crystals from Hamiltonians with long-range interactions, *Phys. Rev. Lett.* **123**, 210602 (2019).

OUTLOOK: OBSERVATION OF A TIME CRYSTAL IN THE RYDBERG EXPERIMENT?

Novel stabilization mechanisms due to disorder?

`rydberg-pair-timecrystal.jl` Replace interacting Hamiltonian with Pair model. Then dynamics are effectively average over pair distribution. Each pair is not stable but has some lifetime depending on its interaction strength. Since distribution is very broad there is some phase-wrapping going on which leads to a slow decay. So pair model predicts not a stable time crystal but an anomalously slow decay (stretched exponential again?).

12

DISCUSSION

Part III
SUMMARY

13

SUMMARY

Two routes to non-thermalization (or to avoid thermalization at the usual short timescales) that both generate effectively conserved quantities in a subtle way.

BIBLIOGRAPHY

- [1] D. J. Luitz, F. Huveneers, and W. De Roeck, "How a Small Quantum Bath Can Thermalize Long Localized Chains," *Physical Review Letters* **119**, 150602 (2017).
- [2] R. Nandkishore and S. Gopalakrishnan, "Many body localized systems weakly coupled to baths: Many body localized systems weakly coupled to baths," *Annalen der Physik* **529**, 1600181 (2017).
- [3] P. Reimann, "Foundation of Statistical Mechanics under Experimentally Realistic Conditions," *Physical Review Letters* **101**, 190403 (2008).
- [4] N. Linden, S. Popescu, A. J. Short, and A. Winter, "Quantum mechanical evolution towards thermal equilibrium," *Physical Review E* **79**, 061103 (2009).
- [5] J. M. Deutsch, "Quantum statistical mechanics in a closed system," *Physical Review A* **43**, 2046–2049 (1991).
- [6] M. Srednicki, "Chaos and Quantum Thermalization," *Physical Review E* **50**, 888–901 (1994).
- [7] M. Rigol, V. Dunjko, and M. Olshanii, "Thermalization and its mechanism for generic isolated quantum systems," *Nature* **452**, 854–858 (2008).
- [8] C. Gogolin and J. Eisert, "Equilibration, thermalisation, and the emergence of statistical mechanics in closed quantum systems," *Reports on Progress in Physics* **79**, 056001 (2016).
- [9] L. D'Alessio, Y. Kafri, A. Polkovnikov, and M. Rigol, "From quantum chaos and eigenstate thermalization to statistical mechanics and thermodynamics," *Advances in Physics* **65**, 239–362 (2016).
- [10] J. M. Deutsch, "Eigenstate Thermalization Hypothesis," *Reports on Progress in Physics* **81**, 082001 (2018).
- [11] T. Mori, T. N. Ikeda, E. Kaminishi, and M. Ueda, "Thermalization and prethermalization in isolated quantum systems: a theoretical overview," *Journal of Physics B: Atomic, Molecular and Optical Physics* **51**, 112001 (2018).
- [12] S. Sugimoto, R. Hamazaki, and M. Ueda, "Eigenstate Thermalization in Long-Range Interacting Systems," *Physical Review Letters* **129**, 030602 (2022).
- [13] P. W. Anderson, "Absence of Diffusion in Certain Random Lattices," *Physical Review* **109**, 1492–1505 (1958).

- [14] J. Z. Imbrie, V. Ros, and A. Scardicchio, "Review: Local Integrals of Motion in Many-Body Localized systems," *Annalen der Physik* **529**, 1600278 (2017).
- [15] M. Kiefer-Emmanouilidis, R. Unanyan, M. Fleischhauer, and J. Sirker, "Evidence for Unbounded Growth of the Number Entropy in Many-Body Localized Phases," *Physical Review Letters* **124**, 243601 (2020).
- [16] D. A. Chávez, C. Artiaco, T. K. Kvorning, L. Herviou, and J. H. Bardarson, *Ultraslow Growth of Number Entropy in an l-bit Model of Many-Body Localization*, Dec. 2023.
- [17] J. H. Bardarson, F. Pollmann, and J. E. Moore, "Unbounded Growth of Entanglement in Models of Many-Body Localization," *Physical Review Letters* **109**, 017202 (2012).
- [18] Y. Huang, *Extensive Entropy from Unitary Evolution*, Preprint (PHYSICAL SCIENCES, Apr. 2021).
- [19] K. Huang, D. Vu, S. Das Sarma, and X. Li, "Interaction-enhanced many-body localization in a generalized Aubry-André model," *Physical Review Research* **6**, L022054 (2024).
- [20] J. Z. Imbrie, "On Many-Body Localization for Quantum Spin Chains," *Journal of Statistical Physics* **163**, 998–1048 (2016).
- [21] N. Y. Yao, C. R. Laumann, S. Gopalakrishnan, M. Knap, M. Müller, E. A. Demler, and M. D. Lukin, "Many-Body Localization in Dipolar Systems," *Physical Review Letters* **113**, 243002 (2014).
- [22] A. L. Burin, "Many-body delocalization in a strongly disordered system with long-range interactions: Finite-size scaling," *Physical Review B* **91**, 094202 (2015).
- [23] D. B. Gutman, I. V. Protopopov, A. L. Burin, I. V. Gornyi, R. A. Santos, and A. D. Mirlin, "Energy transport in the Anderson insulator," *Physical Review B* **93**, 245427 (2016).
- [24] A. L. Burin, *Energy delocalization in strongly disordered systems induced by the long-range many-body interaction*, Nov. 2006.
- [25] A. L. Burin, "Localization in a random XY model with long-range interactions: Intermediate case between single-particle and many-body problems," *Physical Review B* **92**, 104428 (2015).
- [26] A. Safavi-Naini, M. L. Wall, O. L. Acevedo, A. M. Rey, and R. M. Nandkishore, "Quantum dynamics of disordered spin chains with power-law interactions," *Physical Review A* **99**, 033610 (2019).
- [27] S. Schiffer, J. Wang, X.-J. Liu, and H. Hu, "Many-body localization in X Y spin chains with long-range interactions: An exact-diagonalization study," *Physical Review A* **100**, 063619 (2019).

- [28] R. Yousefjani and A. Bayat, "Mobility edge in long-range interacting many-body localized systems," *Physical Review B* **107**, 045108 (2023).
- [29] Y. Mohdeb, J. Vahedi, N. Moure, A. Roshani, H.-Y. Lee, R. N. Bhatt, S. Kettemann, and S. Haas, "Entanglement properties of disordered quantum spin chains with long-range antiferromagnetic interactions," *Physical Review B* **102**, 214201 (2020).
- [30] Y. Mohdeb, J. Vahedi, and S. Kettemann, "Excited-Eigenstate Entanglement Properties of XX Spin Chains with Random Long-Range Interactions," *Physical Review B* **106**, 104201 (2022).
- [31] Y. Mohdeb, J. Vahedi, R. N. Bhatt, S. Haas, and S. Kettemann, "Global quench dynamics and the growth of entanglement entropy in disordered spin chains with tunable range interactions," *Physical Review B* **108**, L140203 (2023).
- [32] J. Brey and A. Prados, "Stretched exponential decay at intermediate times in the one-dimensional Ising model at low temperatures," *Physica A: Statistical Mechanics and its Applications* **197**, 569–582 (1993).
- [33] A. Signoles, T. Franz, R. F. Alves, M. Gärtnner, S. Whitlock, G. Zürn, and M. Weidemüller, "Glassy dynamics in a disordered Heisenberg quantum spin system," *Physical Review X* **11**, 011011 (2021).
- [34] P. Schultzen, T. Franz, S. Geier, A. Salzinger, A. Tebben, C. Hainaut, G. Zürn, M. Weidemüller, and M. Gärtnner, "Glassy quantum dynamics of disordered Ising spins," *Physical Review B* **105**, L020201 (2022).
- [35] P. Schultzen, T. Franz, C. Hainaut, S. Geier, A. Salzinger, A. Tebben, G. Zürn, M. Gärtnner, and M. Weidemüller, "Semiclassical simulations predict glassy dynamics for disordered Heisenberg models," *Physical Review B* **105**, L100201 (2022).
- [36] A. Haldar, *Slow Dynamics and Kohlrausch Relaxation in Isolated Disordered Many-Body Systems*, Feb. 2023.
- [37] S. Chandrasekhar, "Stochastic Problems in Physics and Astronomy," *Reviews of Modern Physics* **15**, 1–89 (1943).
- [38] P. Kaposvári, *Describing the dynamics of disordered heisenberg xxz model with real space renormalisation group methods*, Master's thesis, Heidelberg, Germany, Feb. 2021.

ACKNOWLEDGMENTS

Martin, Matthias, reviewer Tilman Enss, committee Jörg Evers, Selim
Office mate Niklas (seitan), rest of old PhD crew Adrian (Nordic light
expedition), Moritz and Javad. new crew Martina, Elena, Mauro. Supervision of Maximilian Müllenbach, Mohammed Sinan, Mirco Erpelding
(who always gave 112%), Florian.

enjoyed close collaboration with experimentalist, first and foremost
Titus, Sebastian, Eduard. Gerhard. All the others, with whom I had
some contact: Clement, Moritz, Valentina, Andre

Family.

Brini.